

**Fundamental Studies of the Herschel-Quincke Tube Concept  
with Mode Measurements**

By

**Michael M. James**

Thesis submitted to the Faculty of the  
Virginia Polytechnic Institute and State University  
in partial fulfillment of the requirements for the degree of

Masters of Science  
in  
Mechanical Engineering

Ricardo Burdisso, Chair  
Marty Johnson  
Don Leo

December 15, 2005  
Blacksburg, Virginia

**Keywords:** Duct Acoustics, Noise Control, Herschel-Quincke Tube,  
Higher-Order Modes

Copyright 2005, Michael M. James

# **Fundamental Studies of the Herschel-Quincke Tube Concept with Mode Measurements**

By

**Michael M. James**

Committee chairman: Ricardo A. Burdisso

(Abstract)

A fundamental study of the Herschel-Quincke (HQ) tube concept for the reduction of noise in circular ducts is presented here. Recent testing of the Herschel-Quincke tube concept on the Pratt-Whitney JT15D and AlliedSignal TFE731-60 engines showed the potential for the practical application of this approach. A model of the HQ-system has been developed to aid in the design of the system tested. The model has revealed new noise control mechanisms associated to the implementation of multiple HQ-waveguides in a duct in the presence of higher order modes. However, the practical nature of these engine facilities results in limitations with regard to the fundamental research knowledge that could be gained from testing in a more controlled laboratory environment.

A series of experiments was conducted at the NASA Langley Research Center 0.30 m ducted fan test facility where detailed modal measurements were performed. The main goals of this research endeavor were to evaluate the accuracy of the previously developed theoretical model and provide insight into the noise control mechanisms. Experiments were performed with different disturbance mode structures, number of HQ tubes and arrays, and axial positions. The modes in the duct were generated with an array of acoustic drivers (no flow case) and measured with logarithmically spaced circumferential and helical microphone arrays located on the duct wall. The modal amplitudes of the incident, transmitted, and reflected modes in the duct were determined from the microphone measurements. This allowed for the comparison of analytical and experimental modal amplitudes, modal powers, total power, and reductions.

The results of this study provide insight into the three noise control mechanisms associated with this approach: reflection, circumferential scattering, and radial scattering. Comparison with the experimental results shows that the model accurately predicts the sound power attenuation except near the cut-off frequency of the modes where it tends to overestimate the attenuation. The effect of the number of tubes in the array and its axial position was also evaluated. Overall, the results of this study validate the general modeling approach for the HQ tube concept.

## **Acknowledgements**

I would like to thank Dr. Ricardo Burdisso for giving me the opportunity to work on a challenging and interesting research project and for his support and guidance. I would also like to thank Dr. Marty Johnson and Dr. Don Leo for serving on my advisory committee. In addition, I would like to thank the staff of the NASA Langley Research Center Aeroacoustics Branch, in particular Dr. Carl Gerhold and Dr. Joe Posey, for their support.

I would like to express my gratitude and respect to Jason Anderson who has been an incredible friend throughout the years and has pushed me intellectually. A special thank you is extended to Simon Esteve for his friendship and love of great music. I also wish to thank my friends in the Vibration and Acoustics Laboratories, especially John D'Angelo, Tony Harris, Jose Alonzo, and Raphael Hallez, for their support and friendship in and out of work.

Finally, I would like to thank my parents for their support, confidence, and love, and my brothers, for being my best friends even though I have been gone for years.

# Table of Contents

<b>Title Page</b> .....	<b>i</b>
<b>Abstract</b> .....	<b>ii</b>
<b>Acknowledgements</b> .....	<b>iii</b>
<b>Table of Contents</b> .....	<b>iv</b>
<b>List of Figures</b> .....	<b>vii</b>
<b>List of Tables</b> .....	<b>xiv</b>
<b>Chapter 1. Introduction</b> .....	<b>1</b>
1.1 Turbofan Engine Noise.....	2
1.2 The Herschel-Quincke Tube Concept.....	4
1.3 Motivation.....	6
1.4 Objectives and Approach.....	7
1.5 Organization.....	8
<b>Chapter 2. Review of HQ Tube Modeling Approach</b> .....	<b>9</b>
2.1 Modes In Circular Ducts.....	9
2.2 HQ Tube Modeling Technique.....	13
2.2.1 Duct Dynamics.....	14
2.2.2 HQ Tube Dynamics .....	15

2.2.3	Coupled HQ Tube–Duct System .....	17
2.3	Modal Amplitudes and Sound Power .....	18
2.3.1	Modal Amplitudes .....	19
2.3.2	Modal Sound Power.....	21
<b>Chapter 3.</b>	<b>Experimental Effort.....</b>	<b>23</b>
3.1	Experimental Setup.....	23
3.1.1	Noise Sources.....	24
3.1.2	HQ Tube Systems .....	26
3.1.3	Microphone Arrays .....	29
3.1.4	Silencer .....	31
3.1.5	Test Configurations.....	31
3.2	HQ Tube System Modal Analysis .....	37
3.2.1	Duct Cut-Off Frequencies.....	37
3.2.2	HQ Tube Scattering Analysis .....	38
3.2.3	Incident and Transmitted Cut-On Modes .....	39
3.3	Data Analysis and Post Processing.....	39
3.3.1	Data Collection and Reduction .....	40
3.3.2	Modal Decomposition Technique.....	40
3.3.3	Orthogonality Assumption.....	46
<b>Chapter 4.</b>	<b>Experimental Results.....</b>	<b>50</b>
4.1	Microphone Signal Analysis.....	50
4.1.1	Auto Spectrums.....	51
4.1.2	Coherence and Cut-off Frequency .....	52
4.1.3	Cross Spectrum .....	54
4.2	Modal Decomposition Results.....	56
4.3	Analytical Incident Modal Amplitude Predictions .....	60
4.4	Theoretical vs. Experimental Modal Power Comparisons .....	64
4.4.1	Test 1: Single Incident Mode.....	66
4.4.2	Test 2: Number of HQ Tubes.....	70

4.4.3	Test 3: Multiple Incident Modes.....	73
4.4.4	Test 4: Multiple Incident Modes, Effects of Axial Position, Radial Scattering, and Multiple Arrays.....	81
4.4.5	Test 5: Circumferential Scattering.....	97
<b>Chapter 5. Conclusions and Recommendations.....</b>		<b>102</b>
5.1	Theoretical and Experimental Conclusions.....	102
5.2	Recommendations.....	103
<b>Appendix A. Additional Work.....</b>		<b>106</b>
A.1	Repeatability Analysis.....	106
<b>References.....</b>		<b>112</b>

# List of Figures

Figure 1-1: The Herschel-Quincke tube concept.....	4
Figure 2-1: Cross sectional pressure distributions of the $(m,n)$ modes.....	10
Figure 2-2: Infinite rigid wall duct with spinning and propagating acoustic modes.....	11
Figure 2-3: Model of infinite rigid wall circular duct with HQ tube system.....	13
Figure 2-4: Model of duct with finite piston sources.....	14
Figure 2-5: Model of HQ tubes.....	15
Figure 2-6: HQ tube array model.....	16
Figure 3-1: NASA Langley Research Center testing facility.....	24
Figure 3-2: Array of 12 equally spaced acoustic drivers.....	25
Figure 3-3: HQ tube system.....	27
Figure 3-4: HQ tube design.....	28
Figure 3-5: HQ tube system with and without the perforated screen.....	29
Figure 3-6: Logarithmically spaced circumferential and helical microphone arrays located on the duct wall.....	29
Figure 3-7: Silencer used to minimize reflections in the duct.....	31
Figure 3-8: NASA Langley Research Center testing facility. Incident and transmitted mode measurement test rig.....	32
Figure 3-9: NASA Langley Research Center testing facility and reflected mode measurement test rig.....	33
Figure 3-10: HQ tube system configurations to measure transmitted and reflected modes.....	35

Figure 3-11: Comparison of the product of the positive spinning and traveling (1,0) mode versus each positive spinning and traveling mode in the duct.....	47
Figure 3-12: Comparison of the product of the positive spinning and traveling (1,0) mode versus each negative spinning and positive traveling mode in the duct.....	48
Figure 3-13: Comparison of the product of the positive spinning and traveling (1,0) mode versus each positive spinning and negative traveling mode in the duct.....	48
Figure 3-14: Comparison of the product of the positive spinning and traveling (1,0) mode versus each negative spinning and traveling mode in the duct.....	49
Figure 4-1: Auto Spectrum of microphone 5 for the hard wall cases with the (2,0) incident mode.....	51
Figure 4-2: Auto Spectrums of microphone 5 comparing the hard wall case with the (2,0) incident mode and the background noise.....	52
Figure 4-3: Coherence between microphones 1 and 2 for hard wall case with the (2,0) incident mode.....	53
Figure 4-4: Relative phase of microphones 1 through 7 with respect to microphone 1 ..	55
Figure 4-5: Comparison of the relative phase of microphones 1 through 7 with respect to microphone 1 and their respective angular positions. ....	55
Figure 4-6: Sound power versus frequency for the (0,0) mode. ....	57
Figure 4-7: Sound power versus frequency of the (0,1) mode. ....	57
Figure 4-8: Sound power versus frequency of the (1,0) mode. ....	58
Figure 4-9: Sound power versus frequency of the (1,1) mode. ....	58
Figure 4-10: Sound power versus frequency of (2,0) mode. ....	59
Figure 4-11: Sound power versus frequency of the (3,0) mode. ....	59
Figure 4-12: Sound power versus frequency of the (4,0) mode. ....	60
Figure 4-13: The relative modal amplitude phase of the (1,0) and (1,1) modes.....	61
Figure 4-14: Total sound power reduction of the $m$ -order 1 modes, in-phase.....	63
Figure 4-15: Total sound power reduction of the $m$ -order 1 modes, out-of-phase.....	63
Figure 4-16: Test 1 experimental setup with HQ tube system.....	66
Figure 4-17: Experimental $W_l^{++}$ of the (2,0) mode.....	67

Figure 4-18: Analytical versus experimental $W_T^{++}$ of the (2,0) mode with 16 HQ tubes in position 4. ....	68
Figure 4-19: Analytical versus experimental $W_{Red}^{++}$ of the (2,0) mode with 16 HQ tubes in position 4. ....	68
Figure 4-20: The (2,0) mode: analytical versus experimental $W_R^{+-}$ with 16 HQ tubes in position 6 compared to the experimental hard wall $W_R^{+-}$ . ....	69
Figure 4-21: Test 2 experimental setup with 8 HQ tubes. ....	70
Figure 4-22: Test 2 experimental setup with 16 HQ tubes. ....	71
Figure 4-23: Analytical versus experimental $W_{Red}^{++}$ of the (2,0) mode with 8 HQ tubes in position 4. ....	72
Figure 4-24: Analytical versus experimental $W_{Red}^{++}$ of the (2,0) mode with 16 HQ tubes in position 4. ....	72
Figure 4-25: Test 3 experimental setup with HQ tube system. ....	73
Figure 4-26: Experimental total $W_I^{++}$ of the $m$ -order 0 modes. ....	75
Figure 4-27: Experimental $W_I^{++}$ of the (0,0) mode. ....	75
Figure 4-28: Experimental $W_I^{++}$ of the (0,1) mode. ....	76
Figure 4-29: Analytical versus experimental total $W_T^{++}$ of the $m$ -order 0 modes with 16 HQ tubes in position 1. ....	76
Figure 4-30: Analytical versus experimental $W_T^{++}$ of the (0,0) mode with 16 HQ tubes in position 1. ....	77
Figure 4-31: Analytical versus experimental $W_T^{++}$ of the (0,1) mode with 16 HQ tubes in position 1. ....	77
Figure 4-32: Analytical versus experimental total $W_{Red}^{++}$ of the $m$ -order 0 modes with 16 HQ tubes in position 1. ....	78
Figure 4-33: Analytical versus experimental $W_{Red}^{++}$ of the (0,0) mode with 16 HQ tubes in position 1. ....	78

Figure 4-34: Analytical versus experimental  $W_{Red}^{++}$  of the (0,1) mode with 16 HQ tubes in position 1. .... 79

Figure 4-35: The  $m$ -order 0 modes: analytical versus experimental total  $W_R^{+-}$  with 16 HQ tubes in position 6 compared to the experimental hard wall  $W_R^{+-}$  and  $W_I^{++}$ . 79

Figure 4-36: The (0,0) mode: analytical versus experimental  $W_R^{+-}$  with 16 HQ tubes in position 6 compared to the experimental hard wall  $W_R^{+-}$  and  $W_I^{++}$  ..... 80

Figure 4-37: The (0,1) mode: analytical versus experimental  $W_R^{+-}$  with 16 HQ tubes in position 6 compared to the experimental hard wall  $W_R^{+-}$  and  $W_I^{++}$  ..... 80

Figure 4-38: Test 3 experimental setup with HQ tube system ..... 82

Figure 4-39: Experimental total  $W_I^{++}$  of the  $m$ -order 1 modes. .... 84

Figure 4-40: Experimental  $W_I^{++}$  of the (1,0) mode..... 84

Figure 4-41: Experimental  $W_I^{++}$  of the (1,1) mode..... 85

Figure 4-42: Analytical versus experimental total  $W_T^{++}$  of the  $m$ -order 1 modes with 16 HQ tubes in position 1. .... 85

Figure 4-43: Analytical versus experimental  $W_T^{++}$  of the (1,1) mode with 16 HQ tubes in position 1. .... 86

Figure 4-44: Analytical versus experimental  $W_T^{++}$  of the (1,1) mode with 16 HQ tubes in position 1. .... 86

Figure 4-45: Analytical versus experimental total  $W_{Red}^{++}$  of the  $m$ -order 1 modes with 16 HQ tubes in position 1. .... 87

Figure 4-46: Analytical versus experimental  $W_{Red}^{++}$  of the (1,0) mode with 16 HQ tubes in position 1. .... 87

Figure 4-47: Analytical versus experimental  $W_{Red}^{++}$  of the (1,1) mode with 16 HQ tubes in position 1. .... 88

Figure 4-48: Analytical versus experimental total  $W_{Red}^{++}$  of the  $m$ -order 1 modes with 16 HQ tubes in position 2. .... 88

Figure 4-49: Analytical versus experimental  $W_{Red}^{++}$  of the (1,0) mode with 16 HQ tubes in position 2. .... 89

Figure 4-50: Analytical versus experimental  $W_{Red}^{++}$  of the (1,1) mode with 16 HQ tubes in position 2. .... 89

Figure 4-51: Analytical versus experimental total  $W_{Red}^{++}$  of the  $m$ -order 1 modes with 16 HQ tubes in position 3. .... 90

Figure 4-52: Analytical versus experimental  $W_{Red}^{++}$  of the (1,0) mode with 16 HQ tubes in position 3. .... 90

Figure 4-53: Analytical versus experimental  $W_{Red}^{++}$  of the (1,1) mode with 16 HQ tubes in position 3. .... 91

Figure 4-54: Analytical versus experimental total  $W_{Red}^{++}$  of the  $m$ -order 1 modes with 16 HQ tubes in position 4. .... 91

Figure 4-55: Analytical versus experimental  $W_{Red}^{++}$  of the (1,0) mode with 16 HQ tubes in position 4. .... 92

Figure 4-56: Analytical versus experimental  $W_{Red}^{++}$  of the (1,1) mode with 16 HQ tubes in position 4. .... 92

Figure 4-57: Frequency of maximum sound power reduction of the total power of the  $m$ -order 1 modes as a function of axial position of the HQ tubes..... 93

Figure 4-58: Maximum sound power reduction of the total power of the  $m$ -order 1 modes as a function of axial position of the HQ tubes. .... 93

Figure 4-59: The  $m$ -order 1 modes: analytical versus experimental total  $W_R^{+-}$  with 16 HQ tubes in position 6 compared to the experimental hard wall  $W_R^{+-}$  and  $W_I^{++}$ . 94

Figure 4-60: The (1,0) mode: analytical versus experimental  $W_R^{+-}$  with 16 HQ tubes in position 6 compared to the experimental hard wall  $W_R^{+-}$  and  $W_I^{++}$  ..... 94

Figure 4-61: The (1,1) mode: analytical versus experimental  $W_R^{+-}$  with 16 HQ tubes in position 6 compared to the experimental hard wall  $W_R^{+-}$  and  $W_I^{++}$  ..... 95

Figure 4-62: Analytical versus experimental total $W_{Red}^{++}$ of the $m$ -order 1 modes with 16 HQ tubes in position 5. ....	95
Figure 4-63: Analytical versus experimental $W_{Red}^{++}$ of the (1,0) mode with 16 HQ tubes in position 5. ....	96
Figure 4-64: Analytical versus experimental $W_{Red}^{++}$ of the (1,1) mode with 16 HQ tubes in position 5. ....	96
Figure 4-65: Test 5 experimental setup with HQ tube system.....	97
Figure 4-66 Experimental $W_I^{++}$ of the (4,0) mode compared to the experimental $W_I^{-+}$ . .	98
Figure 4-67: Analytical versus experimental total $W_T$ of the $m$ -order 4 modes with 8 HQ tubes in position 1.....	99
Figure 4-68: Analytical versus experimental $W_T^{++}$ of the (4,0) mode with 8 HQ tubes in position 1. ....	99
Figure 4-69: Analytical versus experimental $W_T^{-+}$ of the (-4,0) mode with 8 HQ tubes in position 1. ....	100
Figure 4-70: Analytical versus experimental total $W_{Red}$ of the $m$ -order 4 modes with 8 HQ tubes in position 1.....	100
Figure 4-71: Analytical versus experimental $W_{Red}^{++}$ of the (4,0) mode with 8 HQ tubes in position 1. ....	101
Figure 5-1: Comparison between the magnitude and phase of the frequency response function of round and square tubes.....	105
Figure A-1: Experimental comparisons of the total $W_{Red}^{++}$ of the $m$ -order 0 modes.....	107
Figure A-2: Experimental comparisons of the total $W_{Red}^{++}$ of the (0,0) mode.....	107
Figure A-3: Experimental comparisons of the total $W_{Red}^{++}$ of the (0,1) mode.....	108
Figure A-4: Experimental comparisons of the total $W_{Red}^{++}$ of the $m$ -order 1 modes.....	108
Figure A-5: Experimental comparisons of the total $W_{Red}^{++}$ of the (1,0) mode.....	109

Figure A-6: Experimental comparisons of the total $W_{Red}^{++}$ of the (1,1) mode.....	109
Figure A-7: Experimental comparisons of the total $W_{Red}^{++}$ of the (2,0) mode.....	110
Figure A-8: Experimental comparisons of the total $W_{Red}^{++}$ of the (3,0) mode.....	110
Figure A-9: Experimental comparisons of the total $W_{Red}^{++}$ of the (4,0). .....	111

## List of Tables

Table 3-1: The required phase in radians for each acoustic driver $r$ , to generate a specific disturbance mode $m$ . .....	26
Table 3-2: HQ tube design parameters. ....	28
Table 3-3: Axial and angular microphone positions. ....	30
Table 3-4: Possible HQ tube configurations. ....	36
Table 3-5: Duct cut-off frequencies in Hz. ....	37
Table 3-6: Circumferential modes scattered due to HQ tubes. ....	38
Table 3-7: Incident and transmitted cut-on modes at $f=2500$ Hz. ....	39
Table 4-1: Analytical versus experimental cut-off frequency comparison. ....	54

# Chapter 1. Introduction

Noise pollution is a pervasive problem for those who live, work, and travel in a modern society. Some of the sounds we are bombarded with every day are easily controlled. However, other noises are more difficult to control. The buildings and vehicles we spend much of our time in generate distracting noise that is often inescapable.

Noise radiating from walls and duct openings can be loud and annoying. Reducing this type of noise presents an important challenge. The answer often lies in the re-design of the noise source itself. However, an existing system that cannot be re-designed, or a system that requires additional noise attenuation, calls for an alternative solution. Both passive and active techniques have been used to provide additional noise control. Passive approaches use absorption or reflection of the original noise source to provide noise control. Techniques using absorption such as acoustic liners have traditionally been used but, while providing good attenuation at high frequencies, attenuation is poor at low frequencies. The liners also provide poor attenuation of large amplitude components at discrete frequencies. Reactive devices use a change in geometry to reflect some of the energy of the original sound field back to the noise source. These devices such as Helmholtz resonators, expansion chambers, and Herschel Quincke tubes are primarily used in suppression of plane waves. In contrast, active noise control (ANC) techniques use a secondary noise source to cancel out the original noise source. These techniques usually consist of sensors, an active noise control system, and secondary noise sources. In general, these systems provide good noise reduction, however they are often extremely complex, expensive, and sometimes fragile.

## Chapter 1. Introduction

Turbofan engine noise has become an increasingly significant source for noise pollution in recent years. The limitations of conventional passive and active noise control techniques have inspired an innovative use of an old concept to solve this modern problem. The Herschel-Quincke (HQ) tube technique discussed in this study is a simple, inexpensive passive device that, employed properly, can provide both tonal and broadband noise reduction. A fundamental study of the HQ tubes noise control mechanisms and evaluation of the accuracy of the previously developed theoretical model is examined in this study.

Chapter 1 will briefly discuss turbofan engine noise and several noise reduction techniques. Next, the Herschel-Quincke tube concept will be presented along with relevant previous work. Finally, the motivation, objectives, approach, and organization of this work will be presented.

### **1.1 Turbofan Engine Noise**

Duct noise from turbofan engines has become a significant problem in recent years due to the increasing numbers of flights contributing to extreme levels of noise pollution over populated areas. This has spawned new government regulations lowering the acceptable levels of noise produced from turbofan engines. These regulations include stringent noise requirements on new engines as well as mandating retrofitting on older engines. In addition, these requirements must be met while causing minimal impact on airplane performance. Aircraft noise has become such a serious problem in some locations, such as Reagan International Airport, that the government has had to limit the number of flights to stay within noise ordinances.

Efforts to reduce aircraft noise have been concentrated on three areas: engine, nacelle (the cowling that houses the engine), and airframe. The primary focus of noise reduction on turbofan engines has been the tonal noise produced by the fan. The fan blades cause noise by pushing through the air. The wakes of air produced from the fan flow slap against the stators. This slapping generates tones that are called the blade

## Chapter 1. Introduction

passage frequency (BPF) and harmonics. These tones cause a piercing sound and are often 10-15 dB above the broadband level. The broadband noise, heard as a rumbling sound, is a result of the interaction of the unsteadiness in the fan flow with the stators [1]. The increasing bypass ratios of today's engines mean the level of the BPF is increasing while its frequencies are decreasing.

The first step in reducing noise in these complex pressure field systems has been the redesign of the disturbance itself. Improvements in fan geometry, leaned blades, rotor-stator spacing, blade-wake tailoring, boundary-layer effects, and fan speed have resulted in significant attenuation. However, there is still need for additional noise reduction.

The traditional method of noise reduction in turbofan engines has been the use of acoustic liners, which are passive devices that dissipate acoustic energy into heat [2]. The liners are made of a porous skin supported by a honeycomb like core. The frequencies and level of attenuation produced from liners are proportional to their thickness and length of treatment. However, along with lower frequencies and larger levels, high bypass ratio engines also have shorter inlets. Liners are not well suited to meet these demands. Their relatively small thickness provides poor attenuation characteristics at low frequencies. They are also not particularly appropriate for attenuation of large amplitude components of discrete frequency. Shorter inlets, which decrease the length of liner treatment, will further reduce their efficiency. Passive techniques like quarter wavelength and Helmholtz resonators, and acoustic screens [3] have also been used and can provide high attenuation, though only over narrow frequency bands.

New innovative, ANC techniques for the reduction of engine noise have shown promising results [3-6]. However, industry has been very reluctant to employ these techniques because of the complexity involving combining acoustics, controls, actuator, and sensor design. The number of actuators and sensors required for an ANC system in such a complex sound field results in expensive, heavy, complex, and sometimes-fragile systems. This results in ANC systems that are exceptionally difficult to apply to realistic flight conditions. At takeoff, when turbofan engine noise control is needed most, power

and weight are critical issues. ANC systems are both power consuming and can be heavy. The additional fuel consumption that would result from the increased weight is very unappealing. Thus, the door remains open for a simple, inexpensive, and reliable noise control device, which can control both tonal and broadband noise.

## 1.2 The Herschel-Quincke Tube Concept

The Herschel-Quincke (HQ) tube is a passive control device that uses some of the original noise in the system to produce destructive wave interference. The HQ tube concept is shown in Figure 1-1. A HQ waveguide is a side-duct that travels along the main-duct axis and attaches to the main duct at each end.

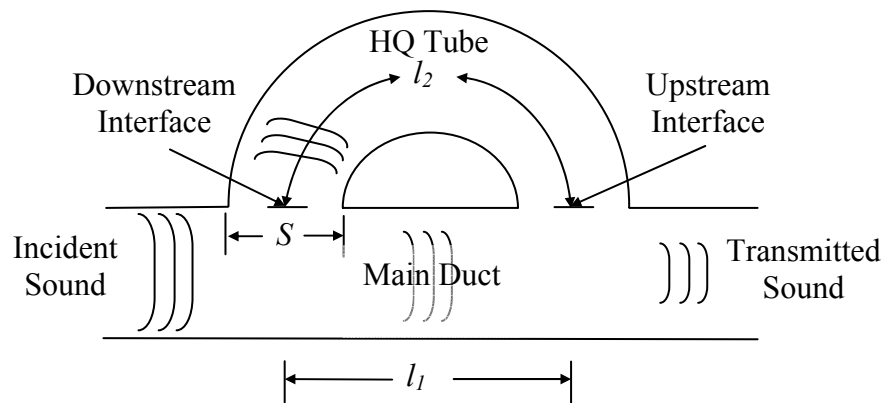


Figure 1-1: The Herschel-Quincke tube concept.

The parameters  $l_2$ ,  $l_1$ , and  $S$  are the length, center-to-center interface distance, and cross sectional area of the HQ tube. A simplified view of the HQ tube concept is that some of the energy in the main duct goes through the HQ tube and then recombines with the remaining energy in the main duct. Since the sound in the HQ tube travels a different length than the sound in the main duct there are frequencies where the sound at the HQ tubes upstream interface is out of phase with the sound in the main duct at the HQ tubes exit. At these frequencies, noise cancellation occurs. These frequencies are controlled by the geometric parameters of the HQ tube. This simplified one-dimensional explanation is only valid for plane waves.

## Chapter 1. Introduction

This concept was first introduced in 1833 by Herschel [7] who theorized that, “No motion is, strictly speaking, annihilated; but it may be divided, and the divided parts made to oppose and, in effect, destroy each other.” He predicted that if the sound of a given pitch is divided into two branches with equal area, one branch being longer than the other by a half of wavelength, when the branches recombine they will be out-of-phase and thus destroy each other. That is, noise cancellation will occur if

$$l_2 - l_1 = (m + 1/2)\lambda \quad (1.1)$$

where  $l_2$  and  $l_1$  and are the lengths of the branches,  $\lambda$  is the acoustic wavelength, and  $m$  is any integer. Herschel’s theory was experimentally confirmed by Quincke [8] in 1866. Stewart [9] improved on Herschel’s theory by observing that noise cancellation also occurs when

$$l_2 + l_1 = n\lambda \quad (1.2)$$

provided that

$$l_2 - l_1 \neq n_1\lambda \quad (1.3)$$

where  $n$  and  $n_1$  are independent integers. Stewart also showed that limited attenuation occurs at other frequencies.

More recently, Selamet continued to work on modeling the HQ tube and removed many of the geometric restrictions of previous work and examined innovated new approaches. Using a three dimensional model that took into account the curvature of the HQ tube Selamet et al. [10] determined that with just a plane wave the one dimensional model, which approximates the tube as being straight is sufficient. Selamet et al. [11], further improved upon the work of Stewart by removing the restriction that the duct branches have equal cross sectional areas. Without this restriction Selamet discovered that the HQ tubes broadband attenuation could be increased and was not limited to narrow spikes. Selamet and Radavich [12] then examined a side branch expansion chamber applied to an HQ tube. They investigated how geometrical variation of the side

branch and HQ tube influenced the resonant frequencies of the system. Another innovated use of the HQ tube by Selamet and Easwaran [13] was to extend the previous analysis of the two-duct HQ tube without flow to a to  $n$ -ducts configuration. They found closed form solutions for the transmission loss and resonance locations for the  $n$ -duct configurations. They also found that the additional branches increased the frequency band and level of noise attenuation.

The effects of flow on the attenuation characteristics of different HQ tube configurations have been investigated by Fuller and Beis [14], Torregrosa, et al. [15], and Zhichi et al. [16]. It was found that peaks of high attenuation were reduced and shifted in the presence of flow.

Up to this point only the effects of plane waves on the HQ tubes had been examined. However, in more complex systems the effects of higher order modes on the HQ tube system is very important. Brady et al. [17] were the first to study the potential of HQ tubes for attenuating higher order modes in two-dimensional ducts. Hallez, et al. [18] expanded the two-dimensional analysis of higher order modes to three-dimensions, i.e. hard walled circular ducts.

Designs based on HQ tubes have received many patents for reducing exhaust noise of internal combustion engines and have been used to study their application on practical problems. Strunk [19] investigated a variation of the HQ tube for hydraulic systems used in off-road earth-moving vehicle fluid power systems. Chen and Hastings [20] used a variation of the HQ tube to examine the ability to reduce fluid-borne noise in power steering hydraulic transmission lines.

### **1.3 Motivation**

Previous HQ tube experiments on the JT15D and AlliedSignal TFE731-60 turbofan engines have shown potential for practical application of this concept. Burdisso and Smith [21] experimentally demonstrated the ability to reduce both tonal and broadband inlet noise using circumferential arrays of HQ tubes applied to the JT15D

engine. Their implementation of the HQ tube concept proved to be simple, reliable, and inexpensive. However, limitations due to the inherent nature of the turbofan engine testing facilities limit the amount of the fundamental research knowledge that could result from a more controlled laboratory environment. Specifically, the difficulty in making detailed mode measurements on turbofan engines prohibits a detailed investigation of the noise control mechanisms of the HQ tubes.

The NASA Langley test facility used in the experiments presented here provided a controlled laboratory environment which allowed accurate and detailed mode measurements, experimental flexibility, and cost efficiency. This facility was superior to those previously used to perform turbofan engine experiments. The HQ tube concepts theoretical model is based on an infinite duct theory, i.e. no reflections. The NASA experimental setup provides a better approximation of this assumption than the previous turbofan engine experiments, which have significant reflections. The experimental conditions are simplified further with the absence of flow in the duct. The NASA experimental setup also allows more experimental flexibility. The use of an acoustic driver array allows control over the circumferential order of the modes generated, while the modes in a turbofan engine are controlled by the rotor-stator interaction. All HQ tube parameters: axial position, number of tubes, and number of arrays can also be varied with ease. The NASA experimental setup also allows the measurement of reflected modes in addition to incident and transmitted modes. Finally, the microphone measurements were made on the wall of the duct instead of the free field.

### **1.4 Objectives and Approach**

Two main objectives will be focused on in this work. The first is to use experimental results to evaluate the accuracy of the VPI analytical model. The second is to provide insight into the noise control mechanisms: reflection, circumferential scattering, and radial scattering of the HQ tubes using experimental results. To obtain these objectives, experiments were performed for different disturbance mode structures,

number of HQ tubes and arrays, and axial positions of the arrays in a controlled laboratory environment. Modal measurements were made upstream and downstream from HQ tube system. Analytical and experimental modal amplitudes, modal power, total power, and reductions were then compared.

### **1.5 Organization**

The remainder of the thesis is separated into four chapters. Chapter 2 provides a brief description of noise in circular ducts. An overview of the theoretical development of the analytical modeling technique is also presented. In Chapter 3, the experimental effort is described in detail. The results of a duct modal analysis are presented. The experimental setup and test procedures are described along with the data analysis and post processing. In Chapter 4, an overview of the experimental results is presented. A microphone signal analysis and modal decomposition results are obtained. The final results and analysis of specific tests are presented in detail. The theoretical and experimental conclusions and future work recommendations are made in Chapter 5.

## **Chapter 2. Review of HQ Tube Modeling Approach**

In order to perform a fundamental study of the HQ tube concept it is necessary to determine the modal amplitudes of all the modes in the duct. The theoretical model reviewed here was developed by Hallez [22] and is simplified with the absence of flow in the duct. First, the sound field in an infinite rigid wall circular duct and the properties of the modes propagating inside them is reviewed. Then, the theoretical modeling technique used to model the HQ tube system is discussed. Next, the modal amplitudes and power are determined from the pressures and velocities determined using the HQ tube model. Finally, a theoretical model is developed to predict incident modal amplitudes.

### **2.1 Modes In Circular Ducts**

The sound field in circular ducts is often very complex and consists of modes that spin clockwise or counterclockwise while traveling upstream or downstream. The cross section of these modes can also have complex pressure distributions that vary both circumferentially and radially. The circumferential order  $m$  and radial order  $n$  of the  $(m,n)$  mode define the number of nodal pressure lines along the radius and around the circumference of the cross section, respectively. Figure 2-1 shows example cross sectional pressure distributions of the  $(m,n)$  modes.

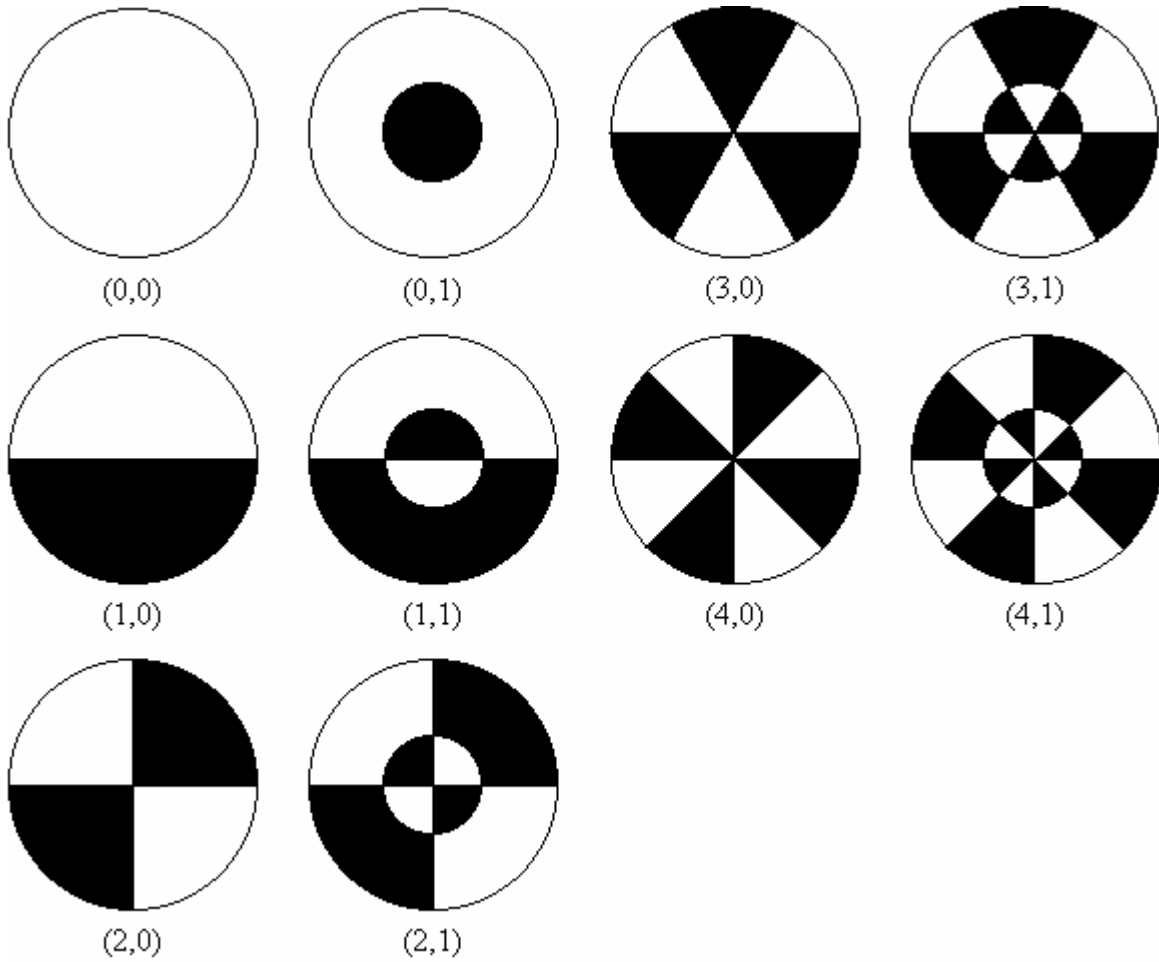


Figure 2-1: Cross sectional pressure distributions of the  $(m,n)$  modes.

The black area of the pressure distribution of the  $(m,n)$  modes represents area that is out of phase with the white area.

The pressure field in an infinite rigid wall circular duct can be described by the contribution of all the propagating modes in the duct. The acoustic wave equation is used to solve the eigenvalue problem and expand the pressure field inside the duct in terms of acoustic modes. The duct with radius  $a$ , is shown in Figure 2-2.

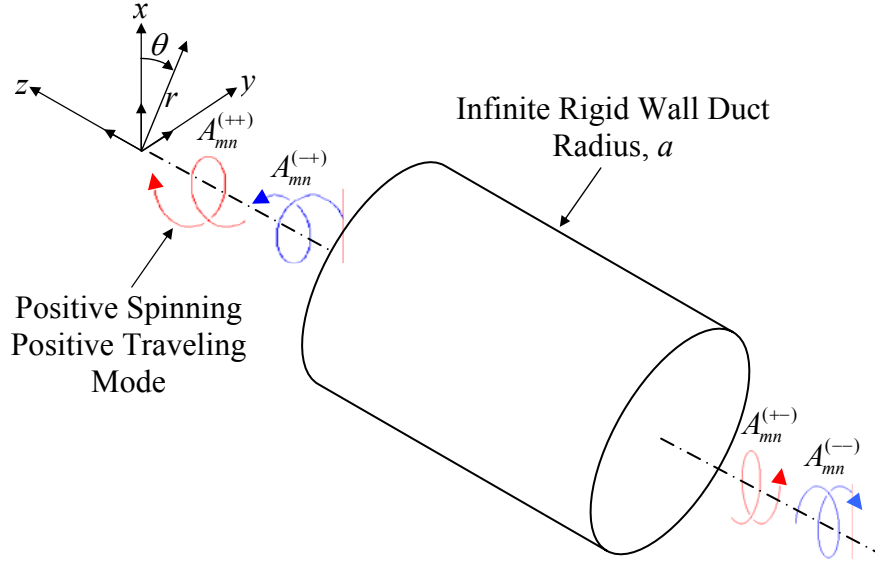


Figure 2-2: Infinite rigid wall duct with spinning and propagating acoustic modes.

The pressure field in the duct is described as the contribution of the positive and negative spinning acoustic modes propagating in both positive and negative  $z$ -direction as depicted in Figure 2-2 by the curved arrows. The pressure at position  $(r, \theta, z)$  in the duct is then given as

$$\begin{aligned}
 p(r, \theta, z, t) = & \left[ \sum_{m=0}^{N_\theta} \sum_{n=0}^{N_r} A_{mn}^{(++)} J_m(k_{mn}r) e^{-im\theta} e^{-ik_{mn,z}z} + \sum_{m=0}^{N_\theta} \sum_{n=0}^{N_r} A_{mn}^{(+)} J_m(k_{mn}r) e^{im\theta} e^{-ik_{mn,z}z} \right. \\
 & \left. + \sum_{m=0}^{N_\theta} \sum_{n=0}^{N_r} A_{mn}^{(+-)} J_m(k_{mn}r) e^{-im\theta} e^{ik_{mn,z}z} + \sum_{m=0}^{N_\theta} \sum_{n=0}^{N_r} A_{mn}^{(-)} J_m(k_{mn}r) e^{im\theta} e^{ik_{mn,z}z} \right] e^{2\pi ft} \quad (2.1)
 \end{aligned}$$

where  $N_\theta$  and  $N_r$  indicate the number of modes included. The coefficient  $A_{mn}^{(st)}$  represents the complex modal amplitude of the  $(m, n)$  mode where the indices  $m$  and  $n$  represent the variation in the circumferential and radial direction of the mode. The acoustic modes in the circular duct could be spinning in the positive or negative  $\theta$ -direction, and traveling in the positive or negative  $z$ -direction, as indicated in Figure 2-2. Thus, the first superscript  $s$  may be  $+$  or  $-$  indicating positive or negative spinning mode, respectively. The second superscript  $t$  may be  $+$  or  $-$  indicating positive or negative traveling direction. For example,  $A_{11}^{(+-)}$  represents the complex modal amplitude of the  $(1, 1)$  mode spinning in the

positive  $\theta$ -direction and traveling in the negative  $z$ -direction. The first kind Bessel function of the  $m^{\text{th}}$  order is defined as  $J_m$  and represents the radial pressure variation of the mode.

Along with different pressure distributions, these modes propagate with different axial velocities. The axial wavenumber for the  $(m,n)$  mode,  $k_{mn,z}$  is expressed as

$$k_{mn,z} = \sqrt{k_o^2 - k_{mn}^2} \quad (2.2)$$

where the free field wavenumber,  $k_o$ , is described as

$$k_o = \frac{2\pi f}{c} \quad (2.3)$$

where  $f$  is the frequency of interest and  $c$  is the speed of sound in air; the eigen-wavenumber  $k_{mn}$  is defined as

$$k_{mn} = \frac{\chi_{mn}}{a} \quad (2.4)$$

where  $\chi_{mn}$  as the inflection point of the first kind Bessel function of the  $m^{\text{th}}$  order. For each  $m$ -order there are  $n$  solutions that satisfy this equation, corresponding to each radial order mode. The values of  $\chi_{mn}$  satisfy the hard wall boundary condition that requires zero radial particle velocity at the duct walls. The propagation characteristics of the modes are defined by the value of  $k_{mn,z}$  in equation (2.2). If  $k_{mn,z}$  is real, the mode propagates and is referred as been cut-on and if  $k_{mn,z}$  is imaginary, the mode is decaying and is indicated as been cut-off.

The frequency that modes change from decaying to propagating is called the cut-off frequency. The cut-off frequency of the  $(m,n)$  mode is then defined as

$$f_{mn,\text{cut-off}} = \frac{c}{2} k_{mn} \quad (2.5)$$

If the driving frequency of the system is larger than the cut-off frequency of the  $(m,n)$  mode, the mode is cut-on and will propagate. However, if the driving frequency is less than the cut-off frequency, the mode is cut-off and will decay exponentially. The plane wave  $(0,0)$  mode is always cut-on with additional higher order modes becoming cut-on as the driving frequency is increased.

## 2.2 HQ Tube Modeling Technique

In this section the theoretical model used to predict the effects of the HQ tube system applied to the infinite rigid wall circular duct in Figure 2-2 is briefly reviewed. Key equations are presented here, a more detailed derivation can be found in Hallez [22]. First, the sound field inside the HQ tubes is defined in the form of propagating plane waves. Next, the sound fields in the circular duct and HQ tubes are coupled by matching their pressure and particle velocity at the interfaces between the duct and the HQ tubes. Finally, expressions for modal amplitudes and power are developed.

The cylindrical coordinate system  $(r, \theta, z)$  used in the theoretical model applied to an infinite rigid wall circular duct with HQ tube system, is shown in Figure 2-3.

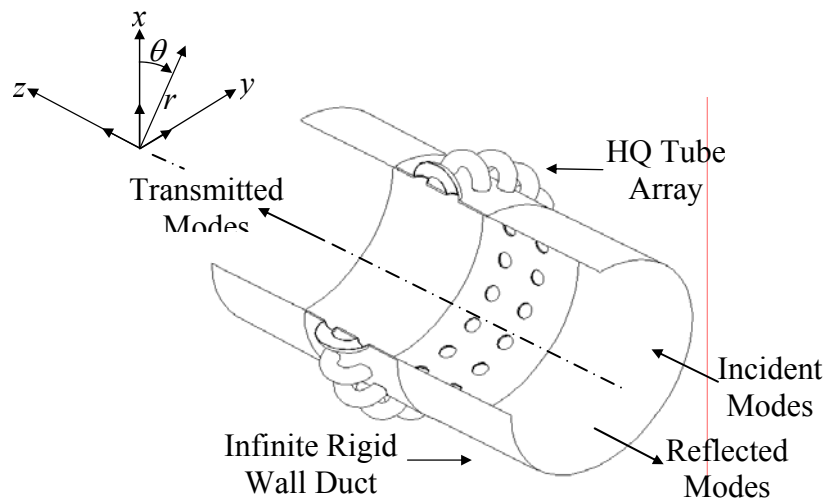


Figure 2-3: Model of infinite rigid wall circular duct with HQ tube system.

Without loss of generality, it is assumed that the disturbance creates incident modes that propagate in the positive  $z$ -direction. At the HQ tube array interface some of the energy of the incident modes is transmitted in the positive  $z$ -direction. In addition, some of the energy is reflected in the negative  $z$ -direction.

### 2.2.1 Duct Dynamics

First, the sound field in the duct due to the HQ tubes is determined. The HQ tube duct interfaces are modeled as piston sources, as shown in Figure 2-4.

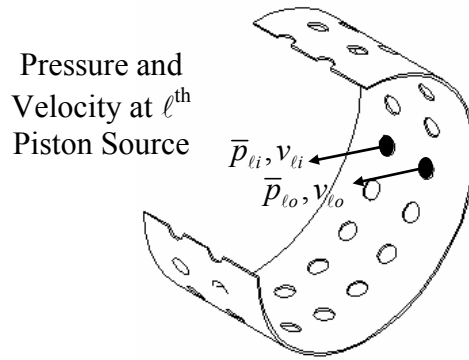


Figure 2-4: Model of duct with finite piston sources.

The average pressure over each piston source can be expressed as summation of the pressure due to each source and the disturbance and is written as

$$\begin{Bmatrix} \bar{p}_{1i} \\ \bar{p}_{1o} \\ \vdots \\ \bar{p}_{\ell i} \\ \bar{p}_{\ell o} \\ \vdots \\ \bar{p}_{Ni} \\ \bar{p}_{No} \end{Bmatrix} = \begin{bmatrix} Z_{1i1i} & Z_{1i1o} & Z_{1i2i} & Z_{1i2o} & \dots & Z_{1iNi} & Z_{1iNo} \\ Z_{1o1i} & Z_{1o1o} & Z_{1o2i} & Z_{1o2o} & \dots & Z_{1oNi} & Z_{1oNo} \\ \vdots & \vdots & \vdots & \vdots & \vdots & \vdots & \vdots \\ Z_{\ell i\ell i} & Z_{\ell i\ell o} & \dots & \dots & \dots & \dots & \dots \\ Z_{\ell o\ell i} & Z_{\ell o\ell o} & \dots & \dots & \dots & \dots & \dots \\ \vdots & \vdots & \vdots & \vdots & \vdots & \vdots & \vdots \\ Z_{Ni1i} & Z_{Ni1o} & \dots & \dots & \dots & Z_{NiNi} & Z_{NiNo} \\ Z_{No1i} & Z_{No1o} & \dots & \dots & \dots & Z_{NoNi} & Z_{NoNo} \end{bmatrix} \begin{Bmatrix} v_{1i} \\ v_{1o} \\ \vdots \\ v_{\ell i} \\ v_{\ell o} \\ \vdots \\ v_{Ni} \\ v_{No} \end{Bmatrix} + \begin{Bmatrix} \bar{p}_{1i}^d \\ \bar{p}_{1o}^d \\ \vdots \\ \bar{p}_{\ell i}^d \\ \bar{p}_{\ell o}^d \\ \vdots \\ \bar{p}_{Ni}^d \\ \bar{p}_{No}^d \end{Bmatrix} \quad (2.6)$$

Where  $\bar{p}_{\ell i}$  and  $\bar{p}_{\ell o}$  and  $v_{\ell i}$  and  $v_{\ell o}$  are the average pressure and velocity of the input and output of the  $\ell^{th}$  tube and  $N$  is the total number of HQ tubes. The impedance  $Z_{r*s*}$ , relates the average pressure over source  $r$  due to another source  $s$  with unit velocity. Where the subscript \* may be  $i$  or  $o$  indicating input or output of the source, respectively. The average pressure at the input and output of the  $\ell^{th}$  tube due to the positive spinning and traveling disturbance modes is  $\bar{p}_{\ell i}^d$  and  $\bar{p}_{\ell o}^d$ , respectively. Expressions for these variables may be found in Hallez [22].

### 2.2.2 HQ Tube Dynamics

The sound field inside the HQ tubes is described here. A model for one HQ tube is developed and used to build a matrix which models the entire HQ tube array. Figure 2-5 shows a model of a HQ tube with perforated screens.

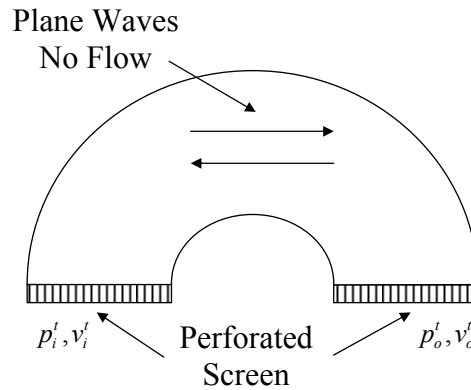


Figure 2-5: Model of HQ tubes.

The HQ tubes are semi-circle in shape, however a straight tube is used since it is assumed only plane waves propagate in the tube. The tube ends are modeled as piston sources and no flow is assumed inside the tube. Perforated screens are used at the HQ tube ends to be consistent with practical implementation. In cases with flow they are used to minimize flow distortion due to the tube openings in the duct.

## Chapter 2. Review of HQ Tube Modeling Approach

The transfer function matrix relating the pressure and particle velocity at the tube ends, including the effects of the perforated screens, is written as

$$\begin{Bmatrix} p_{\ell i}^t \\ p_{\ell o}^t \end{Bmatrix} = \begin{bmatrix} Z_{ii}^{\ell} & Z_{io}^{\ell} \\ Z_{oo}^{\ell} & Z_{oi}^{\ell} \end{bmatrix} \begin{Bmatrix} v_{\ell i}^t \\ v_{\ell o}^t \end{Bmatrix} \quad (2.7)$$

where  $p_{\ell i}^t$  and  $p_{\ell o}^t$  and  $v_{\ell i}^t$  and  $v_{\ell o}^t$  are the pressure and velocity of the input and output of the  $\ell^{\text{th}}$  tube. The impedance  $Z_{**}^{\ell}$  relates the average pressure over one end of tube  $\ell$ , due to the same end or the other end with unit velocity. Where the subscript \* may be  $i$  or  $o$  indicating input or output of the source, respectively.

Now that the model of each HQ tube is developed individually, they can be assembled together to model the circumferential array of HQ tubes. Figure 2-6 shows the model of the HQ tube array.

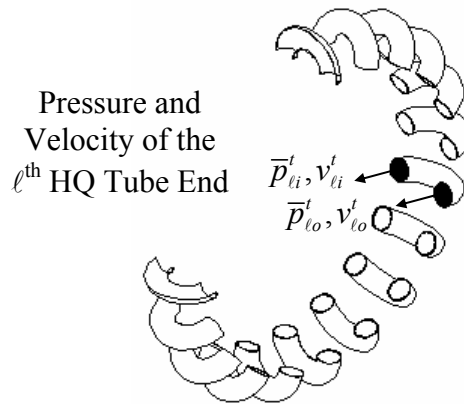


Figure 2-6: HQ tube array model.

The average pressure at the tube ends of the entire HQ tube array due to the dynamics in the duct is written in matrix form as

$$\begin{pmatrix} \bar{p}_{1i}^t \\ \bar{p}_{1o}^t \\ \vdots \\ \bar{p}_{\ell i}^t \\ \bar{p}_{\ell o}^t \\ \vdots \\ \bar{p}_{Ni}^t \\ \bar{p}_{No}^t \end{pmatrix} = \begin{bmatrix} Z_{ii}^{t1} & Z_{io}^{t1} & 0 & 0 & & & 0 & 0 \\ Z_{oi}^{t1} & Z_{oo}^{t1} & 0 & 0 & \cdots & & 0 & 0 \\ 0 & 0 & & & & & & \\ 0 & 0 & & & & & & \\ \vdots & \vdots & & & Z_{ii}^{t\ell} & Z_{io}^{t\ell} & & \\ & & & & Z_{oi}^{t\ell} & Z_{oo}^{t\ell} & & \\ & & & & & & & \\ & & & & & & & \\ & & & & & & & \\ & & & & & & & \\ 0 & 0 & & & & & Z_{ii}^{tN} & Z_{io}^{tN} \\ 0 & 0 & \cdots & & & & Z_{oi}^{tN} & Z_{oo}^{tN} \end{bmatrix} \begin{pmatrix} v_{1i}^t \\ v_{1o}^t \\ \vdots \\ v_{\ell i}^t \\ v_{\ell o}^t \\ \vdots \\ v_{Ni}^t \\ v_{No}^t \end{pmatrix} \quad (2.8)$$

where  $\bar{p}_{\ell i}^t$  and  $\bar{p}_{\ell o}^t$  are the average pressure of the input and output of the  $\ell^{\text{th}}$  tube.

Expressions for these variables may be found in Hallez [22].

### 2.2.3 Coupled HQ Tube–Duct System

The HQ tube and duct systems developed previously are now coupled. The boundary conditions state that the pressure and particle velocity at the HQ tube-duct interfaces must be matched. Thus,

$$\begin{aligned} \bar{p}_{\ell i} &= \bar{p}_{\ell i}^t \quad \text{and} \quad \bar{p}_{\ell o} = \bar{p}_{\ell o}^t \\ v_{\ell i} &= v_{\ell i}^t \quad \text{and} \quad v_{\ell o} = v_{\ell o}^t \end{aligned} \quad (2.9)$$

The pressures at the HQ tube-duct interfaces are matched by replacing equation (2.8) into the left-hand side of equation (2.6). The particle velocities are then matched and solved for which yields



mechanisms of the HQ tube to be examined. This also allows for direct comparison of the analytical and experimental results.

### 2.3.1 Modal Amplitudes

The transmitted pressure at any point in the duct can be expressed as a summation of the positive and negative spinning acoustic modes propagating in the positive  $z$ -direction. Thus, the transmitted pressure is

$$p_{trans}(r, \theta, z) = \sum_{m=0}^{M_g} \sum_{n=0}^{N_g} A_{mn}^{(++)} J_m(k_{mn} r) e^{-im\theta} e^{-ik_{mn,z}^{(+)} z} + \sum_{m=0}^{M_g} \sum_{n=0}^{N_g} A_{mn}^{(-+)} J_m(k_{mn} r) e^{im\theta} e^{-ik_{mn,z}^{(+)} z} \quad (2.11)$$

where  $A_{mn}^{++}$  is due to both the disturbance and piston sources and  $A_{mn}^{-+}$  is due only to the piston sources. The complex modal amplitude of the transmitted modes in the duct are written as

$$A_{mn}^{++} = A_{mn,d}^{(++)} + \sum_{r=1}^{N_s} A_{mn,r}^{(++)} \quad (2.12)$$

$$A_{mn}^{-+} = \sum_{r=1}^{N_s} A_{mn,r}^{(-+)}$$

where  $A_{mn,d}^{(++)}$  is the modal amplitude of the disturbance. Using Green's function the complex modal amplitudes due to source  $r$  are expressed as

$$A_{mn,r}^{(++)} = \frac{v_r k_o \rho c}{\pi a^2} \frac{J_m(k_{mn} a)}{\Lambda_{mn}(k_{mn,z}^{(+)} - k_{mn,z}^{(-)})} \frac{2a\alpha_r \sin(m\alpha_r)}{m\alpha_r} \frac{2d_r \sin(k_{mn,z}^{(+)} d_r)}{k_{mn,z}^{(+)} d_r} e^{ik_{mn,z}^{(+)} z_r} \frac{e^{+im\theta_r}}{2} \quad (2.13)$$

$$A_{mn,r}^{(-+)} = \frac{v_r k_o \rho c}{\pi a^2} \frac{J_m(k_{mn} a)}{\Lambda_{mn}(k_{mn,z}^{(+)} - k_{mn,z}^{(-)})} \frac{2a\alpha_r \sin(m\alpha_r)}{m\alpha_r} \frac{2d_r \sin(k_{mn,z}^{(+)} d_r)}{k_{mn,z}^{(+)} d_r} e^{ik_{mn,z}^{(+)} z_r} \frac{e^{-im\theta_r}}{2} \quad (2.14)$$

For the  $m=0$  mode which is non-spinning,  $A_{0n,r}^{(++)} = A_{0n,r}^{(-+)}$  and the equation simplifies to

$$A_{0n,r}^{(++)} = \frac{v_r k_o \rho c}{\pi a^2} \frac{J_0(k_{0n} a)}{\Lambda_{0n}(k_{mn,z}^{(+)} - k_{mn,z}^{(-)})} 2a\alpha_r \frac{2d_r \sin(k_{mn,z}^{(+)} d_r)}{k_{mn,z}^{(+)} d_r} e^{ik_{mn,z}^{(+)} z_r} \quad (2.15)$$

Similarly, the reflected pressure at any point in the duct can be expressed as a summation of the positive and negative spinning acoustic modes propagating in the negative  $z$ -direction. There is no negative traveling disturbance modes, thus the pressure is only due to the piston sources and may be expressed as

$$p_{ref}(r, \theta, z) = \sum_{m=0}^{M_g} \sum_{n=0}^{N_g} A_{mn,r}^{(+)} J_m(k_{mn} r) e^{-im\theta} e^{ik_{mn,z} z} + \sum_{m=0}^{M_g} \sum_{n=0}^{N_g} A_{mn,r}^{(-)} J_m(k_{mn} r) e^{im\theta} e^{ik_{mn,z} z} \quad (2.16)$$

where the complex modal amplitude of the reflected modes in the duct are written as

$$A_{mn}^{+-} = \sum_{r=1}^{N_s} A_{mn,r}^{(+)} \quad (2.17)$$

$$A_{mn}^{--} = \sum_{r=1}^{N_s} A_{mn,r}^{(-)}$$

where the complex modal amplitudes due to source  $r$  are shown as

$$A_{mn,r}^{(+)} = \frac{v_r k_o \rho c}{\pi a^2} \frac{J_m(k_{mn} a)}{\Lambda_{mn}(k_{mn,z}^{(+)} - k_{mn,z}^{(-)})} \frac{2a\alpha_r \sin(m\alpha_r)}{m\alpha_r} \frac{2d_r \sin(k_{mn,z}^{(-)} d_r)}{k_{mn,z}^{(-)} d_r} e^{ik_{mn,z}^{(-)} z_r} \frac{e^{+im\theta_r}}{2} \quad (2.18)$$

$$A_{mn,r}^{(-)} = \frac{v_r k_o \rho c}{\pi a^2} \frac{J_m(k_{mn} a)}{\Lambda_{mn}(k_{mn,z}^{(+)} - k_{mn,z}^{(-)})} \frac{2a\alpha_r \sin(m\alpha_r)}{m\alpha_r} \frac{2d_r \sin(k_{mn,z}^{(-)} d_r)}{k_{mn,z}^{(-)} d_r} e^{ik_{mn,z}^{(-)} z_r} \frac{e^{-im\theta_r}}{2} \quad (2.19)$$

For the  $m=0$  mode which is non-spinning,  $A_{0n,r}^{(+)} = A_{0n,r}^{(-)}$  and the equation simplifies to

$$A_{0n,r}^{(+)} = \frac{v_r k_o \rho c}{\pi a^2} \frac{J_0(k_{0n} a)}{\Lambda_{0n}(k_{mn,z}^{(+)} - k_{mn,z}^{(-)})} 2a\alpha_r \frac{2d_r \sin(k_{mn,z}^{(-)} d_r)}{k_{mn,z}^{(-)} d_r} e^{ik_{mn,z}^{(-)} z_r} \quad (2.20)$$

The total pressure at  $(r, \theta, z)$  in the duct can be expressed as a combination of the transmitted and reflected pressure. That is

$$\begin{aligned}
 p(r, \theta, z) = & \sum_{m=0}^{N_\theta} \sum_{n=0}^{N_r} A_{mn}^{(++)} J_m(k_{mn} r) e^{-im\theta} e^{-ik_{mn,z}^{(+)} z} + \sum_{m=0}^{N_\theta} \sum_{n=0}^{N_r} A_{mn}^{(-+)} J_m(k_{mn} r) e^{im\theta} e^{-ik_{mn,z}^{(+)} z} \\
 & + \sum_{m=0}^{N_\theta} \sum_{n=0}^{N_r} A_{mn}^{(+-)} J_m(k_{mn} r) e^{-im\theta} e^{ik_{mn,z}^{(-)} z} + \sum_{m=0}^{N_\theta} \sum_{n=0}^{N_r} A_{mn}^{(--)} J_m(k_{mn} r) e^{im\theta} e^{ik_{mn,z}^{(-)} z}
 \end{aligned} \tag{2.21}$$

### 2.3.2 Modal Sound Power

The radiated sound power of each mode can now be computed from the modal amplitudes. Without flow, the acoustic intensity in the  $z$ -direction is written as

$$I_z = \frac{1}{2} \text{Re al} [p v_z^*] \tag{2.22}$$

where  $p$  is pressure,  $v_z$  is the particle velocity in the  $z$ -direction, and asterisk (\*) indicates complex conjugate. The acoustic power is obtained integrating over the cross sectional area of the duct

$$W = \int_0^a \int_0^{2\pi} I_z r dr d\theta \tag{2.23}$$

This results in the total transmitted and reflected sound power of the form

$$W_{trans} = \sum_{m=0}^{N_\theta} \sum_{n=0}^{N_r} W_{mn}^{(++)} + \sum_{m=0}^{N_\theta} \sum_{n=0}^{N_r} W_{mn}^{(-+)} \tag{2.24}$$

$$W_{ref} = \sum_{m=0}^{N_\theta} \sum_{n=0}^{N_r} W_{mn}^{(+-)} + \sum_{m=0}^{N_\theta} \sum_{n=0}^{N_r} W_{mn}^{(--)} \tag{2.25}$$

where the sound power of each propagating mode in the duct expressed in terms of modal amplitudes is

## Chapter 2. Review of HQ Tube Modeling Approach

$$W_{mn}^{(++)} = \frac{\pi a^2 \Lambda_{mn}}{\rho c} |A_{mn}^{(++)}|^2 \left( \frac{k_{mn,z}^{(+)}}{k_o} \right),$$

$$W_{mn}^{(-+)} = \frac{\pi a^2 \Lambda_{mn}}{\rho c} |A_{mn}^{(-+)}|^2 \left( \frac{k_{mn,z}^{(+)}}{k_o} \right),$$

$$W_{mn}^{(+)} = \frac{\pi a^2 \Lambda_{mn}}{\rho c} |A_{mn}^{(+)}|^2 \left( \frac{k_{mn,z}^{(-)}}{k_o} \right),$$

and

$$W_{mn}^{(-)} = \frac{\pi a^2 \Lambda_{mn}}{\rho c} |A_{mn}^{(-)}|^2 \left( \frac{k_{mn,z}^{(-)}}{k_o} \right) \quad (2.26)$$

The orthogonality constant is given as

$$\Lambda_{mn} = \begin{cases} J_m^2(k_{mn}a) & \text{if } m = 0 \\ \frac{1}{2} \left[ 1 - \frac{m^2}{(k_{mn}a)^2} \right] J_m^2(k_{mn}a) & \text{if } m \neq 0 \end{cases} \quad (2.27)$$

The analytical modal amplitudes and power for each mode in the duct can now be determined. Experiments designed to evaluate the accuracy of the analytical model results are presented in Chapter 3. Comparisons of the experimental and analytical results are shown in Chapter 4.

## **Chapter 3. Experimental Effort**

In this chapter, description of the experimental setup and data analysis and post processing of the experimental measurements are described. The experimental setup and HQ tube system configurations are examined and details of the noise source, HQ tube system, and microphones are reviewed. A modal analysis is performed for determining the modes present in the duct for each case. Then, the data analysis and post processing procedure of the microphone measurements are presented. The modal decomposition technique used to obtain the modal amplitudes in the duct from the pressure measurements on the duct wall is developed. The orthogonality assumption used in the modal decomposition is examined. The modal decomposition technique is used in Chapter 4 to view the pressure measurements on a modal level. This enables direct comparison to the analytical model and examination of the noise control mechanisms of the HQ-tube system.

### **3.1 Experimental Setup**

The experimental testing was performed at NASA Langley Research Center in Hampton Virginia. The NASA Langley testing facility and test rig provided a controlled laboratory environment with the ability to generate and measure acoustic modes for testing with the HQ tube system. Multiple test configurations were developed to allow investigation of the noise control mechanisms of the HQ tubes and evaluation of the VPI analytical model. Measurements were taken without and the HQ tube system in order to

measure all of the acoustic modes in the duct, i.e. incident, transmitted, and reflected modes. A picture of the NASA facility is shown in Figure 3.1.

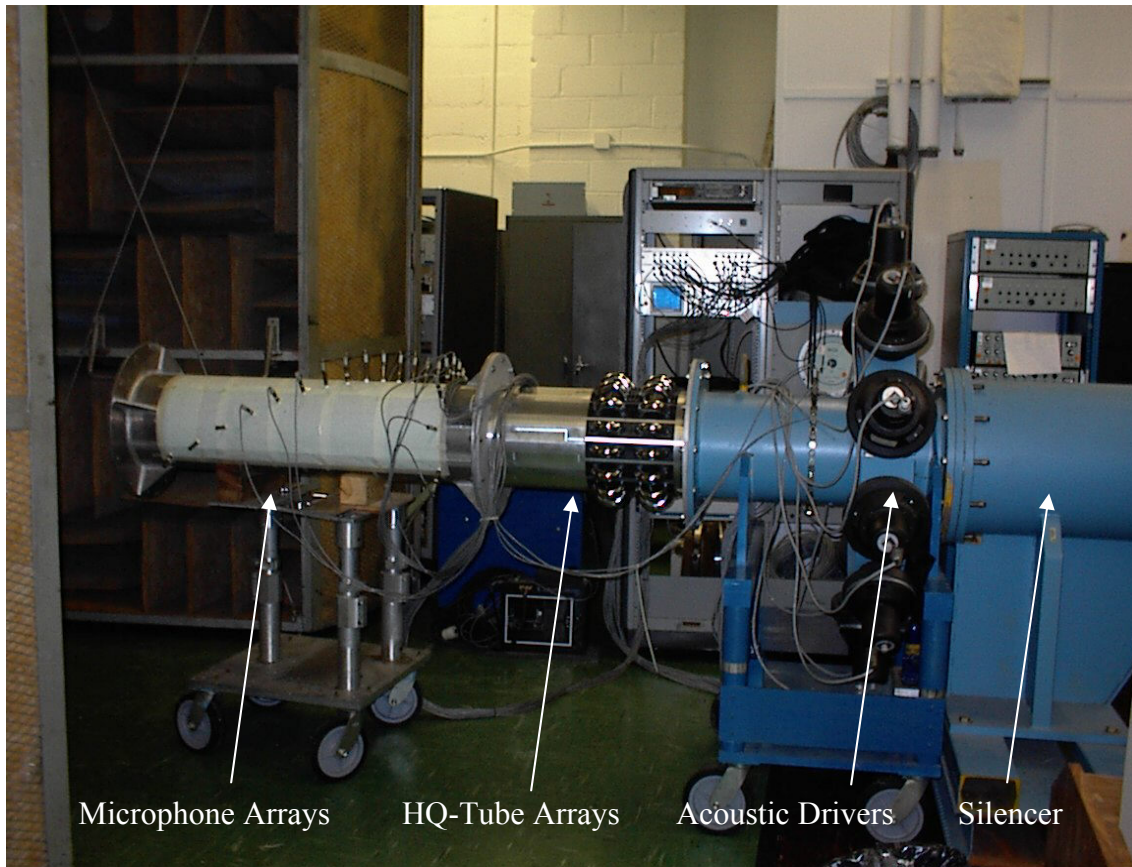


Figure 3-1: NASA Langley Research Center testing facility.

### 3.1.1 Noise Sources

An array of acoustic drivers was used to create circumferential-order disturbance modes. The 12 acoustic drivers are equally spaced 30 degrees apart around the circumference of the duct as shown in shown in Figure 3-2.



Figure 3-2: Array of 12 equally spaced acoustic drivers.

The acoustic drivers are full bandwidth drivers that funnel down to a 3.81 by 10.16 cm hole in the duct wall.

In order to produce specific disturbance modes in the duct, white noise was generated from a signal generator of a spectrum analyzer. The white noise was then band pass filtered with low and high pass filters placed at 100 Hz and 5000 Hz, respectively. Circumferential-order disturbance modes,  $m$  were then generated using a phase controller that assigned an amplified, filtered, white noise signal with equal magnitude and phase of  $\phi_r$  to the  $r^{th}$  acoustic driver. The phase  $\phi_r$  is given as

$$\phi_r = \frac{m(2\pi)(r-1)}{12} \quad r=1,2,\dots,12 \quad (3.1)$$

Therefore, the required phase in radians for each acoustic driver  $r$ , to generate a specific disturbance mode  $m$ , is shown in Table 3-1.

Acoustic Driver, $r$	Disturbance $m$ -order				
	0	1	2	3	4
1	0.00	0.00	0.00	0.00	0.00
2	0.00	0.52	1.05	1.57	2.09
3	0.00	1.05	2.09	3.14	4.19
4	0.00	1.57	3.14	4.71	6.28
5	0.00	2.09	4.19	6.28	8.38
6	0.00	2.62	5.24	7.85	10.47
7	0.00	3.14	6.28	9.42	12.57
8	0.00	3.67	7.33	11.00	14.66
9	0.00	4.19	8.38	12.57	16.76
10	0.00	4.71	9.42	14.14	18.85
11	0.00	5.24	10.47	15.71	20.94
12	0.00	5.76	11.52	17.28	23.04

Table 3-1: The required phase in radians for each acoustic driver  $r$ , to generate a specific disturbance mode  $m$ .

Circumferential-orders of  $m=0$  through  $m=4$  were tested.

### 3.1.2 HQ Tube Systems

The HQ tube system presented here was designed to allow insight into all three noise control mechanisms: reflection, circumferential scattering, and radial scattering. In addition, it was designed to evaluate the HQ tube analytical models ability to predict the effects of changing various parameters in the HQ tube system. Knowledge gained from the modal analysis and analytical model predictions were used to determine the design of the HQ tube system characteristics. The HQ tube system is shown in Figure 3-3.

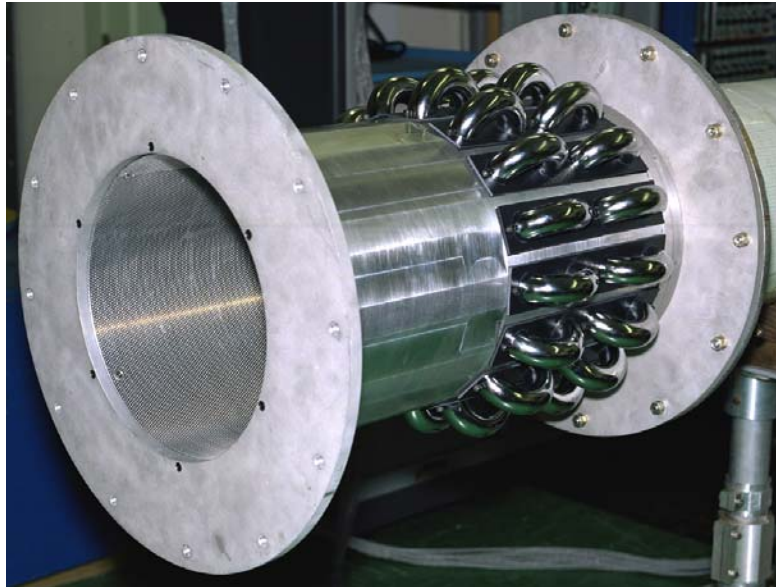


Figure 3-3: HQ tube system.

To preserve the circumferential variation of the sound field in the duct, HQ tubes were evenly spaced around the circumference. Arrays of 8 and 16 HQ tubes were chosen over other HQ tube combinations because of their ability to provide both circumferential and radial scattering in the system. Circumferential arrays of 8 HQ tubes are obtained by covering every other HQ tube in the array with aluminum tape. Circumferential scattering of modes is due to the spatial aliasing of the HQ tubes. At the HQ tube array interface some of the energy of the incident modes spill into other circumferential orders. Radial scattering of modes occurs when multiple radial modes are cut-on for one circumferential order. Energy from one radial order is scattered into other cut-on radial orders.

Two arrays of HQ tubes were chosen to allow investigation into the effects of multiple arrays and different axial positions on the system. Covering up one of the two arrays with aluminum tape results in a single array of HQ tubes that may also be tested. Rotating the HQ tube system 180 deg. about its center cross-section provides a possible four HQ tube array axial positions.

The geometry of each HQ tube in the array was designed to provide simplicity in fabrication and two system resonance's in the frequency range of interest. A single HQ tube is shown in Figure 3-4.

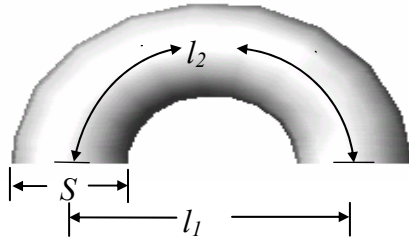


Figure 3-4: HQ tube design.

The resonance of a tube that is open at both ends occurs when the wavelength  $\lambda$  of a plane wave satisfies the condition

$$\lambda = \frac{2\ell_2}{p}, p = 1, 2, 3, \dots \quad (3.2)$$

Using the HQ tube geometrical design parameter values listed in Table 3-2, this results in the first and second resonance frequencies of the tubes as 1,340 and 2,680 Hz, respectively.

HQ Tube Design	
Center to Center Distance, $l_1$	7.80 cm
Tube Length, $l_2$	12.80 cm
Tube Area, $S$	7.15 cm <sup>2</sup>
1 <sup>st</sup> Tube Resonance	1,340 Hz
2 <sup>nd</sup> Tube Resonance	2,680 Hz

Table 3-2: HQ tube design parameters.

A perforated screen is used at the HQ tube ends to be consistent with practical implementation. In cases with flow they are used to minimize flow distortion due to the discontinuity due to the HQ tube-duct wall interface. The screen has a thickness of 0.762 m, orifice radius of 0.762 m, and open area ratio of 25%. Figure 3-5 shows the HQ tube system with and without the perforated screen.

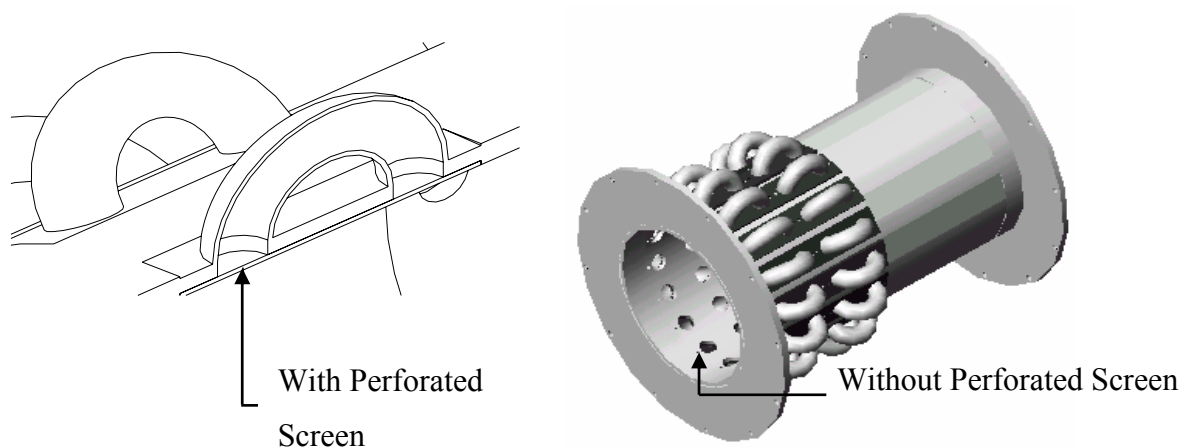


Figure 3-5: HQ tube system with and without the perforated screen.

### 3.1.3 Microphone Arrays

Pressure measurements of the acoustic modes in the duct were taken with two arrays of microphones located on the duct wall. The microphone arrays are shown in Figure 3-6.

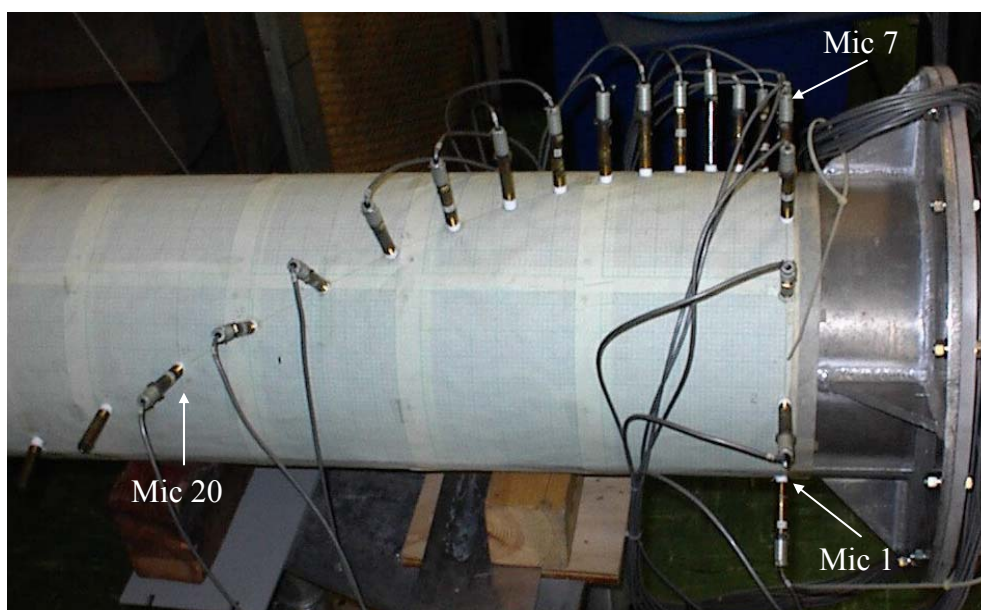


Figure 3-6: Logarithmically spaced circumferential and helical microphone arrays located on the duct wall.

Microphones 1 through 7 were logarithmically spaced around the circumference of the duct. Microphones 8 through 20 were logarithmically spaced in a helix around the duct. The axial and angular positions of the microphones located on the duct wall are listed in

### Chapter 3. Experimental Effort

Table 3-3. The axial and angular microphone positions are referenced to the microphone duct entrance and cross section top, respectively. To be consistent with the sign convention used in this analysis clockwise is defined as the positive angular direction.

	Microphone	Axial Position (cm)	Angular Position (deg)
Circumferential Array	1	13.34	-122.0
	2	13.34	-85.5
	3	13.34	-57.6
	4	13.34	-36.9
	5	13.34	-20.7
	6	13.34	-9.0
	7	13.34	0.0
Helical Array	8	15.62	-4.3
	9	18.29	-9.3
	10	21.08	-14.5
	11	24.26	-20.4
	12	27.81	-27.1
	13	31.75	-34.5
	14	36.20	-42.8
	15	40.89	-51.6
	16	46.36	-61.7
	17	52.32	-72.6
	18	58.93	-85.2
	19	66.29	-99.0
	20	74.42	-114.2

Table 3-3: Axial and angular microphone positions.

### 3.1.4 Silencer

A silencer with a length of 4 m is shown in Figure 3-7 and was used as an anechoic termination to minimize the reflections in the duct.

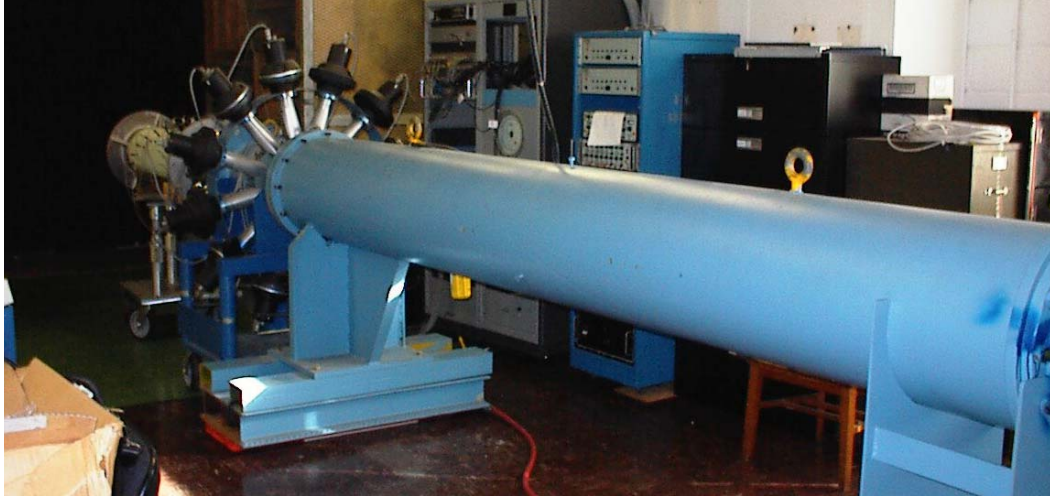


Figure 3-7: Silencer used to minimize reflections in the duct.

The silencer was used to limit reflections from the open end and allow the experimental system to better approximate the infinite duct assumption made in the theoretical model.

### 3.1.5 Test Configurations

The two experimental configurations used to obtain pressure measurements of the incident, transmitted, and reflected modes in the duct are shown in Figure 3-8 and Figure 3-9.

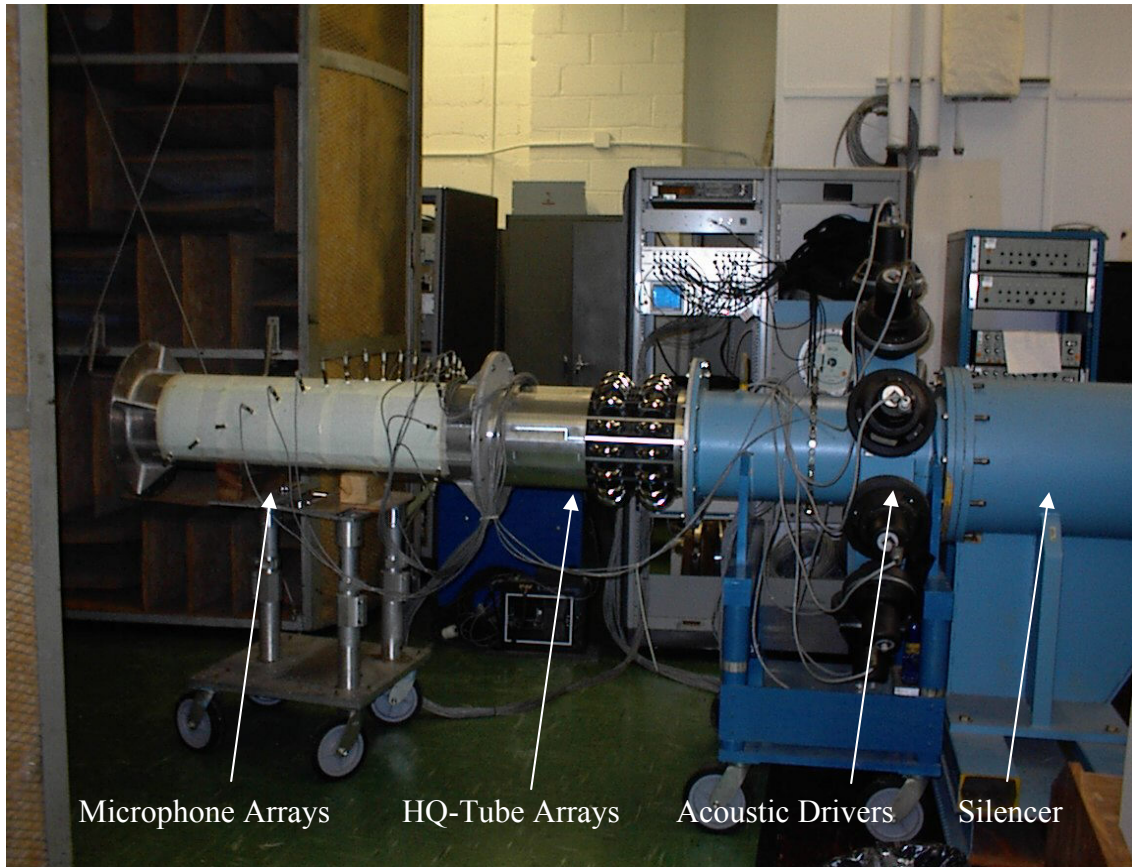


Figure 3-8: NASA Langley Research Center testing facility. Incident and transmitted mode measurement test rig.

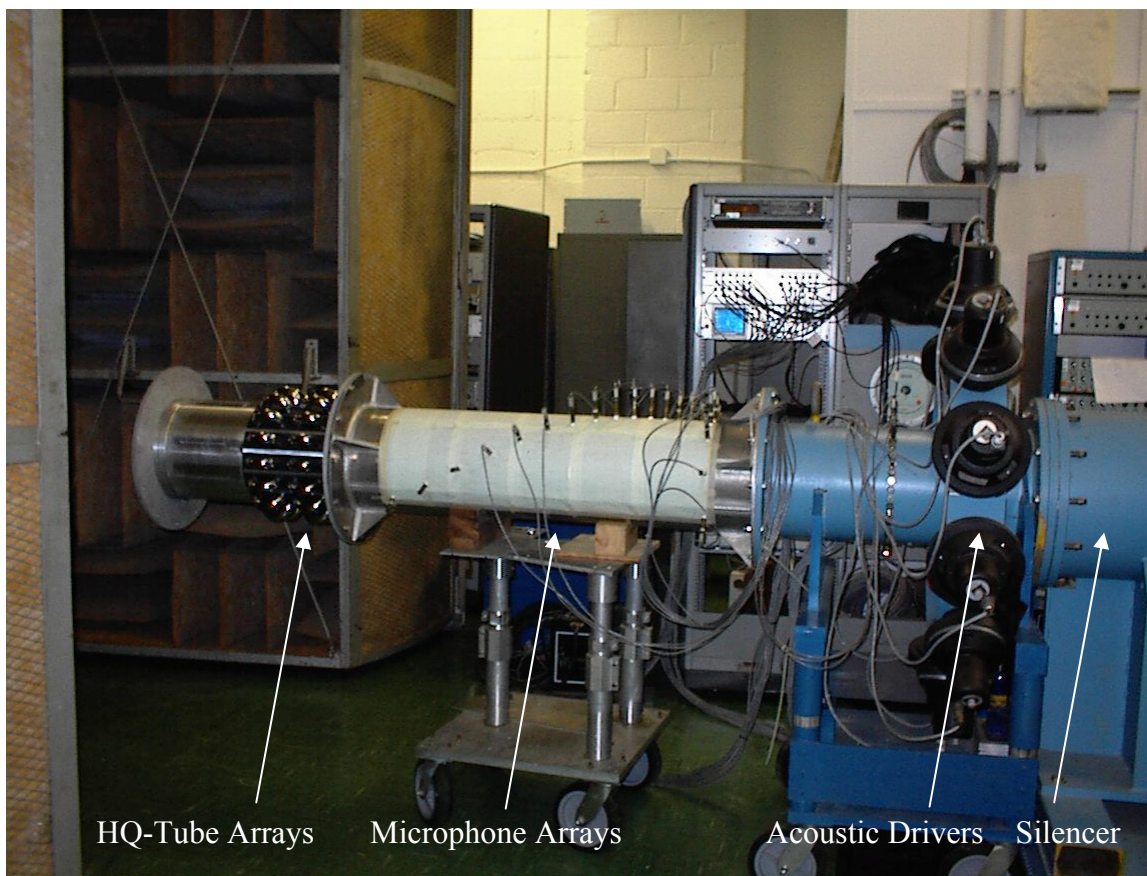


Figure 3-9. NASA Langley Research Center testing facility and reflected mode measurement test rig.

In both configurations an array of acoustic drivers was used to generate circumferential order disturbance modes that propagated throughout the 0.30 m diameter duct. The acoustic energy that propagates towards the open end (toward the left in Figure 3-8) of the acoustic drivers encounters the HQ tube array interface. At this interface some of the energy of the incident modes is transmitted upstream of the HQ tubes and some is reflected downstream.

It is necessary to obtain pressure measurements of all the acoustic modes in the duct: incident, transmitted, and reflected. Incident mode pressure measurements were obtained by creating a hard wall condition in the duct. The HQ tube arrays were covered up with aluminum tape and pressure measurements were taken with the microphone arrays. Transmitted mode pressure measurements were obtained by placing the HQ tube arrays downstream of the microphone arrays, as seen in Figure 3-8. Conversely, reflected mode pressure measurements were obtained by placing the HQ tube arrays upstream of

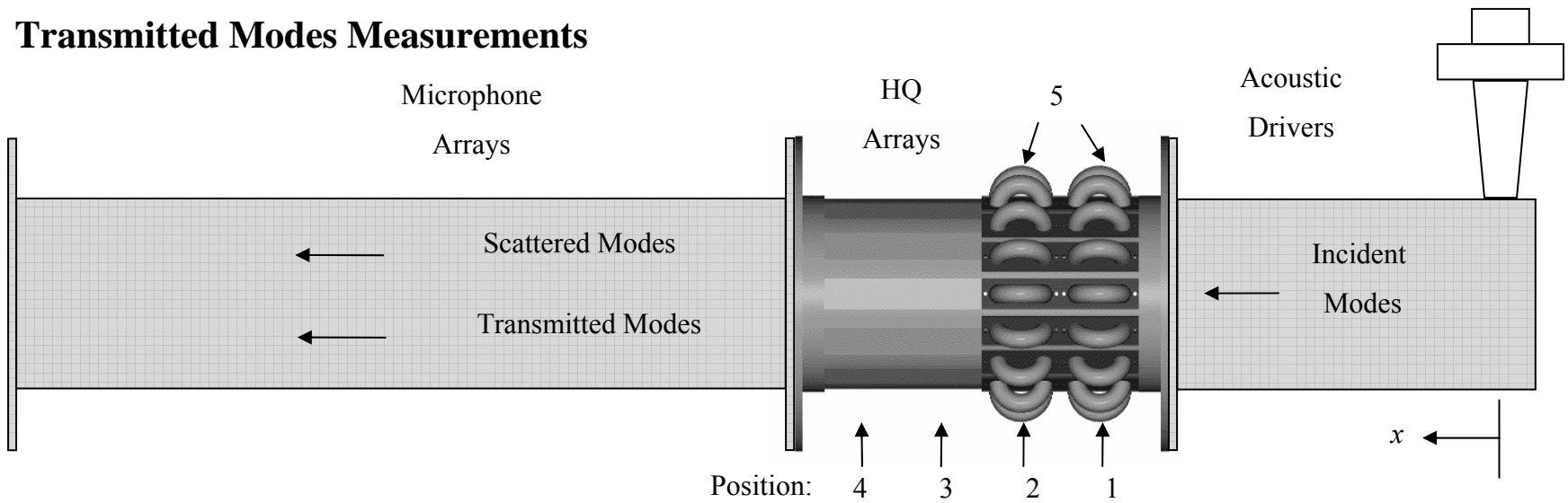
### Chapter 3. Experimental Effort

the microphone arrays, as seen in Figure 3-9. The incident modes also propagate downstream of the acoustic driver array. To limit reflections from the open end downstream of the acoustic driver array a silencer was used as an anechoic termination.

Multiple test configurations were developed to allow a thorough investigation of the noise control mechanisms of the HQ tubes and evaluation of the VPI analytical model. A comprehensive review of the possible test configurations is presented in this section. The experimental setup allowed circumferential order disturbance modes to be generated with acoustic drivers and measured before and after control with the HQ tube system. First, the incident modes were measured using the hard wall case in which the HQ tubes were covered using aluminum tape. Then, separate tests were performed with the HQ tube system placed before and after the microphone arrays in order to measure transmitted, reflected, and scattered modes. These experimental configurations are shown in Figure 3-10.

With only one microphone array available for testing multiple test configurations were created to allow all the modes in the duct to be measured. With two microphone arrays it would have been possible to simultaneously measure both the reflected and transmitted modes in the duct. This would insure that the exact same incident mode was used to generate the transmitted and reflected modes in the duct. The incident modes were measured separately from the transmitted and reflected modes due to the inherent contamination that would have resulted from the reflected modes. Measuring the incident, transmitted, and reflected modes separately does not allow for an accurate energy balance to be performed on the system.

### Transmitted Modes Measurements



### Reflected Modes Measurements

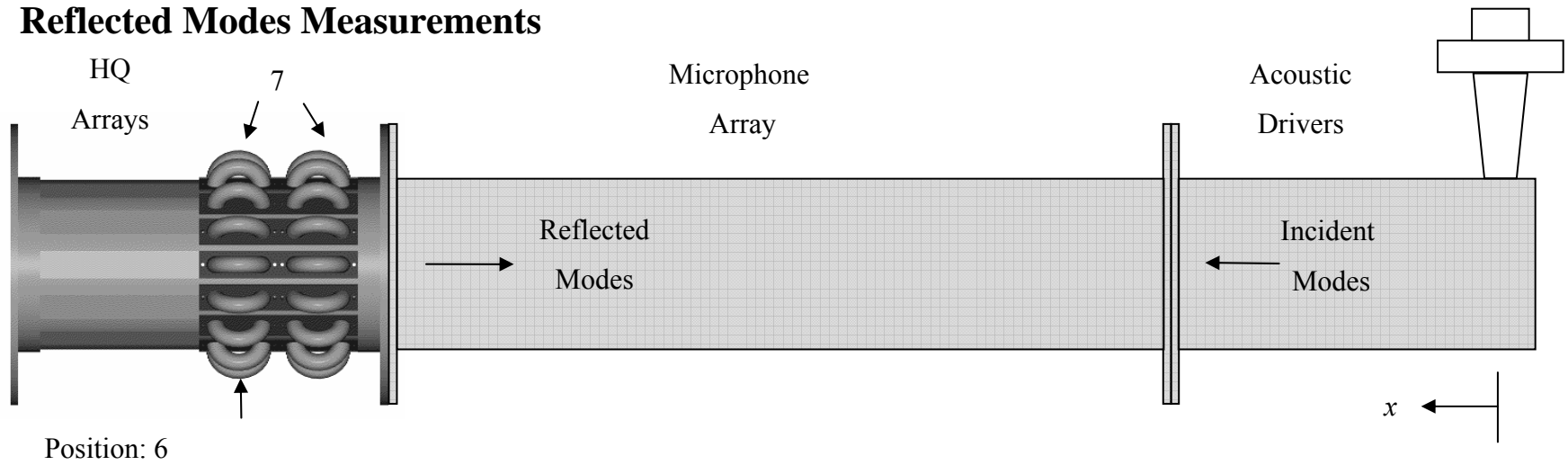


Figure 3-10: HQ tube system configurations to measure transmitted and reflected modes.

### Chapter 3. Experimental Effort

These configurations also allowed many HQ tube configurations to be examined. The axial positions, number of tubes, or number of arrays were varied for each test. The possible configurations for each HQ tube array position are shown in Table 3-4.

Position	HQ Tube Array Axial Position, $x$ (m)	Number of HQ Tubes, $N_{HQ}$	Number of HQ Tube Arrays	Modes Measured
1	0.683	8 or 16	1	Transmitted
2	0.816	8 or 16	1	Transmitted
3	0.949	8 or 16	1	Transmitted
4	1.080	8 or 16	1	Transmitted
5	0.683 & 0.816	8 or 16	2	Transmitted
6	2.035	8 or 16	1	Reflected
7	1.901 & 2.035	8 or 16	2	Reflected

Table 3-4: Possible HQ tube configurations.

The axial position of the HQ tube arrays are in reference to the center cross section of the acoustic driver array. Configurations with 8 HQ tubes were produced by covering up every other tube in the array with aluminum tape. Configurations with one array were achieved by covering up one HQ tube array with aluminum tape. HQ tube array axial positions 3 and 4 are achieved by rotating the HQ duct about its center cross-section.

## 3.2 HQ Tube System Modal Analysis

It is necessary to determine which modes will be present in the duct for each disturbance generated by the acoustic drivers. First, the cut-on frequencies of the modes in the duct must be determined to define their propagation characteristics at the frequency of interest. The modes scattered due to the HQ tubes can then be determined. Using the previous information, all the cut-on incident, transmitted, and reflected modes in the duct can be identified.

### 3.2.1 Duct Cut-Off Frequencies

The cut-off frequency of a mode is a function of the duct diameter (0.30 m) and defines the point in which the mode propagating characteristic turns from decaying to propagating. From equation (2.5) the cut-off frequency of the  $(m,n)$  mode is defined as

$$f_{mn, \text{cut-off}} = \frac{c}{2} k_{mn} \quad (3.3)$$

The resultant cut-off frequencies in Hz for each  $(m,n)$  mode are shown in Table 3-5.

		Radial Mode, $n$					
		0	1	2	3	4	5
Circumferential Mode, $m$	0	0	1418	2596	3764	4930	6094
	1	681	1973	3159	4331	5500	6666
	2	1130	2481	3689	4873	6049	7220
	3	1555	2966	4198	5397	6582	7760
	4	1968	3435	4693	5907	7103	8289
	5	2374	3893	5176	6406	7613	8808
	6	2776	4342	5650	6896	8115	9319
	7	3174	4785	6116	7379	8610	9822
	8	3570	5223	6577	7855	9098	10320
	9	3963	5656	7032	8326	9580	10811

Table 3-5: Duct cut-off frequencies in Hz.

The propagating modes below 2500 Hz are shown shaded in the table. A maximum frequency of 2500 Hz was chosen because the relative phase of the acoustic drivers became unsteady past this point.

### 3.2.2 HQ Tube Scattering Analysis

In order to determine all the modes propagating in the duct the scattered modes must also be found. Hallez [22] experimentally investigated circumferential scattering. He determined that for the case of an evenly spaced circumferential array of tubes, the circumferential scattering of modes due to the spatial aliasing of the HQ tubes is described as

$$m_{HQ} = m + kN_{HQ}, k = 0, \pm 1, \pm 2, \dots \quad (3.4)$$

where  $m$  is the circumferential order of the disturbance mode,  $N_{HQ}$  is the number of HQ tubes, and  $m_{HQ}$  is the m-order of the modes scattered by the array of tubes. For the experimental setup used in this work, a few of the scattered circumferential modes are shown in Table 3-6 for the both  $N_{HQ}=8$  and 16.

Disturbance $m$ -order	$m_{HQ}$					
	$N_{HQ} = 8$ Tubes			$N_{HQ} = 16$ Tubes		
	$k = -1$	$k = 0$	$k = 1$	$k = -1$	$k = 0$	$k = 1$
0	-8	0	8	-16	0	16
1	-7	1	9	-15	1	17
2	-6	2	10	-14	2	18
3	-5	3	11	-13	3	19
4	-4	4	12	-12	4	20
5	-3	5	13	-11	5	21
6	-2	6	14	-10	6	22
7	-1	7	15	-9	7	23
8	0	8	16	-8	8	24
9	1	9	17	-7	9	25

Table 3-6: Circumferential modes scattered due to HQ tubes.

As an example, for  $N_{HQ}=8$  tubes and a disturbance circumferential order  $m=1$ , there is circumferential scattering into the  $m=-7$  and  $m=9$  modes.

### 3.2.3 Incident and Transmitted Cut-On Modes

The results from Table 3-5 and Table 3-6 can be used to determine the incident and transmitted cut-on modes in the duct for each disturbance  $m$ -order for both 8 and 16 HQ tubes. The cut-on modes in the duct at 2500 Hz are shown in Table 3-7.

		Transmitted and Reflected Modes	
Disturbance $m$ -order	Incident Modes	$N_{HQ} = 8$ Tubes	$N_{HQ} = 16$ Tubes
$m = 0$	(0,0) (1,1)	(0,0) (0,1) R.S.	(0,0) (0,1) R.S.
$m = 1$	(1,0) (1,1)	(1,0) (1,1) R.S.	(1,0) (1,1) R.S.
$m = 2$	(2,0) (2,1)	(2,0) (2,1) R.S.	(2,0) (2,1) R.S.
$m = 3$	(3,0)	(3,0)	(3,0)
$m = 4$	(4,0)	(-4,0) (4,0) C.S.	(4,0)

Table 3-7: Incident and transmitted cut-on modes at  $f=2500$  Hz.

In this table, the radial and circumferential scattering effects are noted as R.S. and C.S., respectively. For example, with a disturbance circumferential order  $m=4$  the (4,0) mode is the only incident mode. This is because the (4,0) mode has a cut-off frequency of 1968 Hz (see Table 3-5) and thus propagates while the (4,1) mode is cut-on at 3435 Hz, > 2500 Hz, and thus it is cut-off. The transmitted modes are then determined. From Table 3-6, it is shown that for  $N_{HQ}=8$ , there is circumferential scattering into the  $m=-4$  and  $m=12$ , of which the (-4,0) is the only mode with a cut-off frequency below 2500 Hz. Thus, both the (4,0) and (-4,0) will be present in the transmitted and reflected sound fields.

## 3.3 Data Analysis and Post Processing

The microphone pressure measurements were collected with a data acquisition system for each experiment. The pressure measurements were used to compute auto and cross spectrums. These auto and cross spectrums were used to analyze the microphone data collected and compute modal amplitudes using the modal decomposition technique

developed in this section. The modal amplitude results allowed the pressure measurements on the duct wall to be viewed on a modal level. The results also allowed direct comparison between the experimental and analytical data.

### 3.3.1 Data Collection and Reduction

For each experiment a DataMax acquisition system was used to simultaneously record the 20 microphone channels. The data acquisition system recorded 10 seconds of time data, with a sampling rate of 20000 Hz. An anti-aliasing filter was paced at 8000 Hz.

Using 50% overlapping, the time data was broken up into 47 data blocks. A Hanning window was applied to each data block and a Fast Fourier Transform (FFT) was performed with 8192 spectral lines, frequency resolution of 2.44 Hz.. For each data block, the auto and cross spectrum were calculated from the FFT results to form the spectral matrix. The spectral matrices of the 47 data blocks were then averaged.

### 3.3.2 Modal Decomposition Technique

It is necessary to determine the modal amplitudes of the modes propagation upstream and downstream in the duct. A modal decomposition technique is developed to obtain the modal amplitudes of the modes in the duct from pressure measurements on the duct wall. The modes in the circular duct could be spinning in the positive or negative azimuthal direction as well as traveling in both the positive or negative  $z$ -direction. For the sake of clarity, the following notation will be used for the analysis

$$\left( \right)_{mn}^{(st)}$$

where the term in the parenthesis could be any variable including matrices. The indices  $m$  and  $n$  indicate that the variable in parenthesis is associated to the  $(m,n)$  mode. The parameter  $s$  may be + or – indicating that the variable is related to a positive or negative spinning mode, respectively. Similarly the parameter  $t$  may be + or – indicating the variable is related to a positive or negative traveling mode, respectively.

The pressure field in the duct is described as a summation of all possible acoustic modes in the duct. Equation (2.21) describes the pressure field in the duct and can be

### Chapter 3. Experimental Effort

used to determine the pressure at the  $\ell^{th}$  microphone, located at position  $(a, \theta_\ell, z_\ell)$ , that is

$$\begin{aligned}
 p_\ell(a, \theta_\ell, z_\ell) = & \sum_{m=0}^{N_\theta} \sum_{n=0}^{N_r} A_{mn}^{(++)} J_m(k_{mn}a) e^{-im\theta_\ell} e^{-ik_{mn}z_\ell} + \sum_{m=0}^{N_\theta} \sum_{n=0}^{N_r} A_{mn}^{(-+)} J_m(k_{mn}a) e^{im\theta_\ell} e^{-ik_{mn}z_\ell} \\
 & + \sum_{m=0}^{N_\theta} \sum_{n=0}^{N_r} A_{mn}^{(+-)} J_m(k_{mn}a) e^{-im\theta_\ell} e^{ik_{mn}z_\ell} + \sum_{m=0}^{N_\theta} \sum_{n=0}^{N_r} A_{mn}^{(--)} J_m(k_{mn}a) e^{im\theta_\ell} e^{ik_{mn}z_\ell}
 \end{aligned} \tag{3.5}$$

It is convenient to rewrite equation (3.5) for all microphones in matrix form as

$$\begin{aligned}
 \{p\} = & \left[ T^{(++)} \right] \{F_{mn}^{(++)}\} + \left[ T^{(-+)} \right] \{F_{mn}^{(-+)}\} + \left[ T^{(+-)} \right] \{F_{mn}^{(+-)}\} + \left[ T^{(--)} \right] \{F_{mn}^{(--)}\} \\
 (N_M \times 1) \quad & (N_M \times N_A)(N_A \times 1) \quad (N_M \times N_A)(N_A \times 1) \quad (N_M \times N_A)(N_A \times 1) \quad (N_M \times N_A)(N_A \times 1)
 \end{aligned} \tag{3.6}$$

where  $N_M$  is the total number of microphones in the logarithmically spaced circumferential and helical arrays located on the duct wall. Only modes that are cut-on are included in this approach. Thus, the total number of propagating modes present in the duct is,  $N_A = N_\theta + N_r$ . The elements of vector  $\{p\}$  are the pressure at each microphone ( $\ell = 1, \dots, N_M$ ), that is

$$\{p\}^T = \{p_1, \dots, p_\ell, \dots, p_{N_M}\} \tag{3.7}$$

The  $\left[ T^{(st)} \right]$  matrices in equation (3.6) describe the modal pressure variation in the azimuth and axial direction for each mode at each microphone location. These matrices can be written as

### Chapter 3. Experimental Effort

$$\begin{aligned} [T^{(++)}] = & \left[ \left\{ B_{00}^{(++)} \right\}, \dots, \left\{ B_{0n}^{(++)} \right\}, \dots, \left\{ B_{0N_r}^{(++)} \right\}, \dots, \left\{ B_{m0}^{(++)} \right\}, \dots, \left\{ B_{mn}^{(++)} \right\}, \dots, \left\{ B_{mN_r}^{(++)} \right\}, \dots, \right. \\ & \left. \left\{ B_{N_\theta 0}^{(++)} \right\}, \dots, \left\{ B_{N_\theta n}^{(++)} \right\}, \dots, \left\{ B_{N_\theta N_r}^{(++)} \right\} \right], \end{aligned}$$

$$\begin{aligned} [T^{(+)}] = & \left[ \left\{ B_{00}^{(+)} \right\}, \dots, \left\{ B_{0n}^{(+)} \right\}, \dots, \left\{ B_{0N_r}^{(+)} \right\}, \dots, \left\{ B_{m0}^{(+)} \right\}, \dots, \left\{ B_{mn}^{(+)} \right\}, \dots, \left\{ B_{mN_r}^{(+)} \right\}, \dots, \right. \\ & \left. \left\{ B_{N_\theta 0}^{(+)} \right\}, \dots, \left\{ B_{N_\theta n}^{(+)} \right\}, \dots, \left\{ B_{N_\theta N_r}^{(+)} \right\} \right], \end{aligned}$$

$$\begin{aligned} [T^{(-)}] = & \left[ \left\{ B_{00}^{(-)} \right\}, \dots, \left\{ B_{0n}^{(-)} \right\}, \dots, \left\{ B_{0N_r}^{(-)} \right\}, \dots, \left\{ B_{m0}^{(-)} \right\}, \dots, \left\{ B_{mn}^{(-)} \right\}, \dots, \left\{ B_{mN_r}^{(-)} \right\}, \dots, \right. \\ & \left. \left\{ B_{N_\theta 0}^{(-)} \right\}, \dots, \left\{ B_{N_\theta n}^{(-)} \right\}, \dots, \left\{ B_{N_\theta N_r}^{(-)} \right\} \right], \end{aligned}$$

and

$$\begin{aligned} [T^{(-)}] = & \left[ \left\{ B_{00}^{(-)} \right\}, \dots, \left\{ B_{0n}^{(-)} \right\}, \dots, \left\{ B_{0N_r}^{(-)} \right\}, \dots, \left\{ B_{m0}^{(-)} \right\}, \dots, \left\{ B_{mn}^{(-)} \right\}, \dots, \left\{ B_{mN_r}^{(-)} \right\}, \dots, \right. \\ & \left. \left\{ B_{N_\theta 0}^{(-)} \right\}, \dots, \left\{ B_{N_\theta n}^{(-)} \right\}, \dots, \left\{ B_{N_\theta N_r}^{(-)} \right\} \right] \end{aligned} \quad (3.8)$$

where the columns of these matrices describe the modal pressure variation in the azimuth and axial direction for a particular  $(m,n)$  mode. The  $\{B_{mn}^{(st)}\}$  vectors are described as

$$\left\{ B_{mn}^{(++)} \right\}^T = \left\{ e^{-im\theta_1} e^{-ik_{mn,z}z_1}, \dots, e^{-im\theta_\ell} e^{-ik_{mn,z}z_\ell}, \dots, e^{-im\theta_{N_\ell}} e^{-ik_{mn,z}z_{N_\ell}} \right\},$$

$$\left\{ B_{mn}^{(+)} \right\}^T = \left\{ e^{im\theta_1} e^{-ik_{mn,z}z_1}, \dots, e^{im\theta_\ell} e^{-ik_{mn,z}z_\ell}, \dots, e^{im\theta_{N_\ell}} e^{-ik_{mn,z}z_{N_\ell}} \right\},$$

$$\left\{ B_{mn}^{(-)} \right\}^T = \left\{ e^{-im\theta_1} e^{ik_{mn,z}z_1}, \dots, e^{-im\theta_\ell} e^{ik_{mn,z}z_\ell}, \dots, e^{-im\theta_{N_\ell}} e^{ik_{mn,z}z_{N_\ell}} \right\},$$

and

$$\left\{ B_{mn}^{(-)} \right\}^T = \left\{ e^{im\theta_1} e^{ik_{mn,z}z_1}, \dots, e^{im\theta_\ell} e^{ik_{mn,z}z_\ell}, \dots, e^{im\theta_{N_\ell}} e^{ik_{mn,z}z_{N_\ell}} \right\} \quad (3.9)$$

### Chapter 3. Experimental Effort

The elements of the vectors  $\{F_{mn}^{(st)}\}$  in equation (3.6) represent the modal amplitudes  $A_{mn}^{(st)}$  weighted by the Bessel function  $J_m$  evaluated at the duct wall for each mode. That is

$$\{F_{mn}^{(++)}\}^T = \{F_{00}^{(++)}, \dots, F_{0n}^{(++)}, \dots, F_{0N_r}^{(++)}, \dots, F_{m0}^{(++)}, \dots, F_{mn}^{(++)}, \dots, F_{mN_r}^{(++)}, \dots, F_{N_\theta 0}^{(++)}, \dots, F_{N_\theta n}^{(++)}, \dots, F_{N_\theta N_r}^{(++)}\},$$

$$\{F_{mn}^{(+-)}\}^T = \{F_{00}^{(+-)}, \dots, F_{0n}^{(+-)}, \dots, F_{0N_r}^{(+-)}, \dots, F_{m0}^{(+-)}, \dots, F_{mn}^{(+-)}, \dots, F_{mN_r}^{(+-)}, \dots, F_{N_\theta 0}^{(+-)}, \dots, F_{N_\theta n}^{(+-)}, \dots, F_{N_\theta N_r}^{(+-)}\},$$

$$\{F_{mn}^{(+)}\}^T = \{F_{00}^{(+)}, \dots, F_{0n}^{(+)}, \dots, F_{0N_r}^{(+)}, \dots, F_{m0}^{(+)}, \dots, F_{mn}^{(+)}, \dots, F_{mN_r}^{(+)}, \dots, F_{N_\theta 0}^{(+)}, \dots, F_{N_\theta n}^{(+)}, \dots, F_{N_\theta N_r}^{(+)}\},$$

and

$$\{F_{mn}^{(-)}\}^T = \{F_{00}^{(-)}, \dots, F_{0n}^{(-)}, \dots, F_{0N_r}^{(-)}, \dots, F_{m0}^{(-)}, \dots, F_{mn}^{(-)}, \dots, F_{mN_r}^{(-)}, \dots, F_{N_\theta 0}^{(-)}, \dots, F_{N_\theta n}^{(-)}, \dots, F_{N_\theta N_r}^{(-)}\} \quad (3.10)$$

where

$$F_{mn}^{(++)} = A_{mn}^{(++)} J_m(k_{mn}a),$$

$$F_{mn}^{(+-)} = A_{mn}^{(+-)} J_m(k_{mn}a),$$

$$F_{mn}^{(+)} = A_{mn}^{(+)} J_m(k_{mn}a),$$

and

$$F_{mn}^{(-)} = A_{mn}^{(-)} J_m(k_{mn}a) \quad (3.11)$$

To find the modal amplitude  $A_{mn}^{(st)}$ , of a mode spinning and traveling in a particular direction, equation (3.6) is pre-multiplied by the corresponding vector  $\{B_{\alpha\beta}^{(st)}\}^H$  in equation (3.9). Where the superscript  $H$  indicates Hermitian, i.e. the complex transpose. For example, to solve for the modal amplitude  $A_{\alpha\beta}^{(++)}$ , i.e. amplitude of the positive

spinning and traveling  $(\alpha, \beta)$  mode equation (3.6) is pre-multiplied by the vector  $\{B_{\alpha\beta}^{(++)}\}$ .

That is,

$$\begin{aligned} \{B_{\alpha\beta}^{(++)}\}^H \{p\} = & \{B_{\alpha\beta}^{(++)}\}^H [T^{(++)}] \{F_{mn}^{(++)}\} + \{B_{\alpha\beta}^{(++)}\}^H [T^{(+-)}] \{F_{mn}^{(+-)}\} + \\ & \{B_{\alpha\beta}^{(++)}\}^H [T^{(-+)}] \{F_{mn}^{(-+)}\} + \{B_{\alpha\beta}^{(++)}\}^H [T^{(--)}] \{F_{mn}^{(--)}\} \end{aligned} \quad (3.12)$$

It can be seen in equation (3.12) that the vector  $\{B_{\alpha\beta}^{(++)}\}^H$  will pre-multiply all the vectors in equation (3.9). If a large number of microphones are used, all vector products will vanish except for  $\{B_{\alpha\beta}^{(++)}\}^H \{B_{\alpha\beta}^{(++)}\} = N_M$ . This is because the hard wall duct modes are orthogonal in both azimuthal and axial directions. However, if the positions of a small number of microphones are selected properly, the direct vector product of  $\{B_{\alpha\beta}^{(++)}\}^H \{B_{\alpha\beta}^{(++)}\}$  will be dominant overall all other terms. The validity off this assumption approximation will be presented in section 3.3.3. Assuming this orthogonality condition equation (3.12) is simplified to

$$\{B_{\alpha\beta}^{(++)}\}^H \{p\} = \{B_{\alpha\beta}^{(++)}\}^H \{B_{\alpha\beta}^{(++)}\} F_{\alpha\beta}^{(++)} \quad (3.13)$$

Post-multiplying each side of this equation by its Hermitian yields

$$\{B_{\alpha\beta}^{(++)}\}^H \{p\} \{p\}^H \{B_{\alpha\beta}^{(++)}\} = \{B_{\alpha\beta}^{(++)}\}^H \{B_{\alpha\beta}^{(++)}\} |F_{\alpha\beta}^{(++)}|^2 \{B_{\alpha\beta}^{(++)}\}^H \{B_{\alpha\beta}^{(++)}\} \quad (3.14)$$

Equations (3.12) through (3.14) can similarly be used to solve for the modal amplitudes of the other directions of propagation. Through some straightforward manipulation the amplitude of the  $(\alpha, \beta)$  mode in all four directions can be solved as

### Chapter 3. Experimental Effort

$$|A_{\alpha\beta}^{(++)}|^2 = \left( \{B_{\alpha\beta}^{(++)}\}^H \{p\} \{p\}^H \{B_{\alpha\beta}^{(++)}\} \right) / \left( |J_{\alpha}(k_{\alpha\beta}a)|^2 \left( \{B_{\alpha\beta}^{(++)}\}^H \{B_{\alpha\beta}^{(++)}\} \right)^2 \right),$$

$$|A_{\alpha\beta}^{(-+)}|^2 = \left( \{B_{\alpha\beta}^{(-+)}\}^H \{p\} \{p\}^H \{B_{\alpha\beta}^{(-+)}\} \right) / \left( |J_{\alpha}(k_{\alpha\beta}a)|^2 \left( \{B_{\alpha\beta}^{(-+)}\}^H \{B_{\alpha\beta}^{(-+)}\} \right)^2 \right),$$

$$|A_{\alpha\beta}^{(+-)}|^2 = \left( \{B_{\alpha\beta}^{(+-)}\}^H \{p\} \{p\}^H \{B_{\alpha\beta}^{(+-)}\} \right) / \left( |J_{\alpha}(k_{\alpha\beta}a)|^2 \left( \{B_{\alpha\beta}^{(+-)}\}^H \{B_{\alpha\beta}^{(+-)}\} \right)^2 \right),$$

and

$$|A_{\alpha\beta}^{(--)}|^2 = \left( \{B_{\alpha\beta}^{(--)}\}^H \{p\} \{p\}^H \{B_{\alpha\beta}^{(--)}\} \right) / \left( |J_{\alpha}(k_{\alpha\beta}a)|^2 \left( \{B_{\alpha\beta}^{(--)}\}^H \{B_{\alpha\beta}^{(--)}\} \right)^2 \right) \quad (3.15)$$

The modal power of the  $(\alpha, \beta)$  mode can now be solved for using equation (2.26) as

$$W_{\alpha\beta}^{(++)} = \frac{\pi a^2 \Lambda_{\alpha\beta}}{\rho c} |A_{\alpha\beta}^{(++)}|^2 \left( \frac{k_{\alpha\beta,z}}{k_o} \right),$$

$$W_{\alpha\beta}^{(-+)} = \frac{\pi a^2 \Lambda_{\alpha\beta}}{\rho c} |A_{\alpha\beta}^{(-+)}|^2 \left( \frac{k_{\alpha\beta,z}}{k_o} \right),$$

$$W_{\alpha\beta}^{(+-)} = \frac{\pi a^2 \Lambda_{\alpha\beta}}{\rho c} |A_{\alpha\beta}^{(+-)}|^2 \left( \frac{k_{\alpha\beta,z}}{k_o} \right),$$

and

$$W_{\alpha\beta}^{(--)} = \frac{\pi a^2 \Lambda_{\alpha\beta}}{\rho c} |A_{\alpha\beta}^{(--)}|^2 \left( \frac{k_{\alpha\beta,z}}{k_o} \right) \quad (3.16)$$

The magnitude of the modal amplitude and power of each mode propagating in the duct can now be determined. Using microphone pressure measurements the relative phase of the modal amplitudes between the  $(\alpha, \beta)$  and  $(m, n)$  modes may also be determined. Post-multiplying each side of equation (3.13) by the Hermitian of itself for mode  $(m, n)$  yields

$$\{B_{\alpha\beta}^{(++)}\}^H \{p\}\{p\}^H \{B_{mn}^{(++)}\} = \{B_{\alpha\beta}^{(++)}\}^H \{B_{\alpha\beta}^{(++)}\} F_{\alpha\beta}^{(++)} F_{mn}^{(++)H} \{B_{mn}^{(++)}\}^H \{B_{mn}^{(++)}\} \quad (3.17)$$

Through some straight forward manipulation the product of the modal amplitudes of the  $(\alpha,\beta)$  and  $(m,n)$  modes can be solved as

$$A_{\alpha\beta}^{(++)} A_{mn}^{(++)H} = \frac{\{B_{\alpha\beta}^{(++)}\}^H \{p\}\{p\}^H \{B_{mn}^{(++)}\}}{J_{\alpha}(k_{\alpha\beta}a) J_m(k_{mn}a) \{B_{\alpha\beta}^{(++)}\}^H \{B_{\alpha\beta}^{(++)}\} \{B_{mn}^{(++)}\}^H \{B_{mn}^{(++)}\}} \quad (3.18)$$

Therefore, the relative phase of the modal amplitudes of the  $(\alpha,\beta)$  and  $(m,n)$  modes is

$$\phi_{rel} = \tan^{-1} \frac{\text{Im ag} \left[ A_{\alpha\beta}^{(++)} A_{mn}^{(++)H} \right]}{\text{Re al} \left[ A_{\alpha\beta}^{(++)} A_{mn}^{(++)H} \right]} \quad (3.19)$$

### 3.3.3 Orthogonality Assumption

The previous modal decomposition approach assumes that  $\{B_{\alpha\beta}^{(st)}\}^H \{B_{mn}^{(st)}\}$  for  $\alpha=m$  and  $\beta=n$  dominates over the other terms, i.e.  $\alpha \neq m$  and  $\beta \neq n$ . Here, this orthogonality assumption is evaluated for the experimental setup described in section 3.1. To examine this assumption the product of the positive spinning and traveling  $(\alpha,\beta)=(1,0)$  mode, times each of the  $(m,n)$  modes propagating in the duct is compared in Figure 3-11 through Figure 3-14. For example, in Figure 3-11 the red line represents the product  $\{B_{10}^{(++)}\}^H \{B_{10}^{(++)}\} = 20$  because there are 20 microphones. The blue line represents the product  $\{B_{10}^{(++)}\}^H \{B_{00}^{(++)}\}$ . Each line starts at the cut-off frequency of the mode, which is the point in which the mode turns from decaying to propagating. For easy comparison, the dashed line in Figure 3-12 through Figure 3-14 represents the product of  $\{B_{10}^{(++)}\}^H \{B_{10}^{(++)}\}$ . As seen from Figure 3-11 through Figure 3-14, as expected, the cross products are always smaller than 20. However, the direct product is not always much larger than the cross terms.

### Chapter 3. Experimental Effort

Improvements can be made in the orthogonality condition of the modal decomposition technique. Increasing the number of microphones in the array and/or optimizing the position of the microphones would increase the difference between the magnitude of mode of interest and the other modes in the duct. However, the microphone locations could not be changed for these experiments.

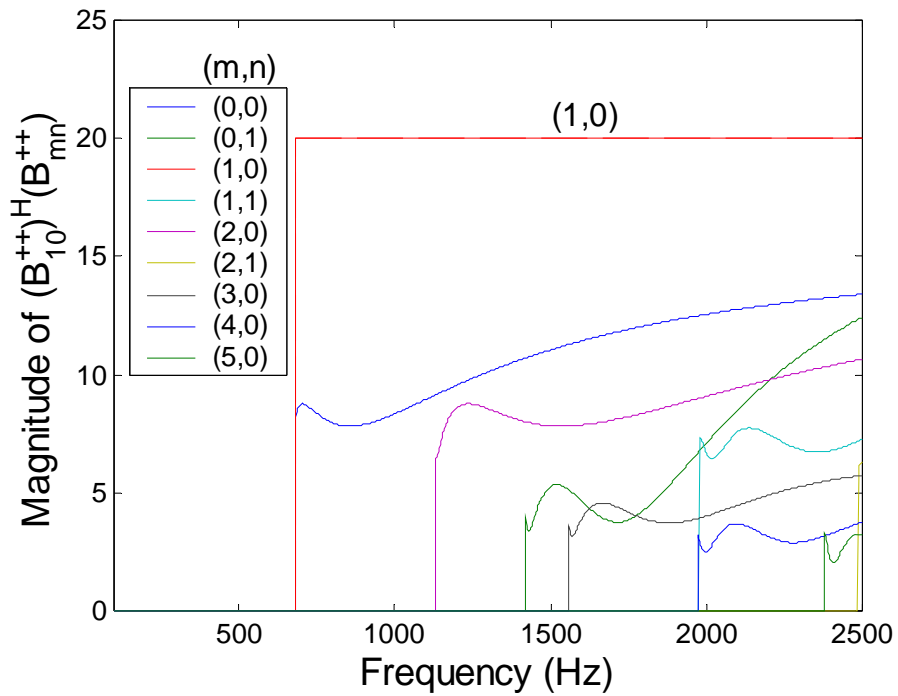


Figure 3-11: Comparison of the product of the positive spinning and traveling (1,0) mode versus each positive spinning and traveling mode in the duct.

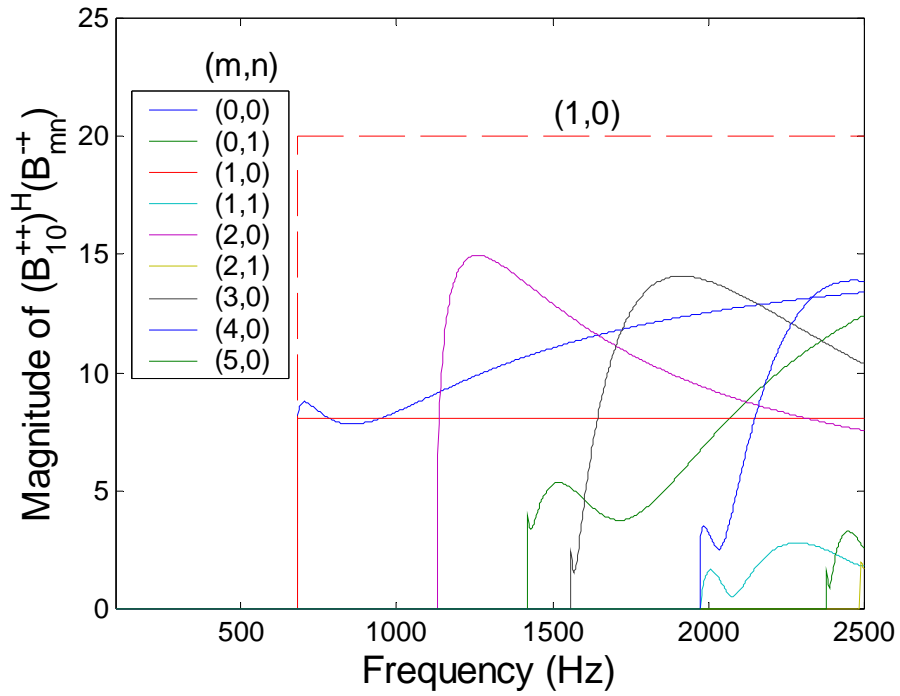


Figure 3-12: Comparison of the product of the positive spinning and traveling (1,0) mode versus each negative spinning and positive traveling mode in the duct.

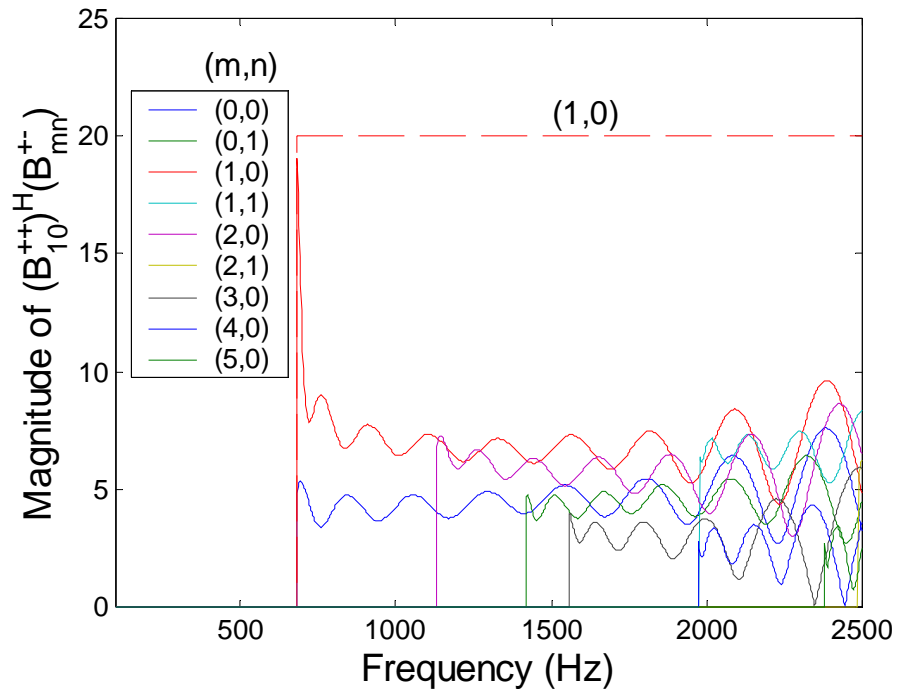


Figure 3-13: Comparison of the product of the positive spinning and traveling (1,0) mode versus each positive spinning and negative traveling mode in the duct.

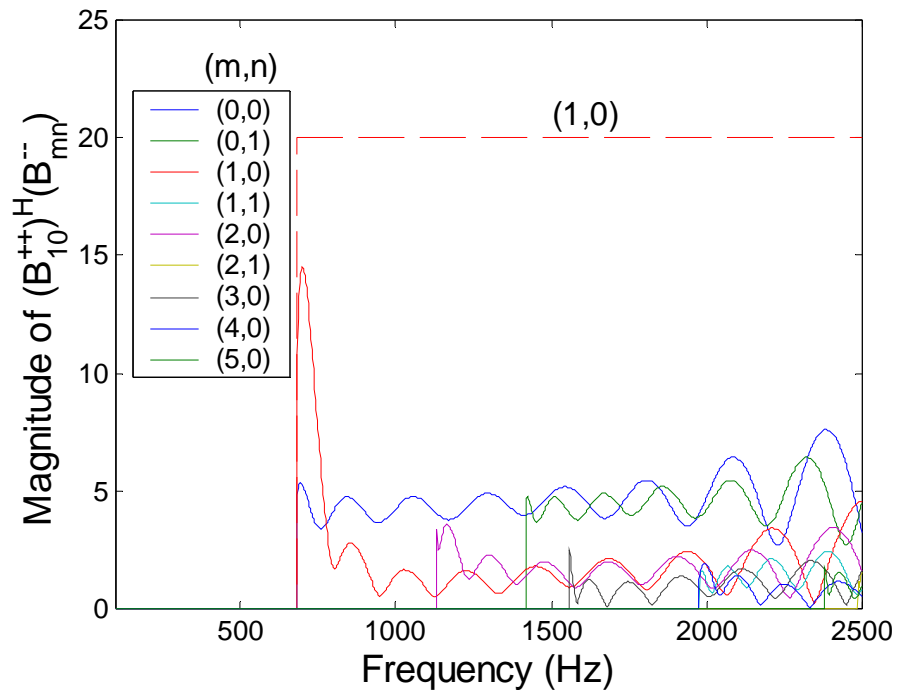


Figure 3-14: Comparison of the product of the positive spinning and traveling (1,0) mode versus each negative spinning and traveling mode in the duct.

## **Chapter 4. Experimental Results**

This chapter will focus on presenting and discussing the results of this study. Results of a microphone signal analysis examining auto spectrums, coherence, and cross spectrum will be explored. Results of the modal decomposition are presented. Theoretical and experimental modal power comparisons are presented and investigated in detail for five cases. For each case, objectives of the test, description of the setup, and discussion of the results will be studied. These experiments were designed to fundamentally study the noise control mechanisms of the HQ tubes and allow evaluation of the VPI analytical model.

### **4.1 Microphone Signal Analysis**

To determine how well the acoustic drivers generated the acoustic modes they were intended too, a microphone signal analysis was performed. The plots shown in this section are all of hard wall cases to investigate the system unobstructed by the HQ tubes. Auto spectrums were generated for each microphone for each case. The levels of the background noise in contrast to the experimental levels are examined. The coherence between two microphones and a theoretical and experimental cut-off frequency comparison is obtained. Cross spectrums between microphones are then calculated to investigate the accuracy of the formulation of the incident modes generated for the acoustic drivers.

### 4.1.1 Auto Spectrums

In each case, the auto spectrum for each microphone was generated. Figure 4-1 shows an example of an auto spectrum of the sound pressure level of microphone 5 for the hard wall cases in which the (2,0) incident mode was generated.

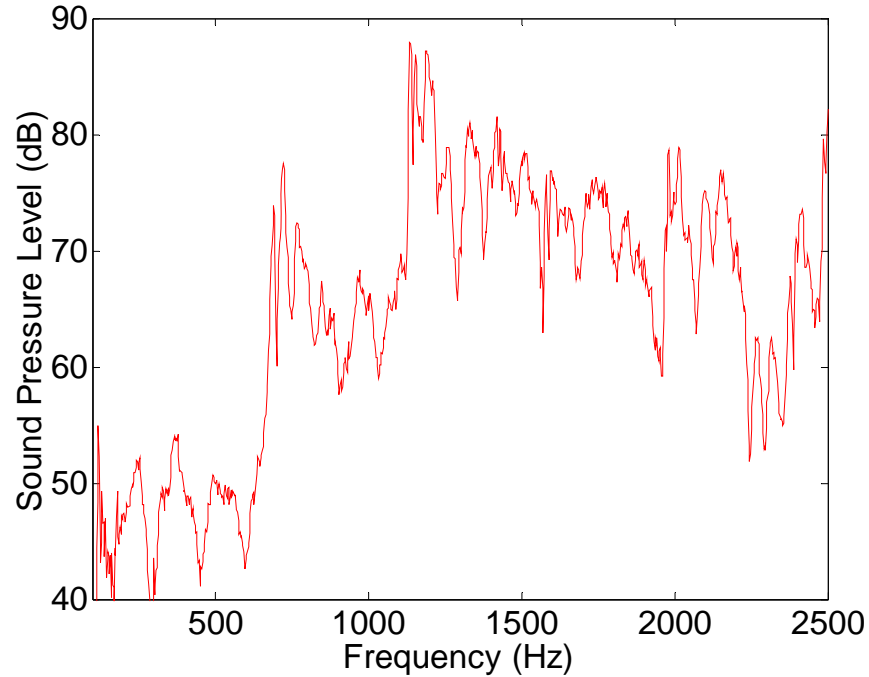


Figure 4-1: Auto Spectrum of microphone 5 for the hard wall cases with the (2,0) incident mode.

The auto spectrum shows its largest levels around 1150 Hz, which corresponds to the cut-off frequency of the (2,0) mode. At the cut-off frequency of a mode its modal amplitude is theoretically infinite which creates large sound pressure levels. The acoustic drivers were set to generate the (2,0) mode, thus, these increased levels are expected. However, the spike around 677 Hz, which corresponds to the cut-off frequency of the (1,0) mode was not intended to be generated by the acoustic drivers. The accuracy of the mode formulation of the acoustic drivers will be further investigated in below section 4.1.3.

The background noise was measured to ensure the sound pressure levels measured during experiments were much louder than the noise floor. A comparison of the hard wall case in which the (2,0) mode was incident and the background noise of microphone 5, are shown in Figure 4-2.

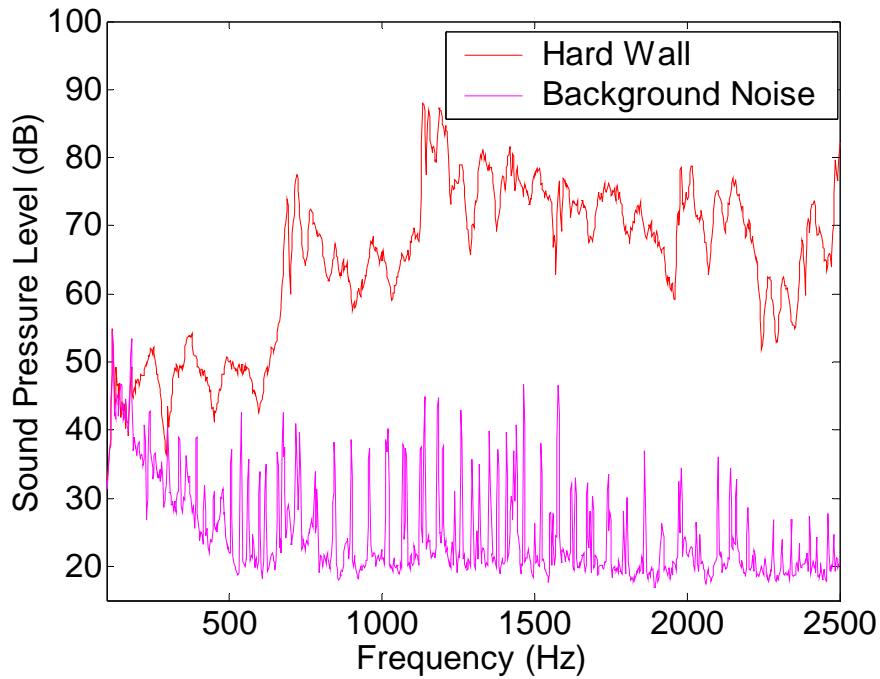


Figure 4-2: Auto Spectrums of microphone 5 comparing the hard wall case with the (2,0) incident mode and the background noise.

The average sound pressure level of the (2,0) incident mode is about 70 dB, while the background noise lies below 45 dB. The background noise is shown to be at acceptable levels in comparison to the experimental levels.

#### 4.1.2 Coherence and Cut-off Frequency

The coherence between microphones was also calculated. A typical coherence plot between microphones 1 and 2 for the hard wall case in which the (2,0) incident mode was generated is shown in Figure 4-3.

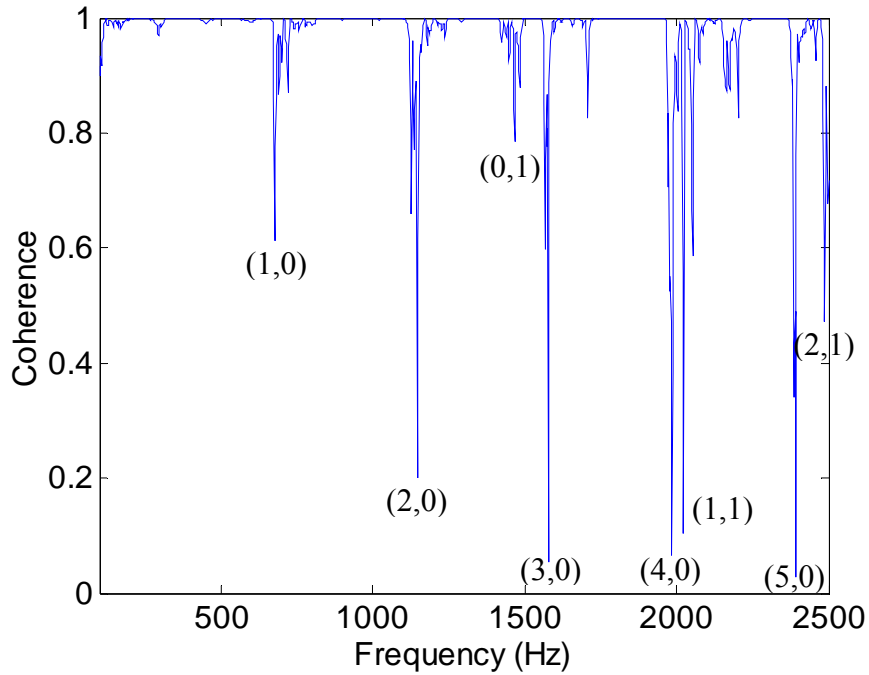


Figure 4-3: Coherence between microphones 1 and 2 for hard wall case with the (2,0) incident mode.

Frequencies with low coherence correspond to the cut-off frequencies of the cut-on modes in the duct. These frequencies are used to experimentally determine the cut-off frequencies. A comparison of the analytic cut-off frequencies from section 3.2.1 and the experimentally determined cut-off frequencies from the Figure 4-3 are shown in Table 4-1.

Mode ( $m,n$ )	Cut-off Frequency $f_{mn, cut-off}$ (Hz)		
	Analytical	Experimental	% Difference
(0,0)	0	0	0.00
(1,0)	681	677	-0.59
(2,0)	1130	1146	1.40
(0,1)	1418	1466	3.27
(3,0)	1555	1579	1.52
(1,1)	1968	1984	0.81
(4,0)	1973	2023	2.47
(5,0)	2374	2393	0.79
(2,1)	2481	2488	0.28

Table 4-1: Analytical versus experimental cut-off frequency comparison.

The results show very good agreement between the analytical and experimental cut-off frequencies.

### 4.1.3 Cross Spectrum

To investigate the accuracy of the incident mode formulation of the acoustic drivers the cross spectrum between microphones was calculated. For example, a hard wall case was examined in which the  $m$ -order 1 modes were generated. In Figure 4-4 the relative phase of microphones 1 through 7 is shown with respect to the reference microphone 1. These microphones are logarithmically spaced around the circumference of a cross-section in the duct. With only the plane wave, (0,0) mode cut-on until 681 Hz, the relative phase between microphones is equal, as expected. At 681 Hz, the (1,0) mode cuts-on and goes through a circumferential pressure variation of  $2\pi$ . The cross-section of a circular duct is also  $2\pi$  around. Thus, for the (1,0) mode the relative phase of the each microphone should match its respective angular position. Zooming in on Figure 4-4 the relative phase of each microphone is compared to its angular position in Figure 4-5. The angular position of each microphone is shown in the same color as its respective microphone phase. The trend is correct but the relative phase varies over frequency.

## Chapter 4. Experimental Results

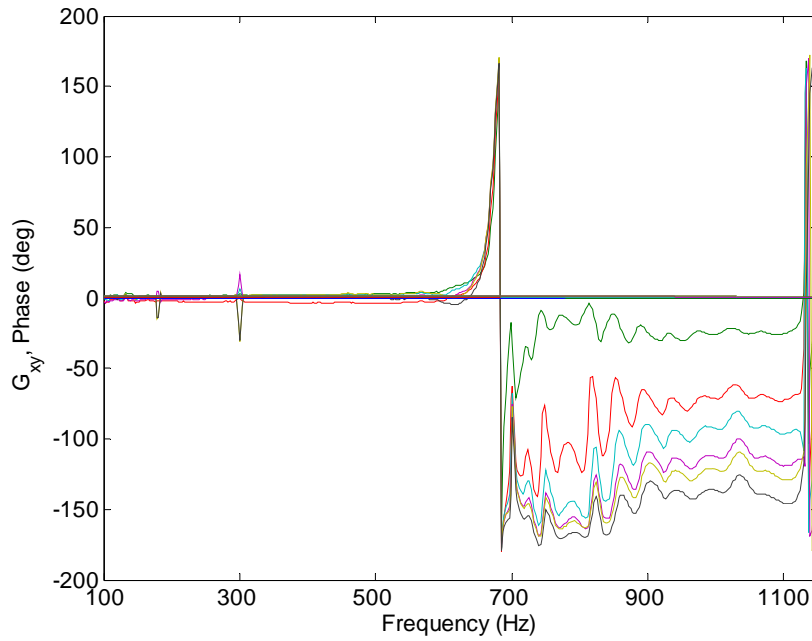


Figure 4-4: Relative phase of microphones 1 through 7 with respect to microphone 1.

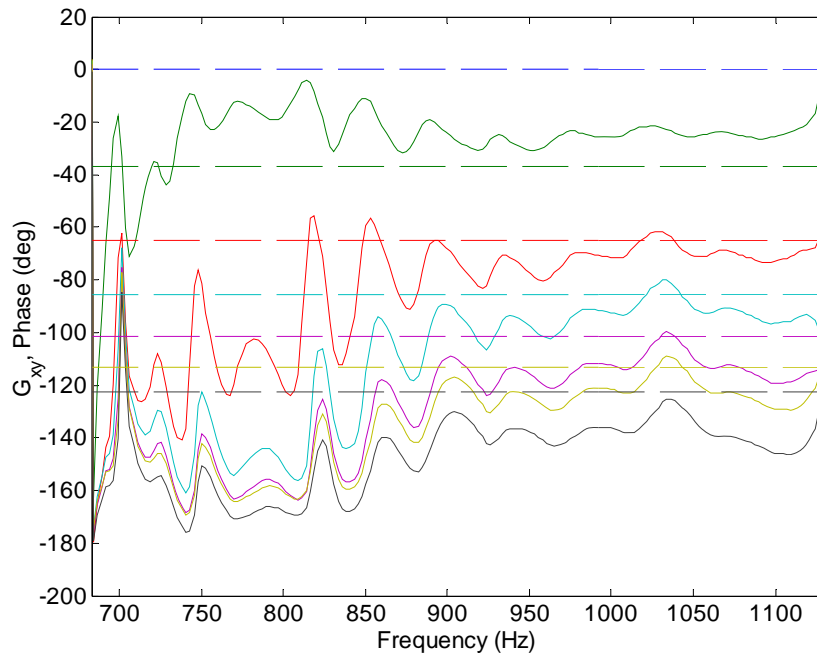


Figure 4-5: Comparison of the relative phase of microphones 1 through 7 with respect to microphone 1 and their respective angular positions.

This phase variation over frequency suggests improvements could be made in the formulation of the disturbance modes generated by the acoustic drivers. The accuracy of the disturbance mode generation and the acoustic measurements could be increased by using phased matched acoustic drivers and microphones, respectively.

## 4.2 Modal Decomposition Results

An example modal decomposition was performed for the hard wall case in which positive spinning and traveling  $m$ -order 1 modes were generated. Figure 4-6 through Figure 4-12 show the resultant sound power for each mode in the duct. Each plot shows four curves corresponding to the four  $(m,n)$  modes: positive spinning and traveling, negative spinning and positive traveling, positive spinning and negative traveling, and negative spinning and traveling. It is expected that the sound power level of the positive spinning and traveling (1,0) and (1,1) modes should dominate over all other modes in the duct. Figure 4-8 and Figure 4-9 show the positive spinning and traveling (1,0) and (1,1) modes do dominate over the other propagating (1,0) and (1,1) modes. However, Figure 4-6 and Figure 4-7 show that they do not dominate over all of the modes in the duct. This is especially true at the cut-off frequencies of other modes.

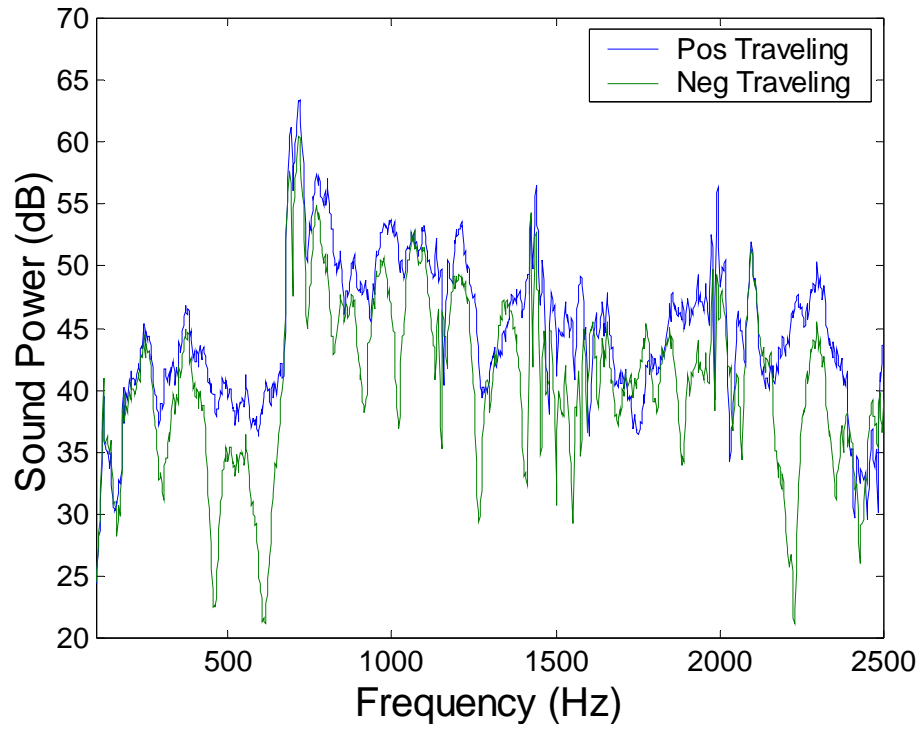


Figure 4-6: Sound power versus frequency for the (0,0) mode.

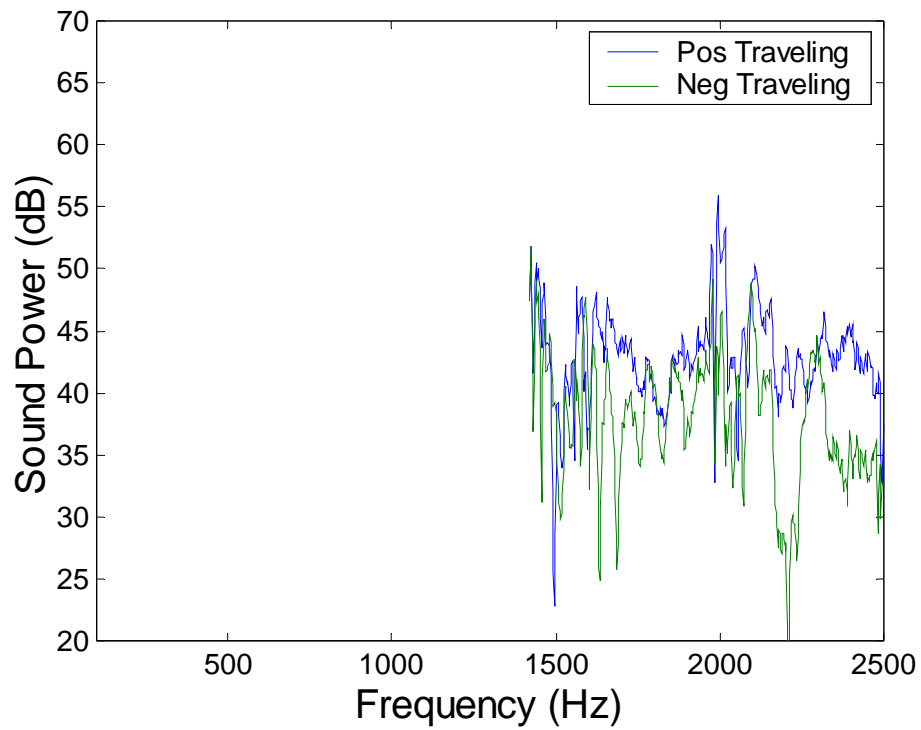


Figure 4-7: Sound power versus frequency of the (0,1) mode.

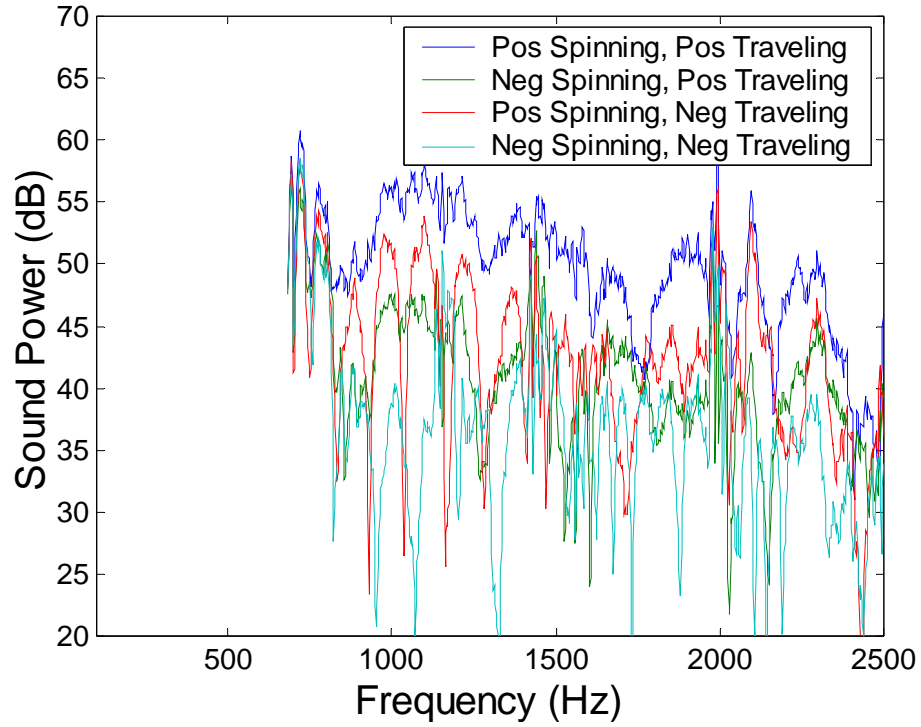


Figure 4-8: Sound power versus frequency of the (1,0) mode.

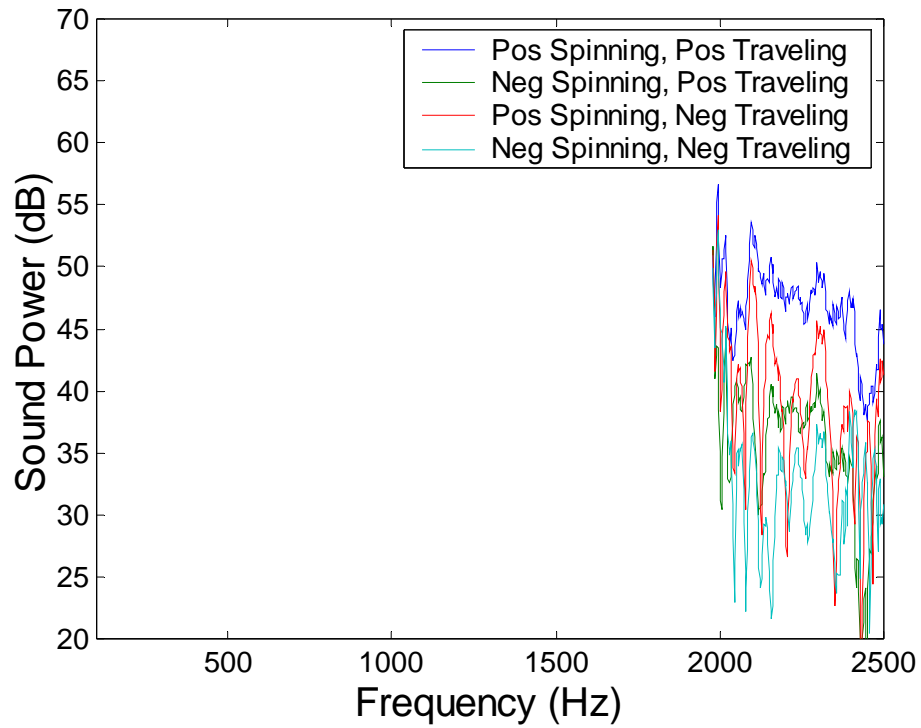


Figure 4-9: Sound power versus frequency of the (1,1) mode.

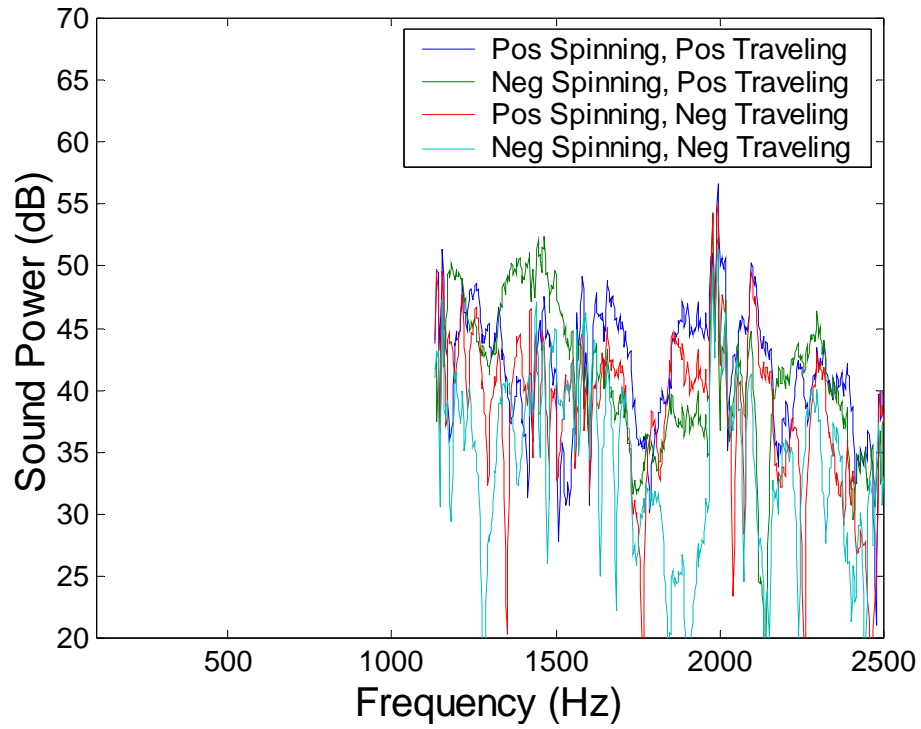


Figure 4-10: Sound power versus frequency of (2,0) mode.

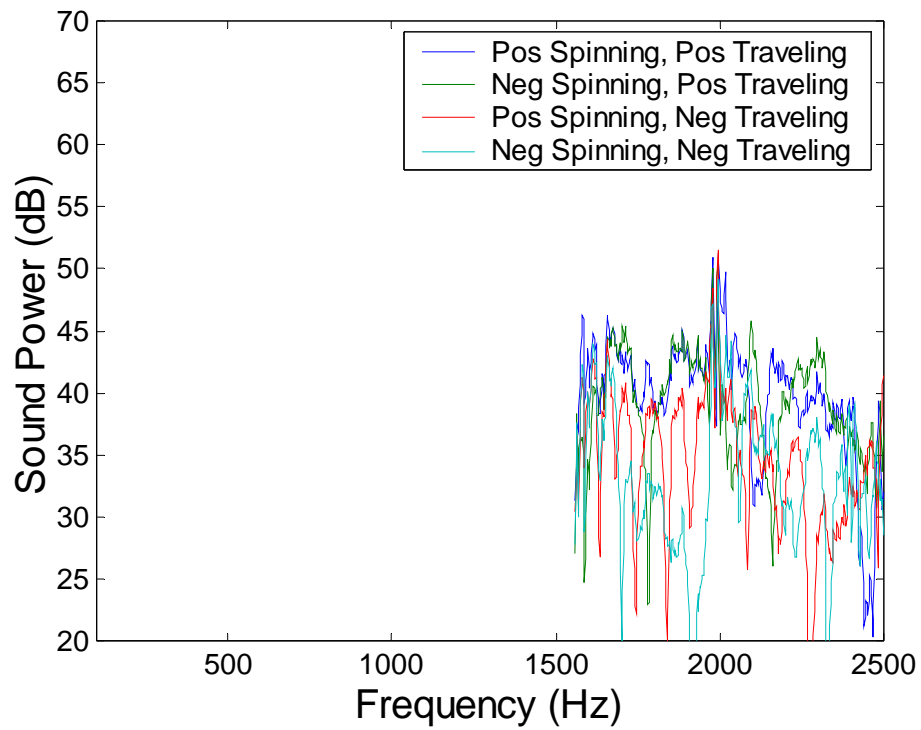


Figure 4-11: Sound power versus frequency of the (3,0) mode.

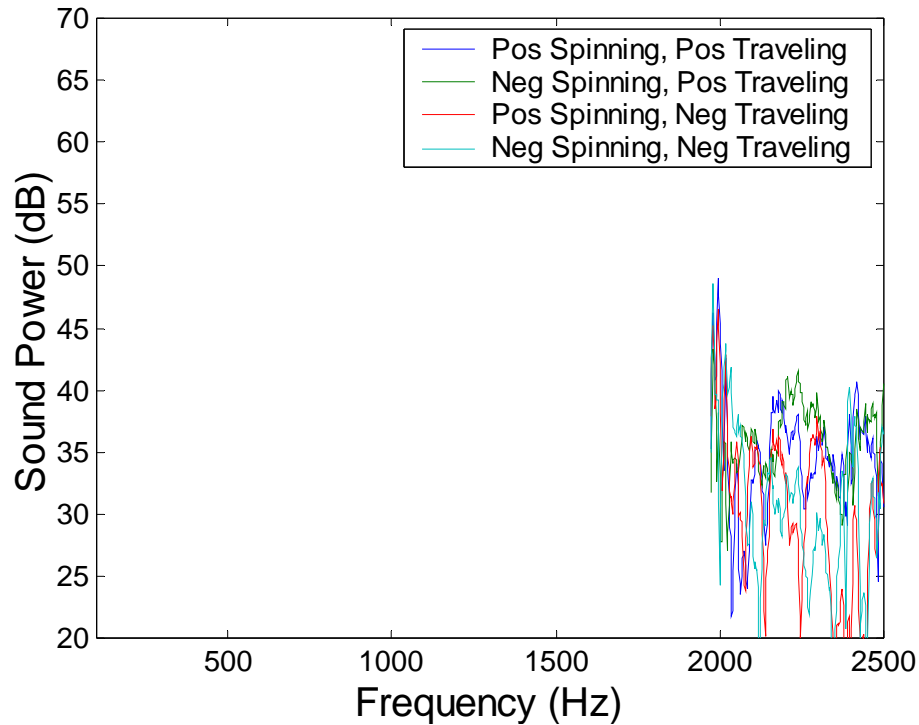


Figure 4-12: Sound power versus frequency of the (4,0) mode.

These results show that in order for the  $m$ -order 1 modes to dominate in the duct improvements must be made to avoid generating the  $m$ -order 0 modes.

The hard wall experimental incident modal amplitudes for each case can now be used as input into the analytical model. This will allow the theoretical predictions made using the HQ tube systems analytical model to be directly compared to the experimental results.

### 4.3 Analytical Incident Modal Amplitude Predictions

In order to make predictions using the HQ tube systems analytical model, the magnitude and phase of the incident modal amplitudes must be determined. To be consistent, the experimental incident modal amplitudes of the hard wall case are used as input into the analytical model. The magnitude of incident modes may be found using equation (3.15). The phase of the incident modal amplitude is arbitrary with only one

incident  $m$ -order mode present. However, with multiple incident modes the phase between radial modes is important because of their inherent difference in wave velocity. The relative phase of the modal amplitudes of the  $(\alpha,\beta)$  and  $(m,n)$  modes can be solved for using equation (3.19).

For example, for the hard wall case with a positive spinning and traveling  $m$ -order 1 incident mode, the (1,0) and (1,1) modes are both cut-on above 1973 Hz. The relative phase between the modal amplitudes of the (1,0) and (1,1) modes are shown in Figure 4-13 and show significant variability.

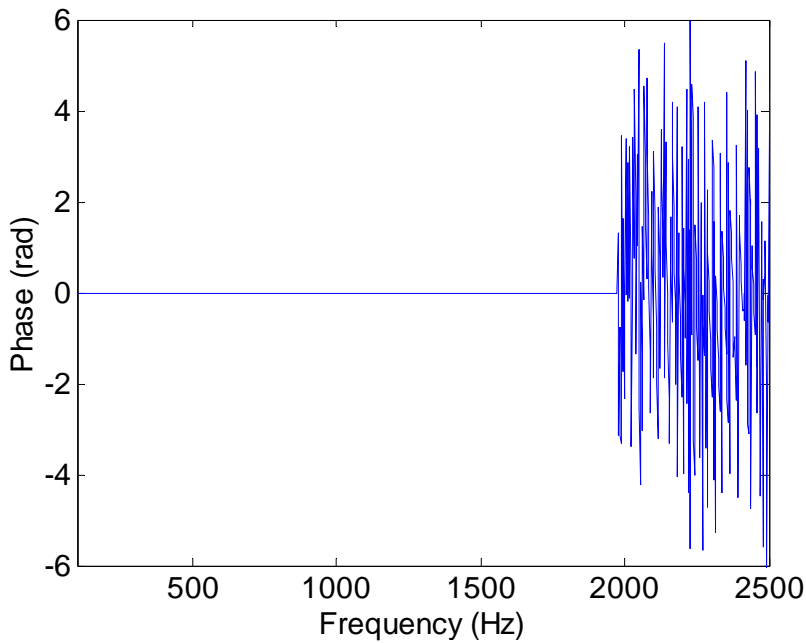


Figure 4-13: The relative modal amplitude phase of the (1,0) and (1,1) modes.

Because of the significant variability, an incident modal amplitude model was developed to examine the relative phase of like  $m$ -order incident modes.

A model was developed to predict the incident modes generated by the acoustic drivers. The acoustic drivers were modeled as piston sources. The modal amplitude of the positive spinning and traveling  $(m,n)$  mode generated by the acoustic drivers can be expressed as a summation of the modal amplitudes due to each piston source. That is

$$A_{mn}^{(++)} = \sum_{r=1}^{N_g} A_{mn,r}^{(++)} \quad (4.1)$$

## Chapter 4. Experimental Results

where the complex modal amplitude due to piston source  $r$ , located at  $z=0$  can be expressed from equation (2.13) as

$$A_{mn,r}^{(++)} = \frac{v_r k_o \rho c}{\pi a^2} \frac{J_m(k_{mn} a)}{\Lambda_{mn}(k_{mn,z}^{(+)} - k_{mn,z}^{(-)})} \frac{2a\alpha_r \sin(m\alpha_r)}{m\alpha_r} \frac{2d_r \sin(k_{mn,z}^{(+)} d_r)}{k_{mn,z}^{(+)} d_r} \frac{e^{+im\theta_r}}{2} \quad (4.2)$$

For the  $m=0$  mode which is non-spinning, the equation simplifies to

$$A_{0n,r}^{(++)} = \frac{v_r k_o \rho c}{\pi a^2} \frac{J_0(k_{0n} a)}{\Lambda_{0n}(k_{mn,z}^{(+)} - k_{mn,z}^{(-)})} 2a\alpha_r \frac{2d_r \sin(k_{mn,z}^{(+)} d_r)}{k_{mn,z}^{(+)} d_r} \quad (4.3)$$

The phase of the complex modal amplitude of the  $(m,n)$  mode is due to the piston source velocity  $v_r$ , and the Bessel function. The piston sources are equally spaced around the circumference of the duct. Thus, the resultant phase of  $v_r$ , summed over the piston sources is zero. The Bessel function  $J_m$ , is actually the reason for the phase change. Each circumferential order mode has many radial orders. Each radial order resulting from the  $n^{\text{th}}$  inflection point of the  $m^{\text{th}}$  order Bessel function of the first kind. The Bessel function is sinusoidal and oscillates about zero. Thus, the value of  $J_m$  evaluated at its inflection point alternates sign from positive to negative. This results in increasing radial order modes of like  $m$ -order being out of phase with respect to one another.

These results were examined by assuming the incident modal amplitudes of the case above were in-phase and out-of-phase, and comparing the analytical and experimental modal power results. Assuming the (1,0) and (1,1) modes are in-phase and out-of-phase, the total sound power reduction results are shown in Figure 4-14 and Figure 4-15, respectively.

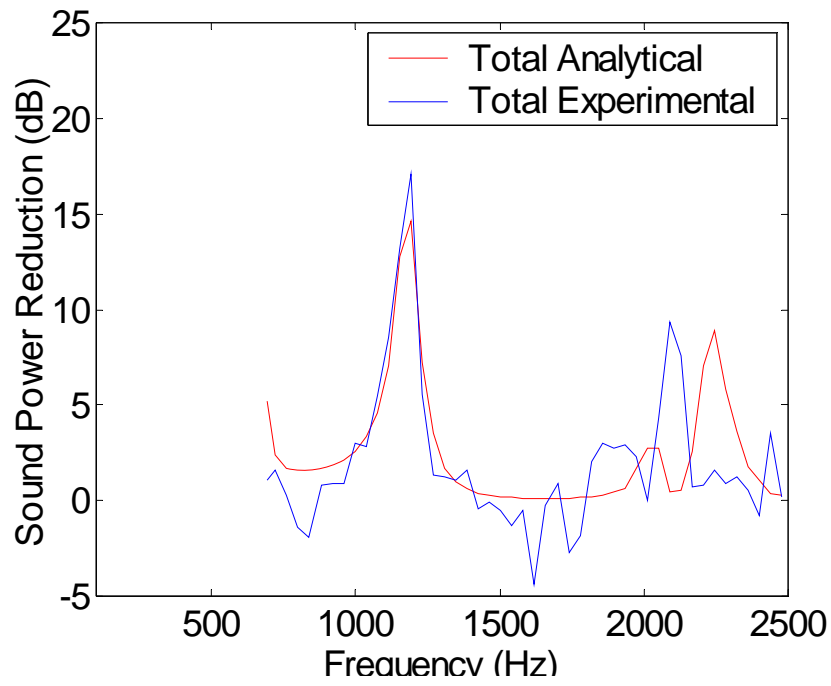


Figure 4-14: Total sound power reduction of the  $m$ -order 1 modes, in-phase.

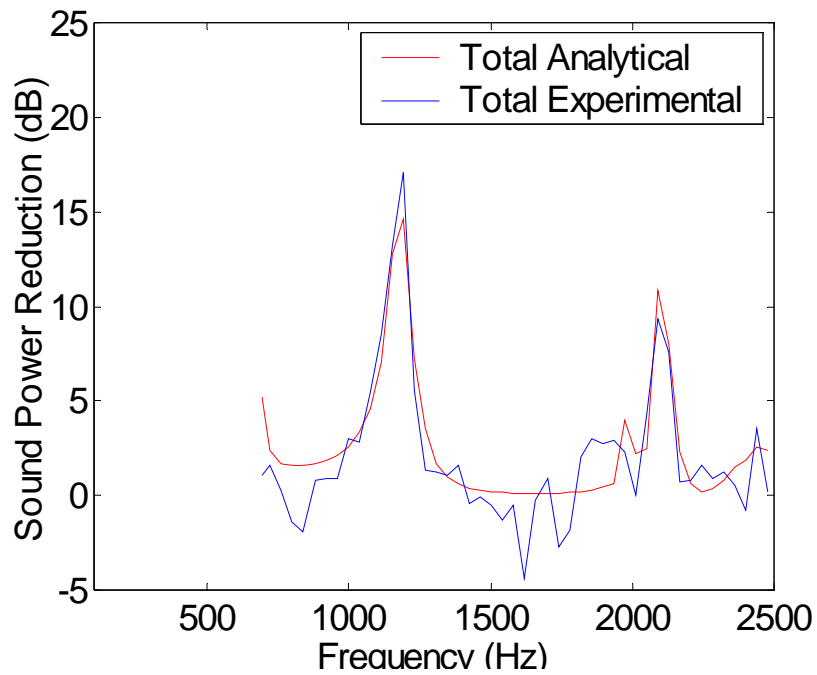


Figure 4-15: Total sound power reduction of the  $m$ -order 1 modes, out-of-phase.

Above 1973 Hz where the (1,0) and (1,1) modes are present, the results show poor agreement assuming the incident complex modal amplitudes are in-phase. However, assuming the complex modal amplitudes are out-of-phase, the results are in very good agreement. Thus, supporting the incident modal amplitude model. With this knowledge, it is understood that incident modes of like  $m$ -order are out-of-phase with respect to each other. The magnitude and phase of the experimental incident modes is used as input into the HQ tube analytical model to produce all analytical results.

These modal sound power results presented here and in section 4.4 were averaged over a 39 Hz bandwidth (16 spectral lines) and the average power assigned to the center frequency of that band.

### **4.4 Theoretical vs. Experimental Modal Power Comparisons**

A set of experiments was designed to fundamentally study the noise control mechanisms of the HQ tubes and allow evaluation of the VPI analytical model. Experimental tests were performed for the simplest of cases with one incident mode, one transmitted mode, and no scattered modes to more complex cases with multiple incident modes, radial scattering, and circumferential scattering. For each case the incident, transmitted, reflected, and scattered modes in the duct were studied. The effects of changing the HQ tube system parameters were also investigated. The axial position of the HQ tube circumferential array was varied from positions 1 through 7. The number of HQ tubes in the circumferential array and the number of circumferential arrays of HQ tubes was varied from 8 to 16 tubes and 1 to 2 arrays, respectively. The experimental setup schematic can be found in Figure 3-10. The experimental incident modal sound power in the duct was measured for the hard-wall condition for each case and used as the incident modal amplitudes in the analytical predictions.

The results for five different test cases are presented in the following sections. The experimental modal powers are a result of applying the data analysis and post processing technique described in section 3.2 to the microphone measurements. The HQ

## Chapter 4. Experimental Results

tube model was used to predict the analytical modal powers. The plots of the test results show the experimental results in blue compared to the analytical predictions in red. Additional information plotted is shown in the plot legend.

For sake of clarity, the sign convention for the plot captions is defined as

$$W_*^{(st)}$$

where  $W$  represents sound power. The induce  $*$  represents the sound power type plotted:  $I$  for incident,  $T$  for transmitted,  $R$  for reflected, and  $Red$  for reduction. The parameter  $s$  may be  $+$  or  $-$  indicating positive or negative spinning and the parameter  $t$  may be  $+$  or  $-$  indicating positive or negative traveling. Thus  $W_I^{+-}$  reads, positive spinning and traveling incident sound power. Conversely  $W_{Red}^{++}$  reads, positive spinning and traveling sound power reduction.

#### 4.4.1 Test 1: Single Incident Mode

##### Objectives and Description

The first experiment is designed to study the most fundamental HQ tube noise control mechanism, single mode reflection. To accomplish this, the acoustic drivers must generate only one disturbance mode. The (2,0) disturbance mode is chosen for the fact that it has a relatively low cut-off frequency of 1130 Hz and its higher order radial modes are cut-off in the frequency range of interest. Using a single array of 16 HQ tubes in position 4 (1.08 m) avoids circumferential scattering due to the special aliasing in the number of HQ tubes. The (2,0) disturbance mode will propagate to the tube-duct interfaces with some of its energy transmitting upstream while some is reflected downstream. With no radial or circumferential scattering present and a low cut-off frequency allowing multiple HQ tube resonance this is an excellent case to study single mode reflection. The experimental setup is shown in Figure 4-16.

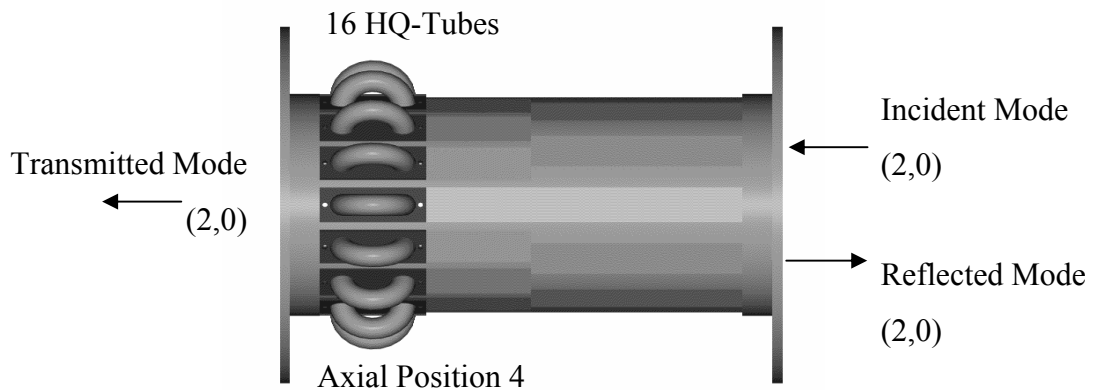


Figure 4-16: Test 1 experimental setup with HQ tube system

##### Test 1 Results: Single Incident Mode

The incident sound power of the positive spinning and traveling (2,0) mode is generally decaying as shown in Figure 4-17. The (2,0) mode shows a very good agreement between level, shape, and HQ tube system resonance frequencies for the transmitted sound power and sound power reduction shown in Figure 4-18 and Figure

4-19, respectively. The sound power reduction level is high at the cut-off frequency and starts close to the HQ tube systems 1<sup>st</sup> resonance at 1269 Hz. The reduction level then decreases exponentially and spikes at the 2<sup>nd</sup> system resonance at 2207 Hz.

The reflected sound power of the positive spinning and negative traveling (2,0) mode with the HQ tube system is shown in Figure 4-20. Generally, there is a good agreement in shape and level of the reflected sound power. However, the experimental sound power shows significantly more oscillation. At the 1<sup>st</sup> and 2<sup>nd</sup> resonances of the system the reflected sound power of the HQ tube system is much higher than the hard-wall case. This suggests the sound power reduction is due to single mode reflection. This is expected because of the significant reflection that occurs at the resonance of the HQ tube system.

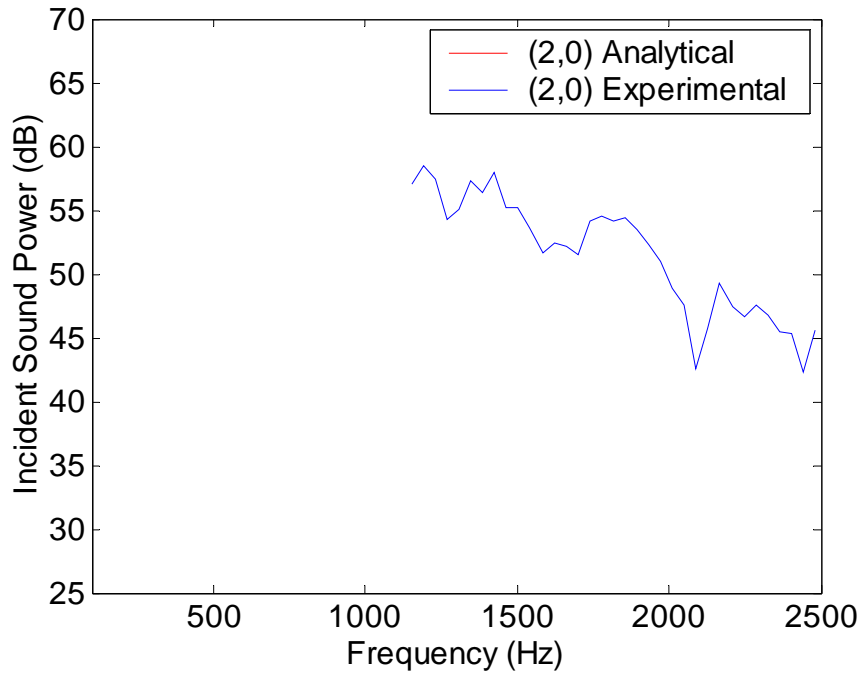


Figure 4-17: Experimental  $W_I^{++}$  of the (2,0) mode.

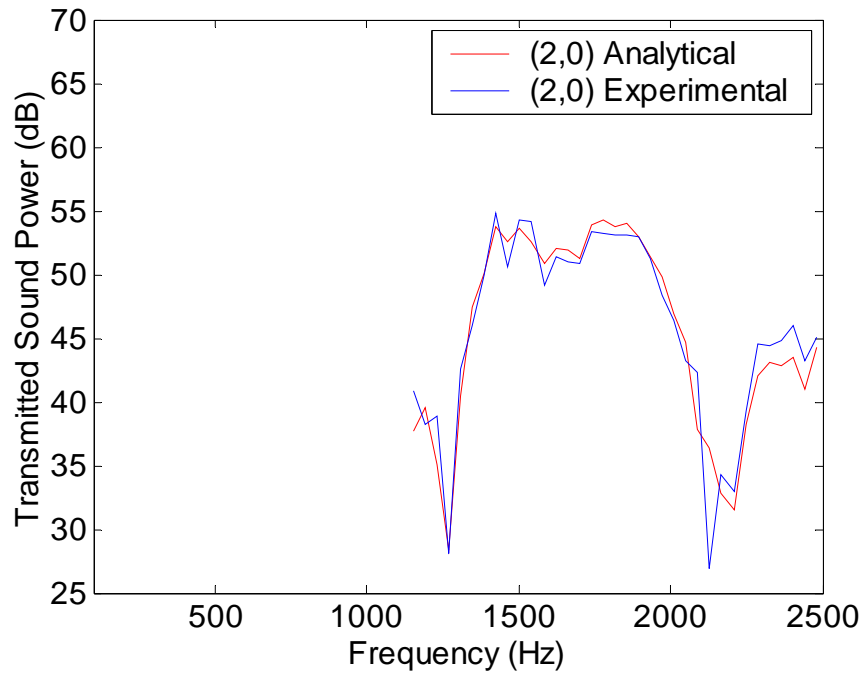


Figure 4-18: Analytical versus experimental  $W_T^{++}$  of the (2,0) mode with 16 HQ tubes in position 4.

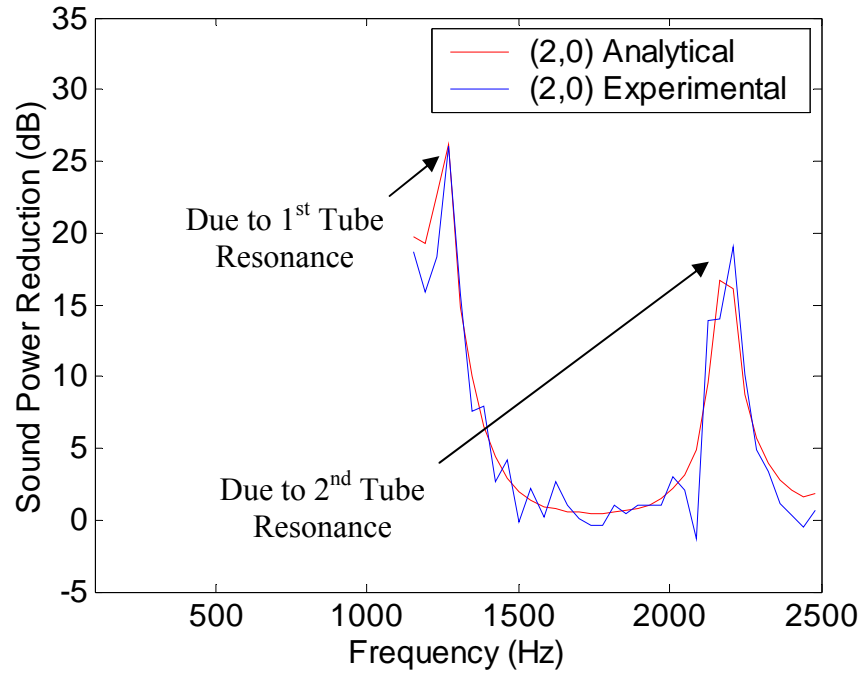


Figure 4-19: Analytical versus experimental  $W_{Red}^{++}$  of the (2,0) mode with 16 HQ tubes in position 4.

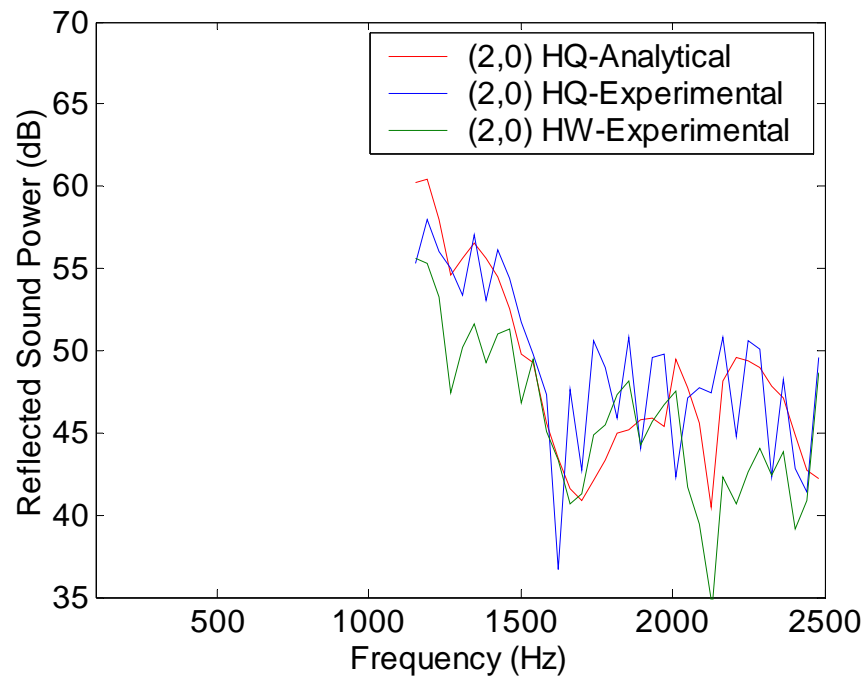


Figure 4-20: The (2,0) mode: analytical versus experimental  $W_R^{+-}$  with 16 HQ tubes in position 6 compared to the experimental hard wall  $W_R^{+-}$ .

## 4.4.2 Test 2: Number of HQ Tubes

### Objectives and Description

This experiment investigates the effects of varying the number of HQ tubes on the single mode reflection noise control mechanism studied in section 4.4.1. To accomplish this, measurements are made with a single array of both 8 and 16 HQ tubes in position 4 (1.08 m). The acoustic drivers generated the (2,0) incident mode with a cut-off frequency of 1130 Hz. The (2,0) disturbance mode will propagate to the tube-duct interfaces with some of its energy transmitting upstream while some is reflected downstream. There is no radial or circumferential scattering present at the frequencies of interest. The experimental setup with 8 and 16 HQ tubes is shown in Figure 4-21 and Figure 4-22, respectively.

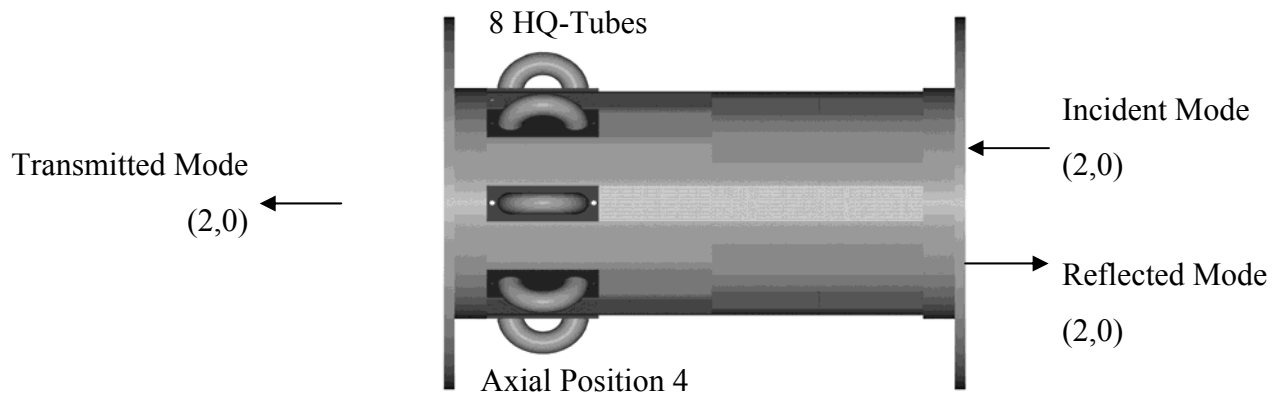


Figure 4-21: Test 2 experimental setup with 8 HQ tubes.

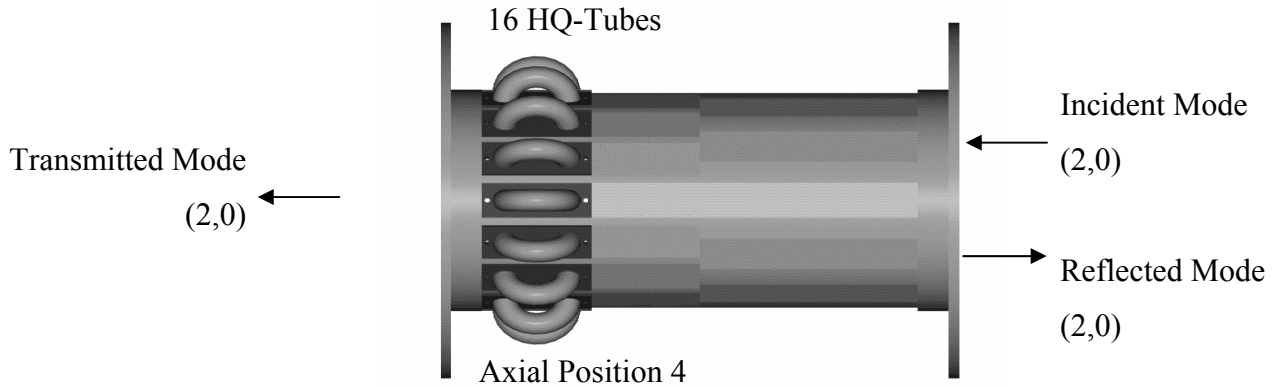


Figure 4-22: Test 2 experimental setup with 16 HQ tubes.

### Test 2 Results: Number of HQ Tubes

The sound power reduction for HQ tube systems with 8 and 16 HQ tubes are shown in Figure 4-23 and Figure 4-24, respectively. These figures show very accurate predictions in shape, level, and HQ tube resonance frequencies. Increasing the number of HQ tubes from 8 to 16 increases the 1<sup>st</sup> and 2<sup>nd</sup> resonant frequencies of the HQ tube system from 1152 and 2168 Hz to 1270 and 2207 Hz. Increasing the number of HQ tubes also increases the level of maximum attenuation. With 8 HQ tubes there is poor agreement between analytical and experimental sound power reduction at the cut-off frequency.

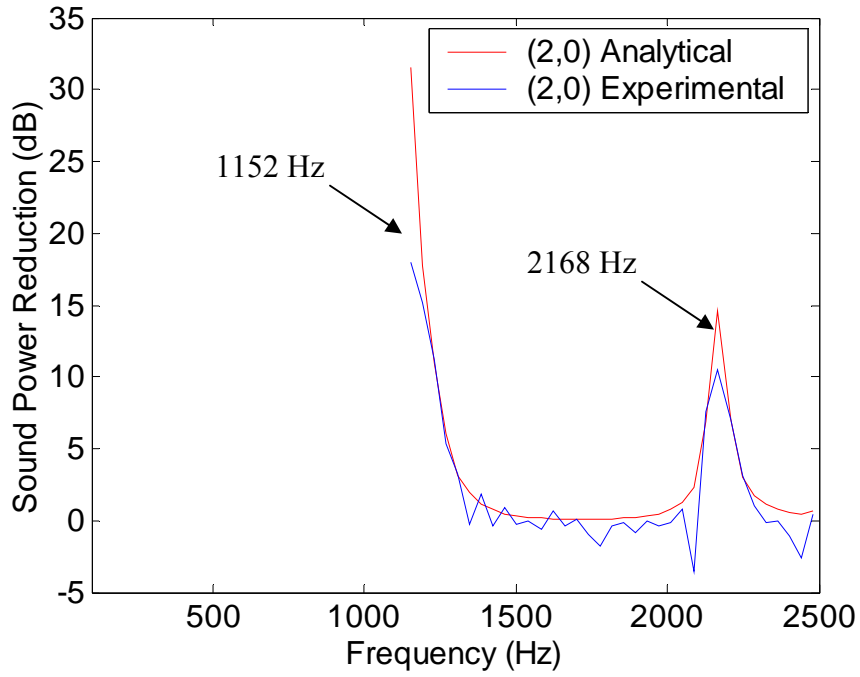


Figure 4-23: Analytical versus experimental  $W_{Red}^{++}$  of the (2,0) mode with 8 HQ tubes in position 4.

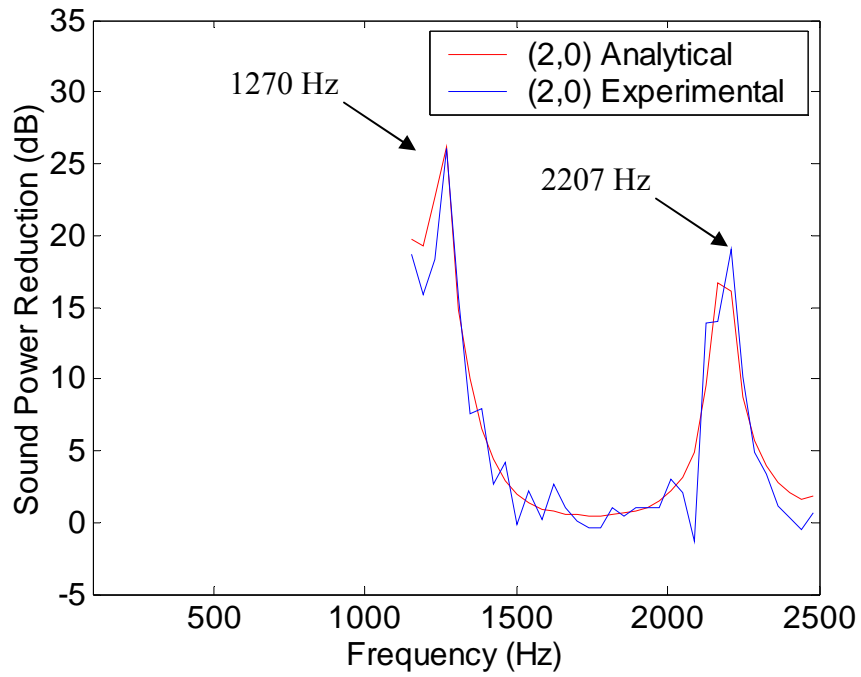


Figure 4-24: Analytical versus experimental  $W_{Red}^{++}$  of the (2,0) mode with 16 HQ tubes in position 4.

### 4.4.3 Test 3: Multiple Incident Modes

#### Objectives and Description

The previous tests in sections 4.4.1 and 4.4.2 studied cases where the only attenuation mechanism occurring was reflection of the incident energy. This experiment is designed to examine a more complex case with multiple incident modes all of the same circumferential order,  $m=0$ . This test investigates radial scattering in addition to reflection as attenuation mechanisms. The incident disturbance is comprised of the modes (0,0) and (0,1) with a cut-off frequency of 0 and 1418 Hz, respectively. A single array of 16 HQ tubes is located at position 1 (0.683 m). At the tube-duct interfaces some of the energy of the (0,0) and (0,1) modes is transmitted upstream while some is reflected downstream. In addition, there is a possibility of radial scattering of energy between the (0,0) and (0,1) modes. The experimental setup is shown in Figure 4-25.

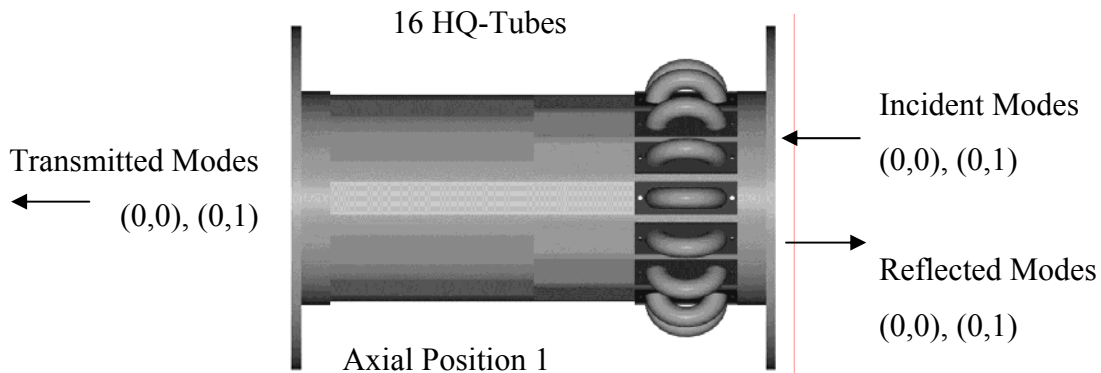


Figure 4-25: Test 3 experimental setup with HQ tube system.

#### Test 3 Results: Multiple Incident Modes

The HQ tubes are very effective at reducing the noise at the end of the duct as seen in the sound power reduction of the total  $m$ -order 0, (0,0), and (0,1) modes, shown in Figure 4-32 through Figure 4-34, respectively. There is significant attenuation at the 1<sup>st</sup> and 2<sup>nd</sup> resonant frequencies of the HQ tube system, approximately 1113 Hz and 2207 Hz respectively. The analytical model does well in predicting the frequencies of maximum reduction but under predicts the sound power reduction at the systems 1<sup>st</sup> resonance while it over predicts the reduction at the 2<sup>nd</sup> resonance. There is also poor agreement at

frequencies around 950, 1600, and 2360 Hz. At these frequencies the total  $m$ -order 0, (0,0), and (0,1) incident modes show extremely low levels in Figure 4-26 through Figure 4-28, respectively. The analytical model predicts minimal change in sound power level at these frequencies from the incident to transmitted modes. However, the experimental results show a change of approximately 5 dB in level at these frequencies from the incident to transmitted modes. This causes differences in sound power reduction levels between the analytical and experimental. The transmitted sound power for the total  $m$ -order 0, (0,0), and (0,1) modes are shown in Figure 4-29 through Figure 4-31, respectively.

In order to have insight into the attenuation mechanisms in this test the reflected modes must be examined in addition to the incident and transmitted modes. The reflected sound power results for the positive spinning and negative traveling total  $m$ -order 0, (0,0), and (0,1) modes are shown in Figure 4-35 through Figure 4-37, respectively. There is significantly more reflection at the systems 1<sup>st</sup> and 2<sup>nd</sup> resonance frequencies with the HQ tube system than with the hard wall case. Suggesting that a significant source of the sound power reduction is due to reflection. The reflected sound power generally agrees in shape with large discrepancies in level except at the cut-off frequency of the (0,1) mode.

Figure 4-36 shows the reflected sound power of the (0,0) mode as greater than the incident sound power around the 2<sup>nd</sup> resonant frequencies of the HQ tube system. This indicates possible scattering of energy from the (0,1) mode to the (0,0) mode. However, Figure 4-35 of the total  $m$ -order 0 modes show higher levels of reflected sound power than incident at these frequencies. This inaccuracy is due to the limitations with the experimental setup that prevented incident, transmitted, and reflected mode measurements from occurring at the same time. In this case the incident sound power must have varied slightly in the duct from one run to another. Thus, the effects of radial scattering cannot be determined from the reflected power results.

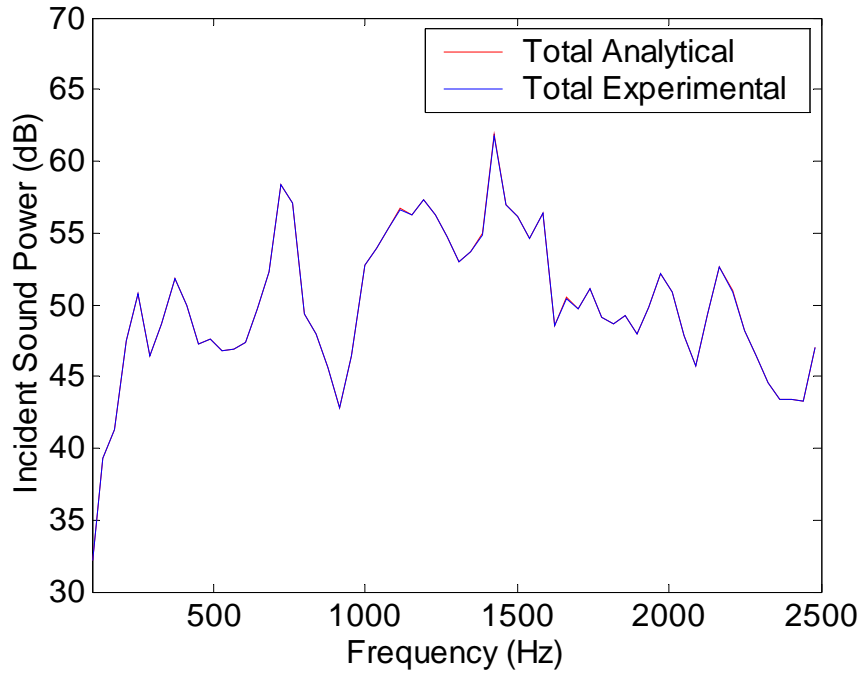


Figure 4-26: Experimental total  $W_l^{++}$  of the  $m$ -order 0 modes.

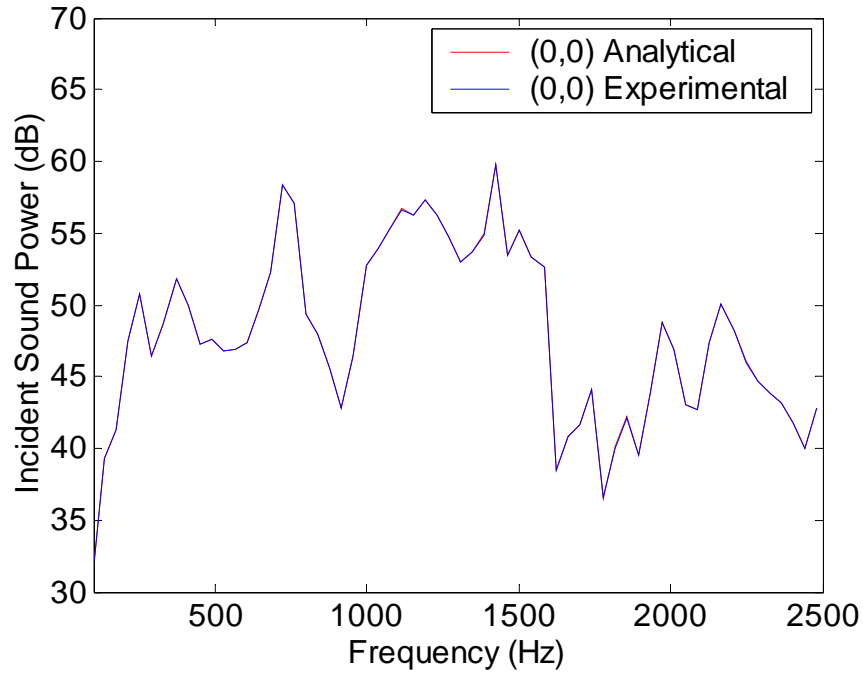


Figure 4-27: Experimental  $W_l^{++}$  of the (0,0) mode.

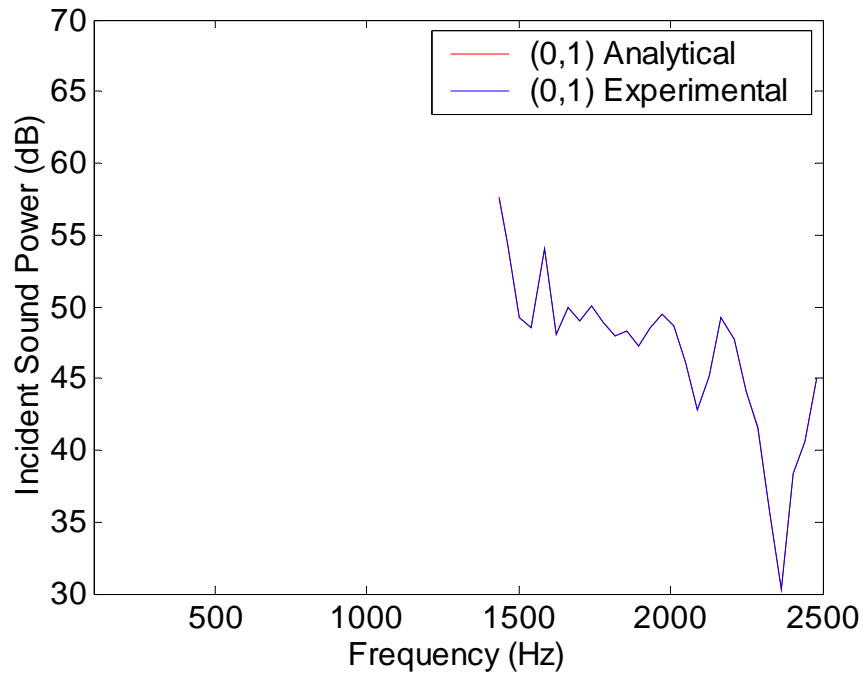


Figure 4-28: Experimental  $W_I^{++}$  of the (0,1) mode.

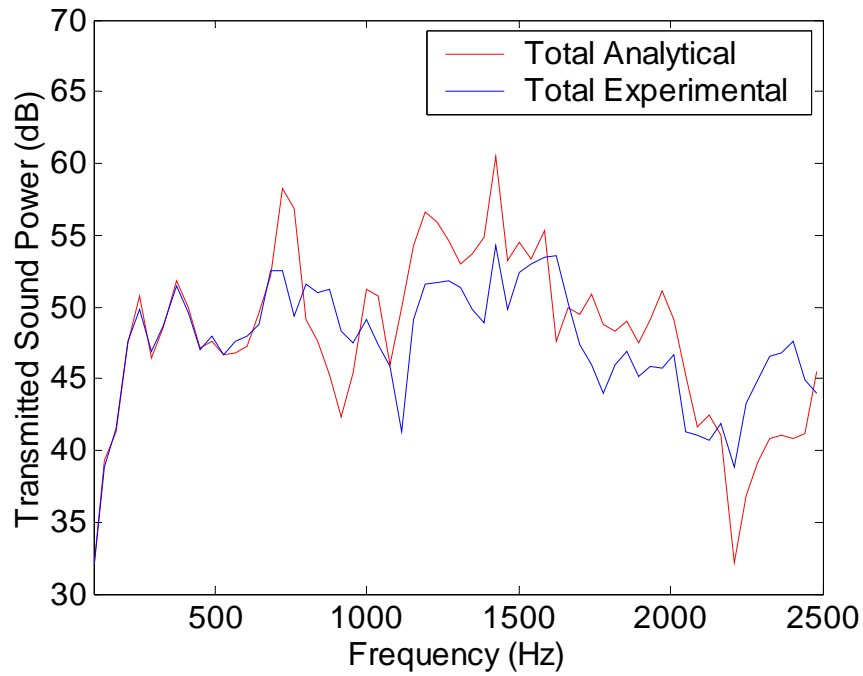


Figure 4-29: Analytical versus experimental total  $W_T^{++}$  of the  $m$ -order 0 modes with 16 HQ tubes in position 1.

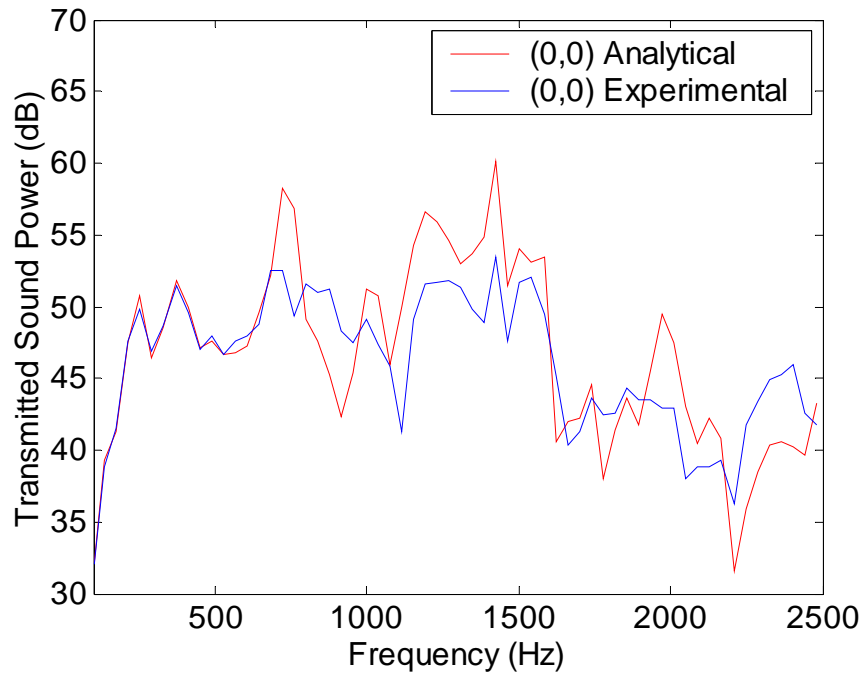


Figure 4-30: Analytical versus experimental  $W_T^{++}$  of the (0,0) mode with 16 HQ tubes in position 1.

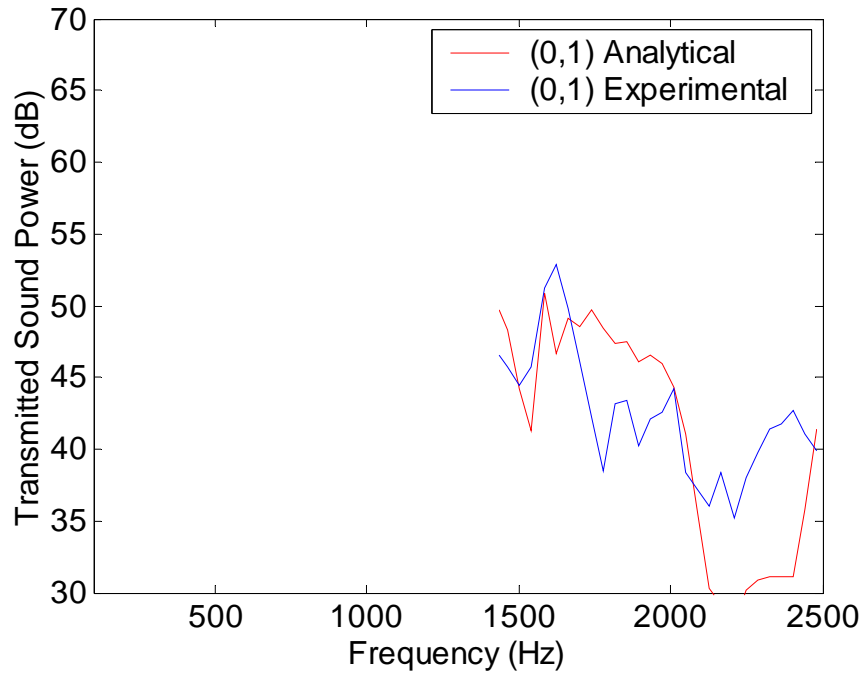


Figure 4-31: Analytical versus experimental  $W_T^{++}$  of the (0,1) mode with 16 HQ tubes in position 1.

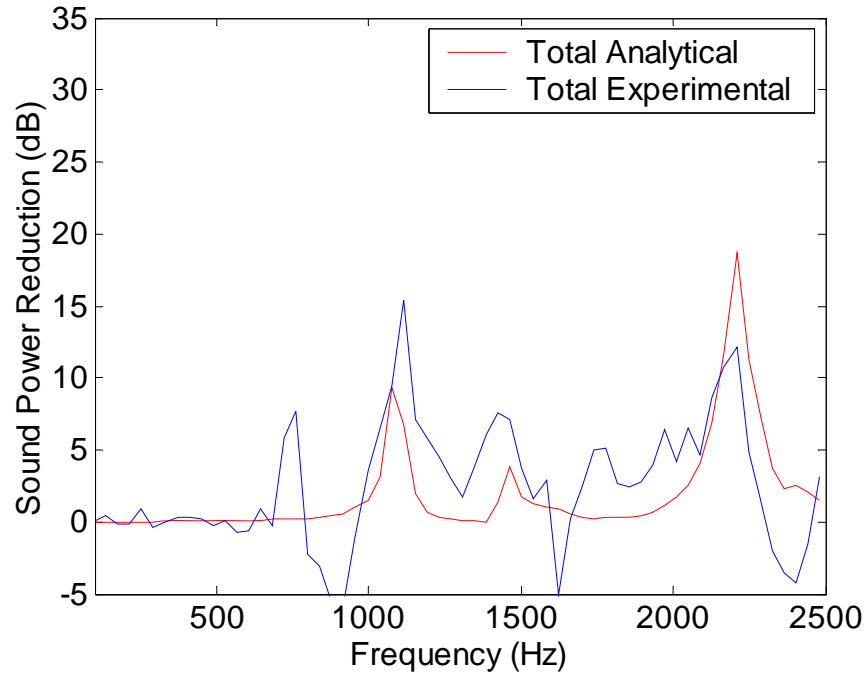


Figure 4-32: Analytical versus experimental total  $W_{Red}^{++}$  of the  $m$ -order 0 modes with 16 HQ tubes in position 1.

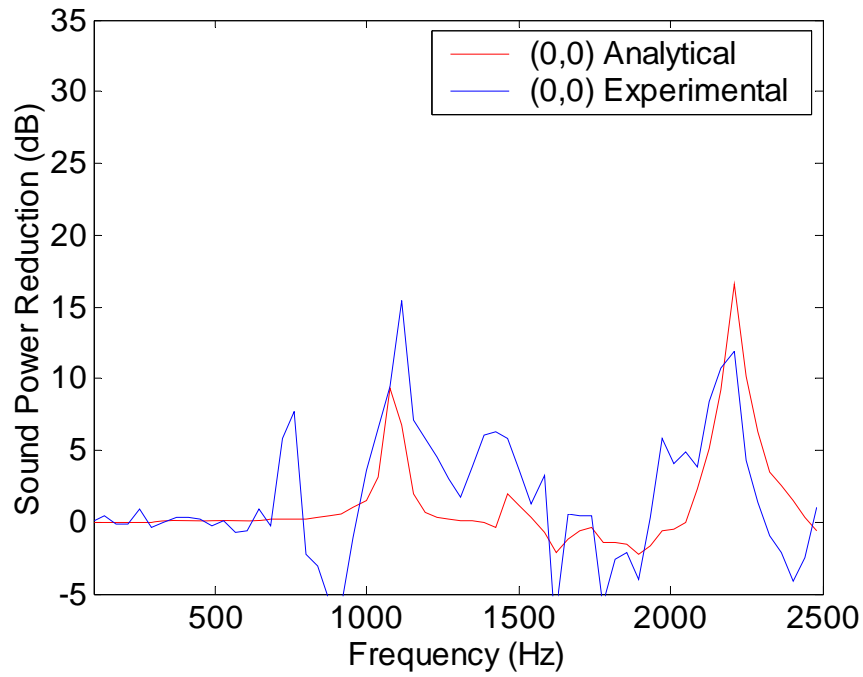


Figure 4-33: Analytical versus experimental  $W_{Red}^{++}$  of the (0,0) mode with 16 HQ tubes in position 1.

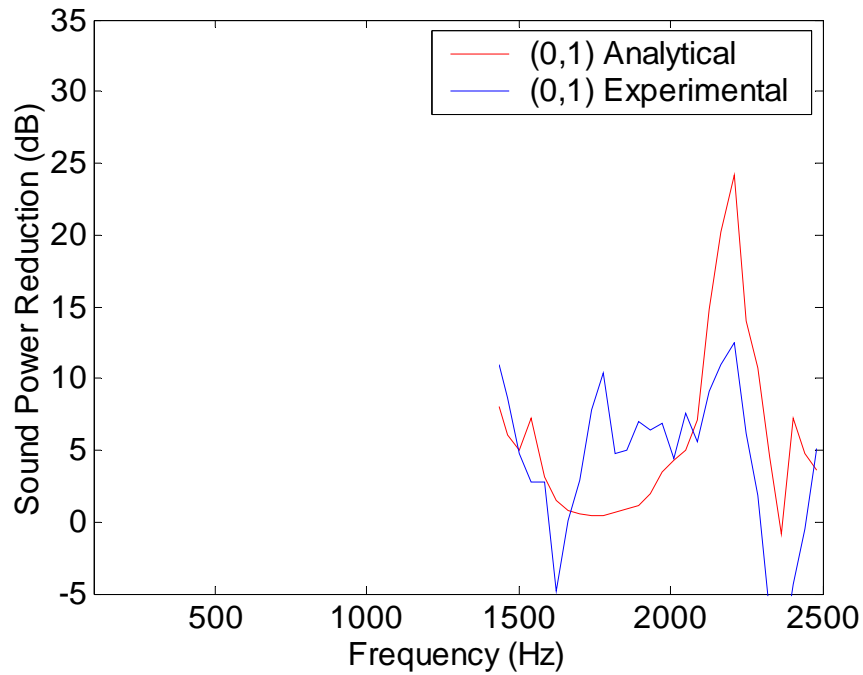


Figure 4-34: Analytical versus experimental  $W_{Red}^{++}$  of the (0,1) mode with 16 HQ tubes in position 1.

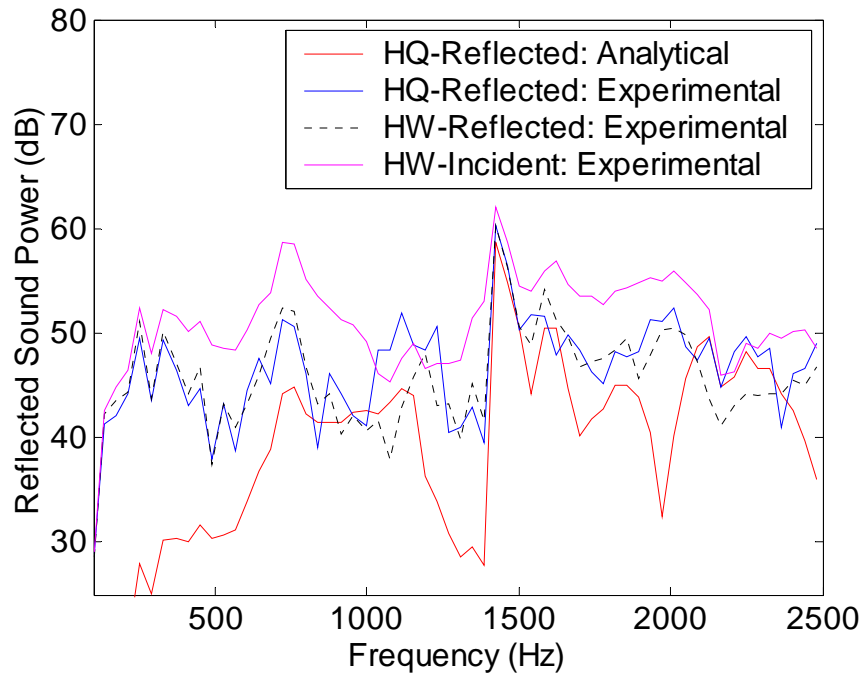


Figure 4-35: The  $m$ -order 0 modes: analytical versus experimental total  $W_R^{+-}$  with 16 HQ tubes in position 6 compared to the experimental hard wall  $W_R^{+-}$  and  $W_I^{++}$ .

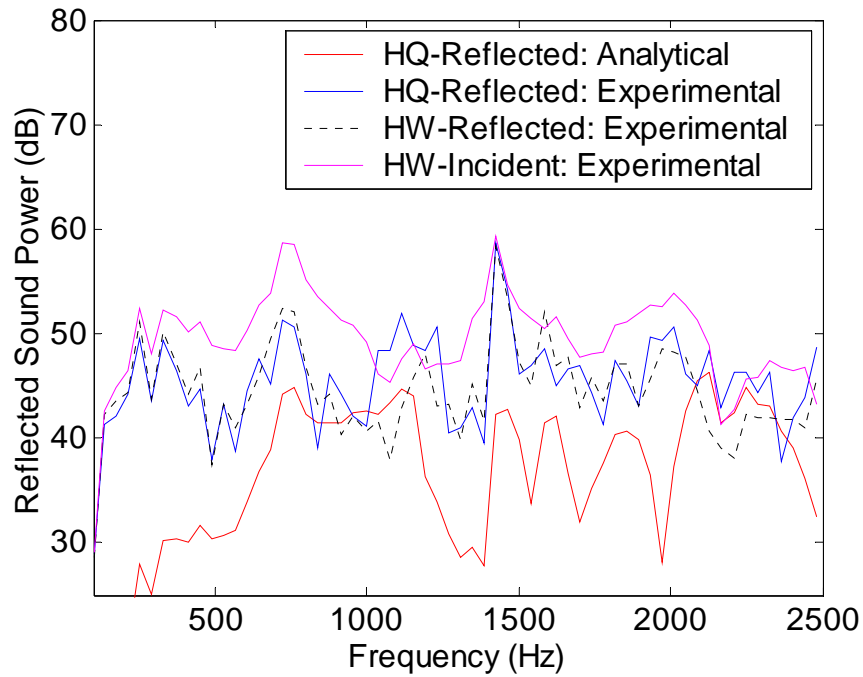


Figure 4-36: The (0,0) mode: analytical versus experimental  $W_R^{+-}$  with 16 HQ tubes in position 6 compared to the experimental hard wall  $W_R^{+-}$  and  $W_I^{++}$ .

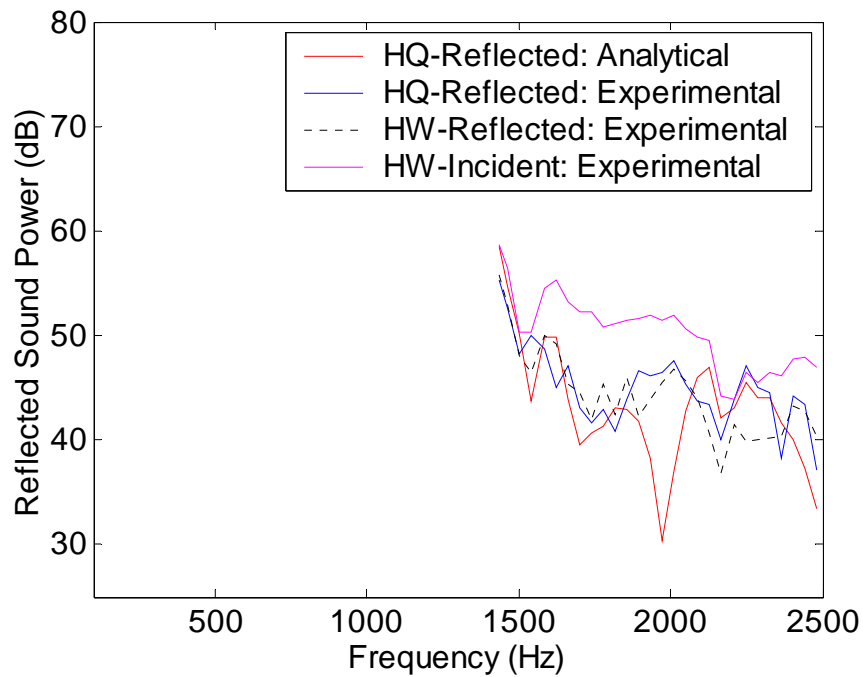


Figure 4-37: The (0,1) mode: analytical versus experimental  $W_R^{+-}$  with 16 HQ tubes in position 6 compared to the experimental hard wall  $W_R^{+-}$  and  $W_I^{++}$ .

#### **4.4.4 Test 4: Multiple Incident Modes, Effects of Axial Position, Radial Scattering, and Multiple Arrays**

##### **Objectives and Description**

This experiment is designed to investigate how changes in HQ tube array axial position and numbers of HQ tubes arrays affect a system with multiply incident modes. The incident disturbance in this test is comprised of the modes (1,0) and (1,1) with cut-off frequency of 681 and 1973 Hz, respectively. With multiple incident modes there is a relative phase change created from the differences in wave velocity. Thus, there are axial positions along the duct that will maximize the reduction provided by the HQ tube array by optimizing the recombination of the spill of energy between the modes. To study the affect of axial position change measurements were made with the HQ tube array in axial positions 1 through 4.

With multiple incident modes of the same circumferential order,  $m=1$  present the effects of radial scattering will be investigated. At the HQ tube array interface some of the energy of the (1,0) and (1,1) modes is transmitted upstream while some is reflected downstream. Due to the radial scattering there may also be energy exchange between the (1,0) and (1,1) modes. No circumferential scattering is present in this experiment.

To this point all the measurements have been made with only one array of HQ tubes. It is of interest to determine if additional attenuation would occur with multiple arrays of HQ tubes. Measurements were performed with 1 and 2 arrays of HQ tubes. The experimental setup is shown in Figure 4-38.

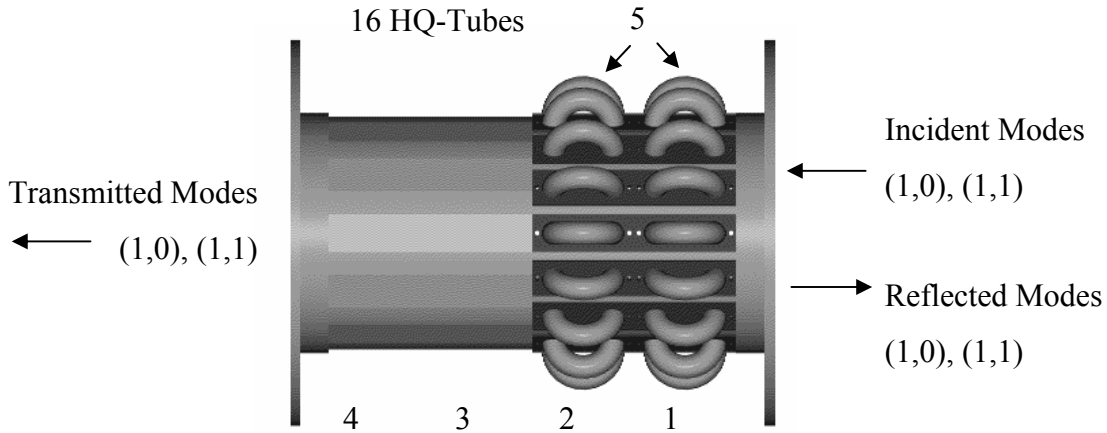


Figure 4-38: Test 3 experimental setup with HQ tube system

#### **Test 4 Results: Multiple Incident Modes, Effects of Axial Position, Radial Scattering, and Multiple Arrays**

The results of this experiment enabled evaluation of the analytic models ability to predict the effects of axial position, radial scattering, and multiple arrays. The positive spinning and traveling incident sound power of the total  $m$ -order 1, (1,0), and (1,1) modes, are shown in Figure 4-39 through Figure 4-41, respectively. An example of the transmitted sound power of the total  $m$ -order 1, (1,0), and (1,1) modes for position 1 are shown in Figure 4-42 through Figure 4-44, respectively. The sound power reduction of the (1,0) mode is predicted very accurately in shape, level, and resonance frequency before the cut-on of the (1,1) mode at 1973 Hz. The (1,1) mode generally has good agreement with some discrepancies in shape and level. The sound power reduction level starts close to zero and spikes at the 1<sup>st</sup> HQ tube system resonance, and then returns to zero and spikes at the 2<sup>nd</sup> system resonance.

Measurements were made with the HQ tube array in positions 1 through 4. The sound power reduction results of the total  $m$ -order 1, (1,0), and (1,1) modes for positions 1 through 4 are shown in Figure 4-45 through Figure 4-56, respectively. Up until the 1973 Hz cut-off frequency of the (1,1) mode the (1,0) mode is the only mode present in the duct. With one incident mode the attenuation provided by the HQ tubes is unaffected by variation in the axial position of the HQ tubes. The results show that for a single mode in the duct the frequency and magnitude of maximum sound power reduction is

independent of the axial position of the HQ tube array. However, with multiple incident modes there is a sinusoidal variation of the frequency and level of maximum reduction. This sinusoidal variation is a result of the relative phase change created from the differences in wave velocity of the (1,0) and (1,1) modes. With both the (1,0) and (1,1) modes cut-on, the sinusoidal variation of the frequency of maximum sound power reduction is predicted very accurately in Figure 4-57. The level of maximum reduction varies slightly from the analytical predictions as seen in Figure 4-58.

The positive spinning and negative traveling reflected sound power of the total  $m$ -order 1, (1,0), and (1,1) modes are shown in Figure 4-59 through Figure 4-61, respectively. The reflected sound power generally agrees in shape with some discrepancies in level. Figure 4-60 shows significantly more reflection at the systems 1<sup>st</sup> resonance with the HQ tube system than with the hard wall case. This suggests the sound power reduction is due to single mode reflection of the (1,0) mode. Figure 4-60 also shows that for the (1,0) mode around 2300 Hz there is more reflected sound power with the HQ tubes than was incident. The only possible explanation is radial scattering, in which energy of the (1,1) mode scattered into the (1,0) mode. This explanation is supported in Figure 4-61, which shows that with the HQ tube system the reflected sound power of the (1,1) mode around 2300 Hz is much less than the incident sound power.

The results show that increasing the number of HQ tube arrays from 1 to 2 can significantly increase the levels of attenuation, as seen in Figure 4-62 through Figure 4-64. There is very good agreement of the (1,0) mode before the cut-on of the (1,1) mode. With both the (1,0) and (1,1) modes cut-on there is good agreement in shape and tube resonance. However, the analytical sound power reduction level under predicts the experimental by 3-5 dB.

The analytical model repeatedly over predicts the sound power reduction at the cut-off frequency of the (1,0) mode. This could be a result of the theoretical model not taking into account the reflection at open end of the duct. Additionally, the sound power reduction level at the cut-off frequency of (1,1) mode is generally in poor agreement with no discernable trend.

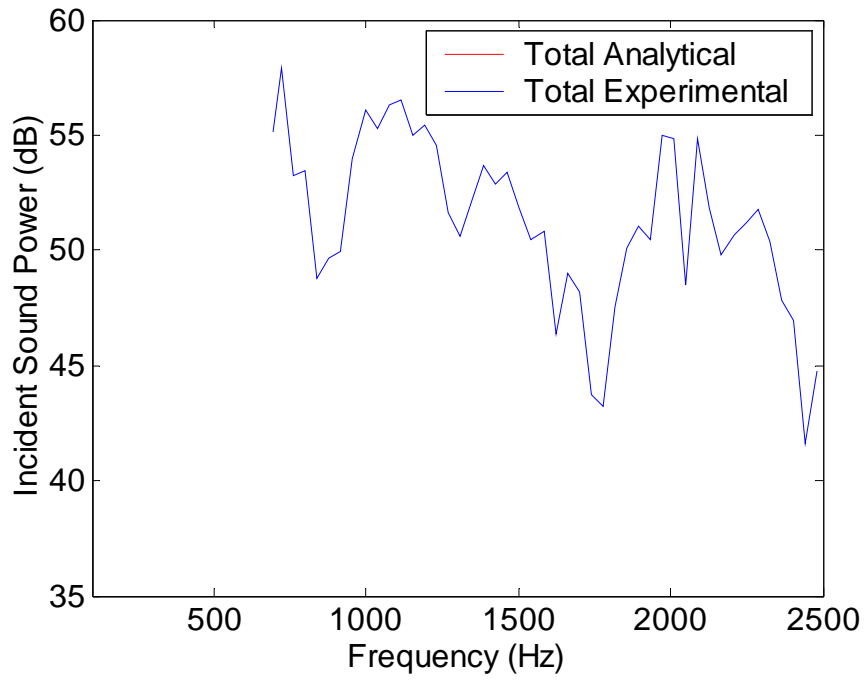


Figure 4-39: Experimental total  $W_I^{++}$  of the  $m$ -order 1 modes.

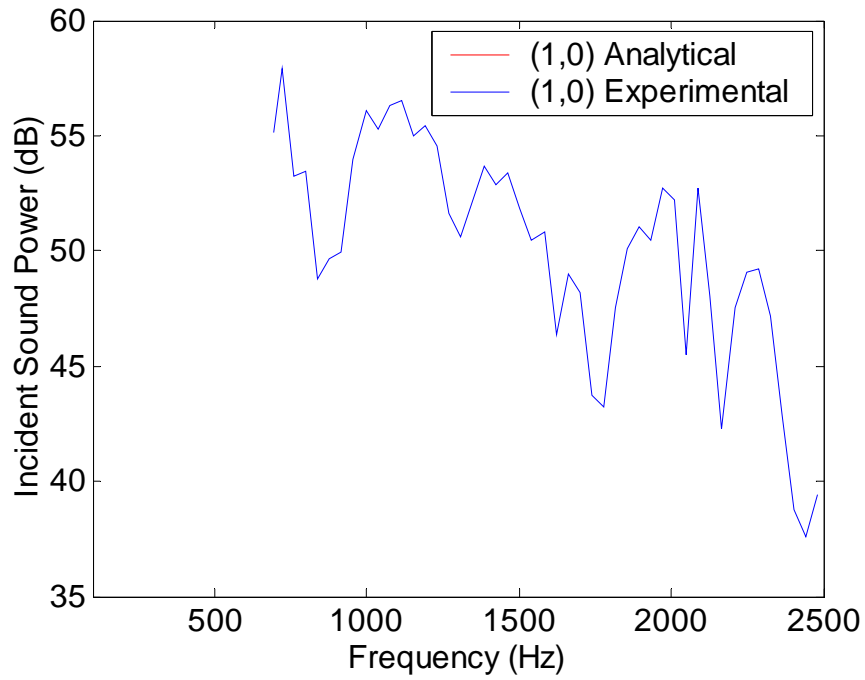


Figure 4-40: Experimental  $W_I^{++}$  of the (1,0) mode.

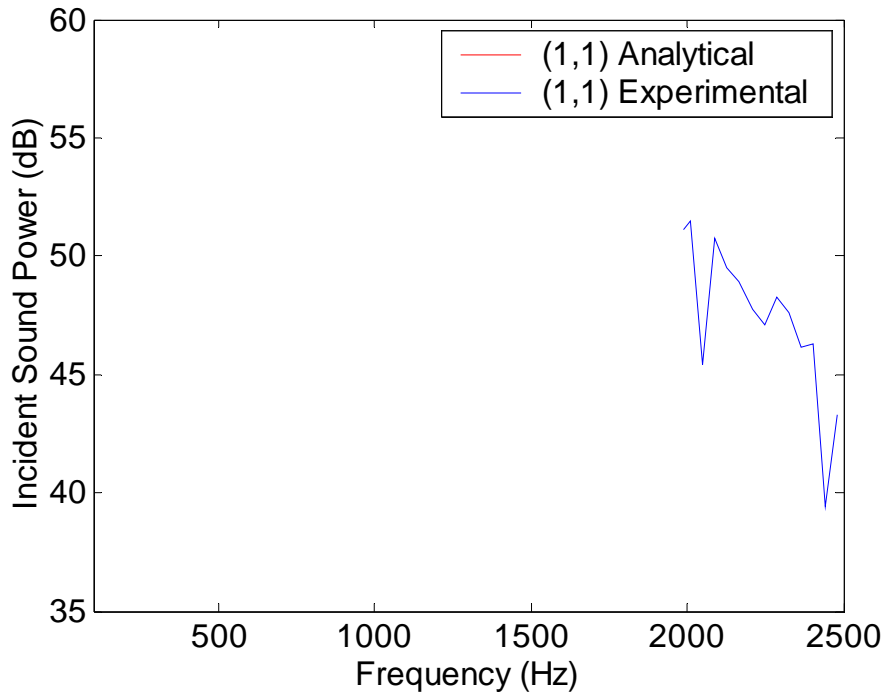


Figure 4-41: Experimental  $W_i^{++}$  of the (1,1) mode.

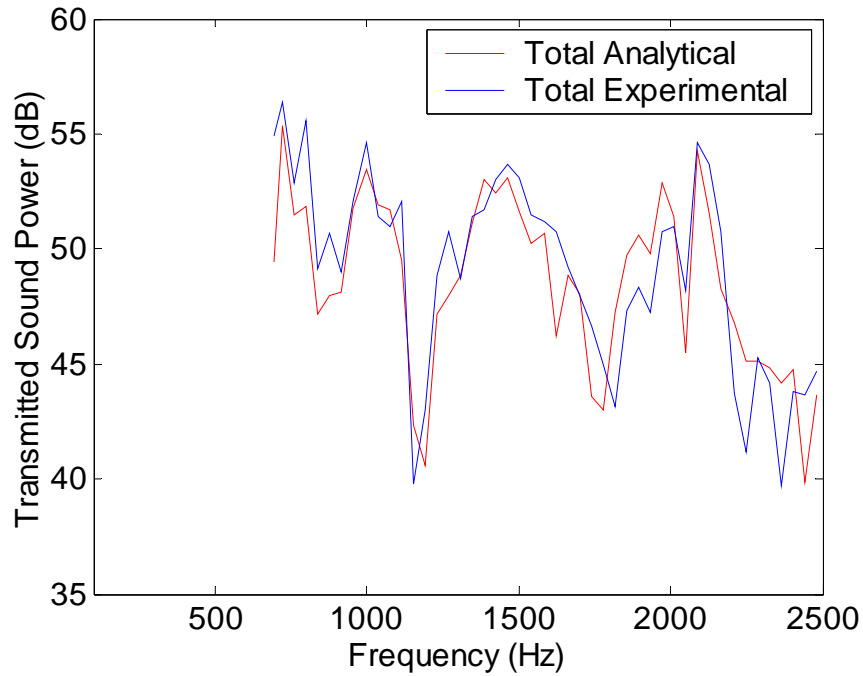


Figure 4-42: Analytical versus experimental total  $W_T^{++}$  of the  $m$ -order 1 modes with 16 HQ tubes in position 1.

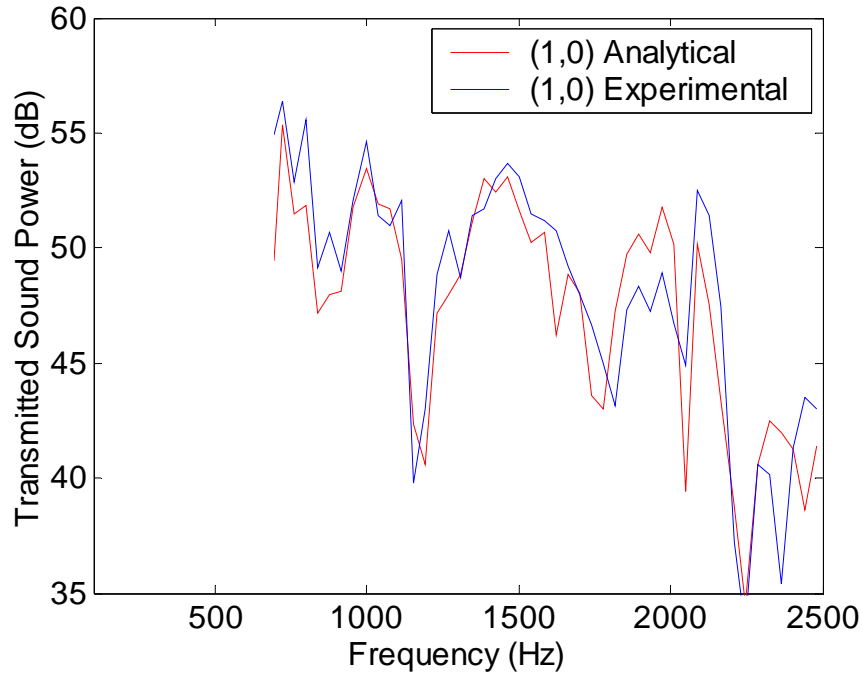


Figure 4-43: Analytical versus experimental  $W_T^{++}$  of the (1,1) mode with 16 HQ tubes in position 1.

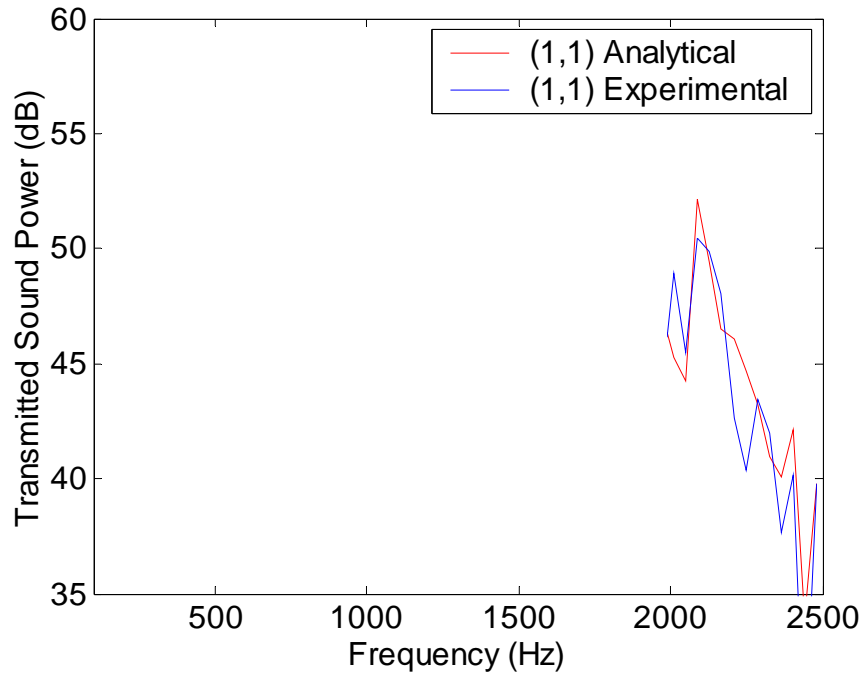


Figure 4-44: Analytical versus experimental  $W_T^{++}$  of the (1,1) mode with 16 HQ tubes in position 1.

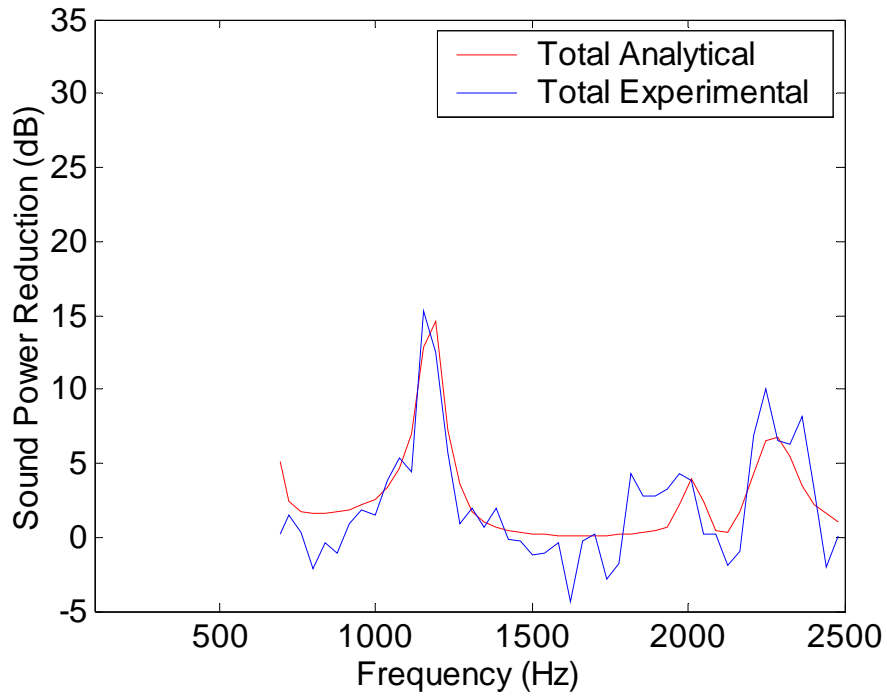


Figure 4-45: Analytical versus experimental total  $W_{Red}^{++}$  of the  $m$ -order 1 modes with 16 HQ tubes in position 1.

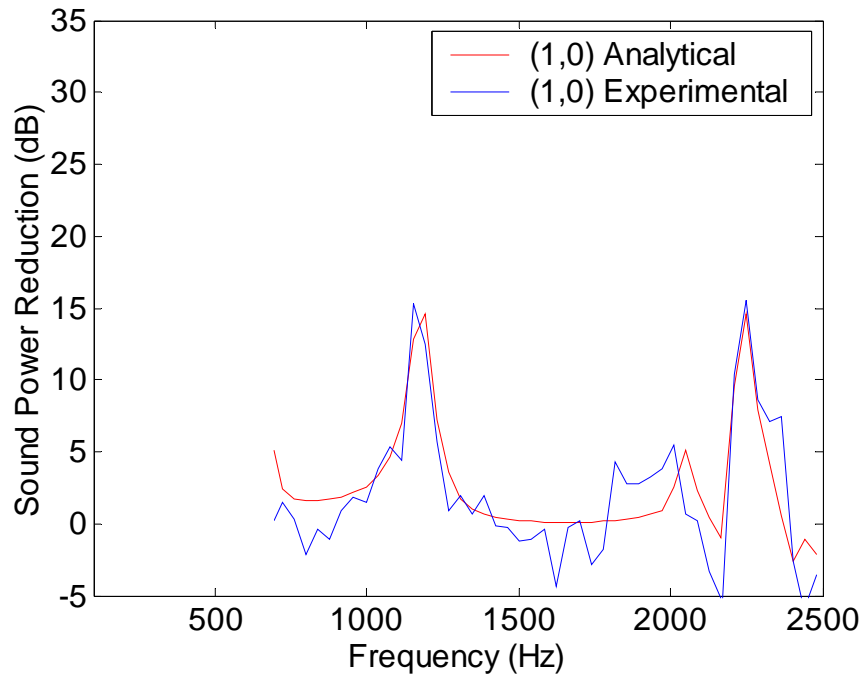


Figure 4-46: Analytical versus experimental  $W_{Red}^{++}$  of the (1,0) mode with 16 HQ tubes in position 1.

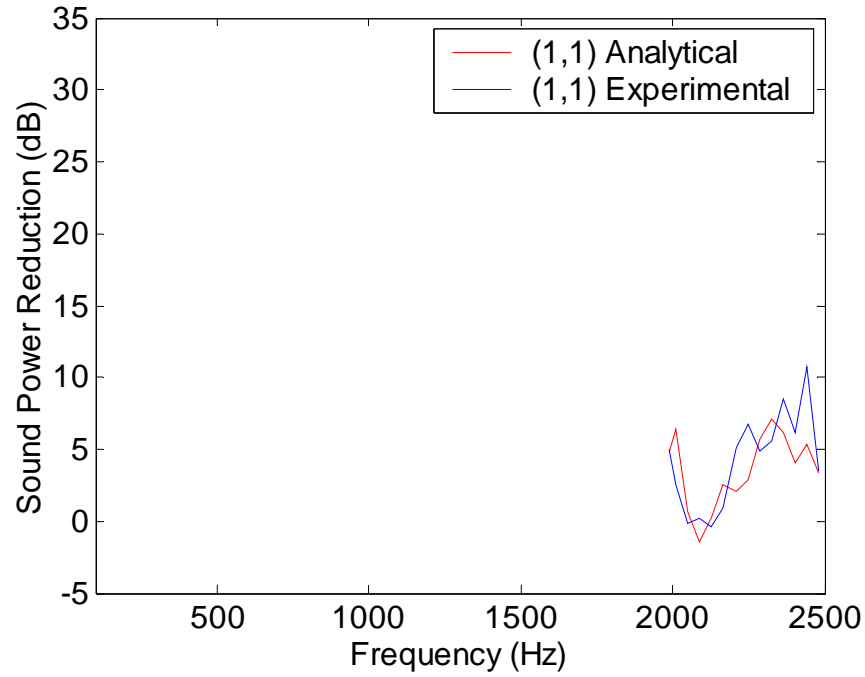


Figure 4-47: Analytical versus experimental  $W_{Red}^{++}$  of the (1,1) mode with 16 HQ tubes in position 1.

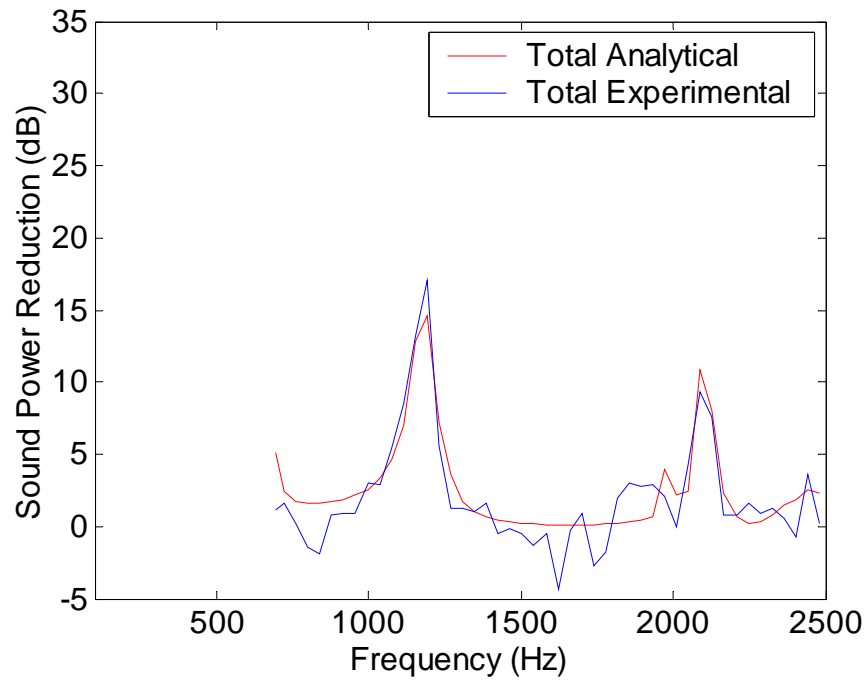


Figure 4-48: Analytical versus experimental total  $W_{Red}^{++}$  of the  $m$ -order 1 modes with 16 HQ tubes in position 2.

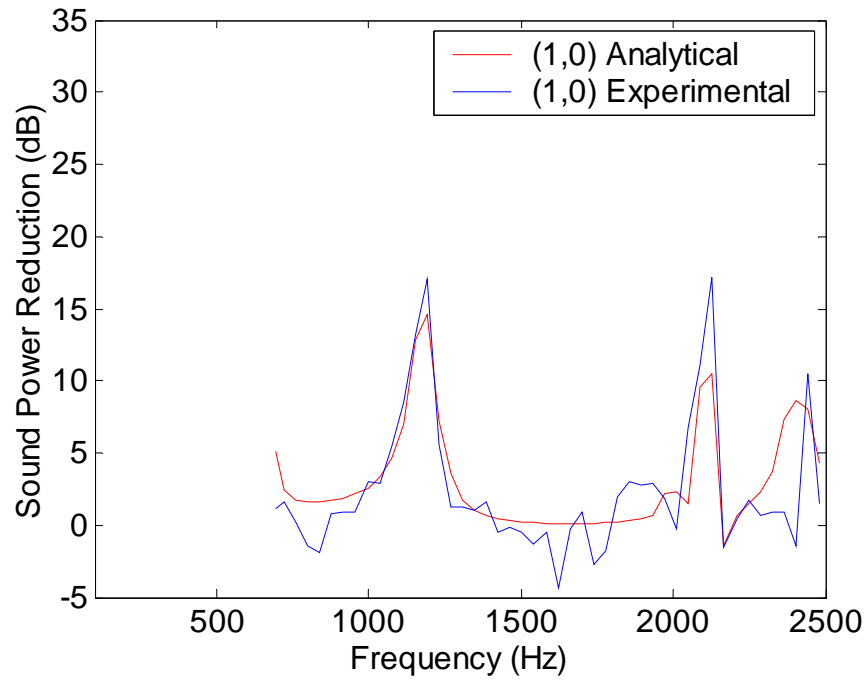


Figure 4-49: Analytical versus experimental  $W_{Red}^{++}$  of the (1,0) mode with 16 HQ tubes in position 2.

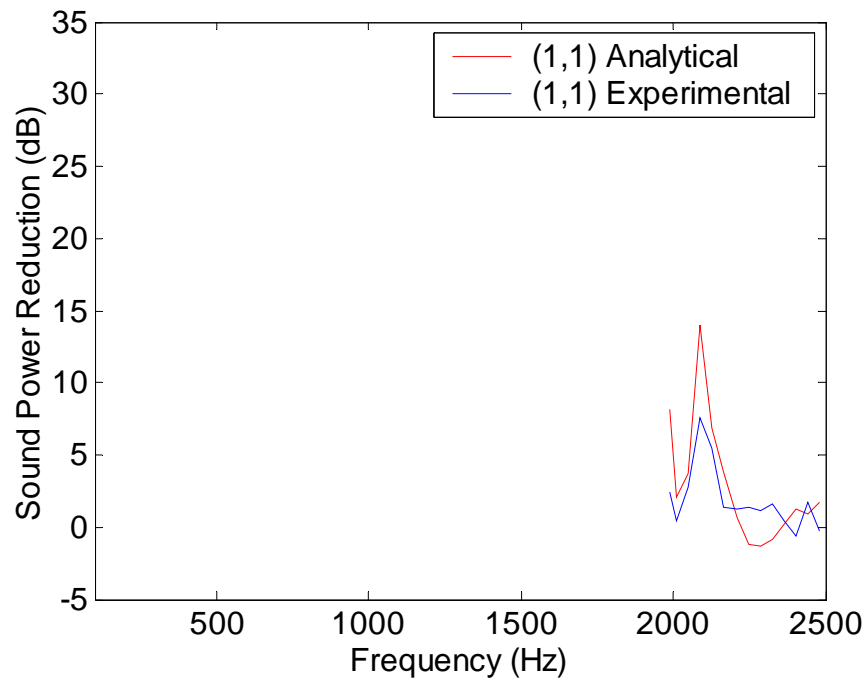


Figure 4-50: Analytical versus experimental  $W_{Red}^{++}$  of the (1,1) mode with 16 HQ tubes in position 2.

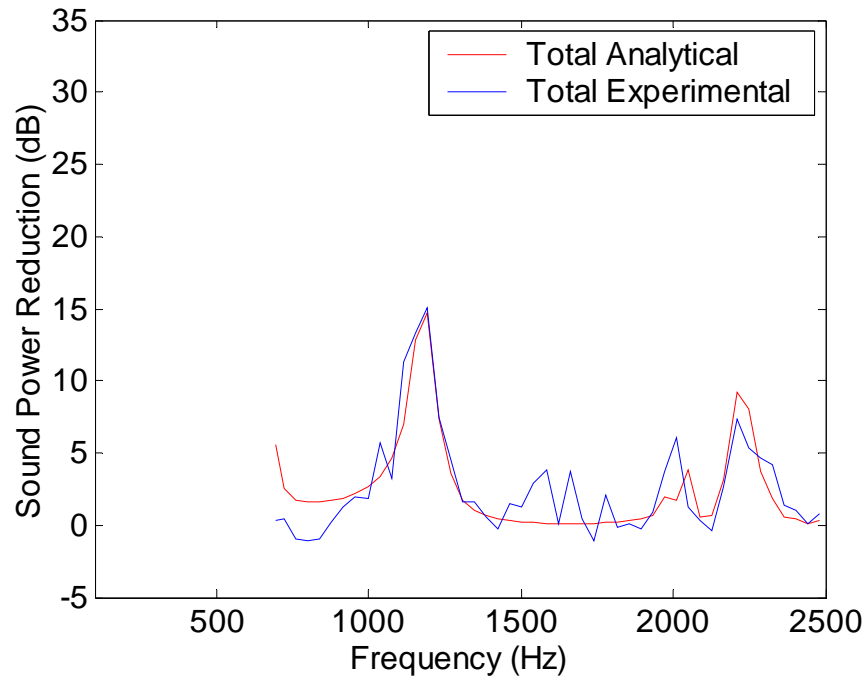


Figure 4-51: Analytical versus experimental total  $W_{Red}^{++}$  of the  $m$ -order 1 modes with 16 HQ tubes in position 3.

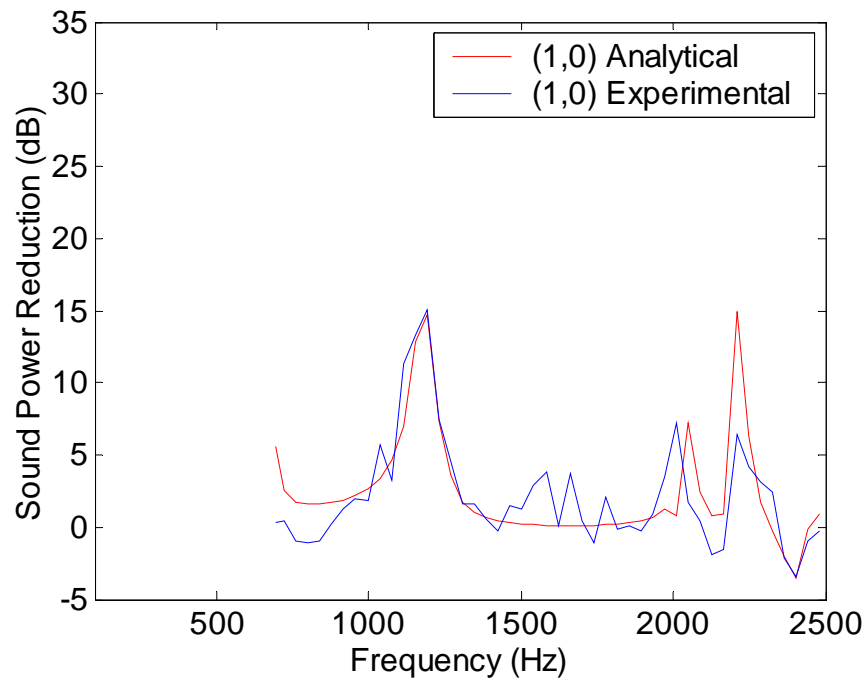


Figure 4-52: Analytical versus experimental  $W_{Red}^{++}$  of the (1,0) mode with 16 HQ tubes in position 3.

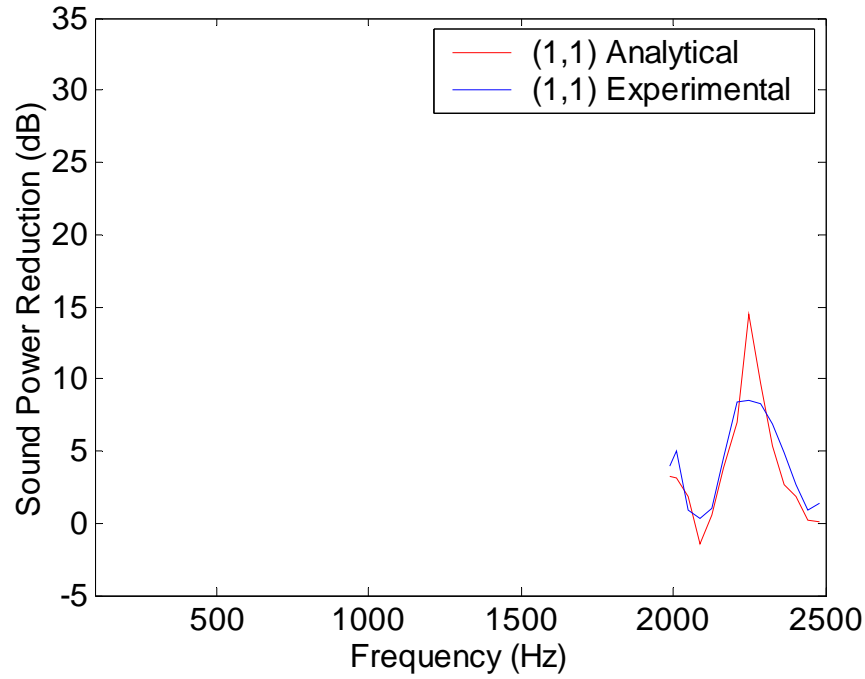


Figure 4-53: Analytical versus experimental  $W_{Red}^{++}$  of the (1,1) mode with 16 HQ tubes in position 3.

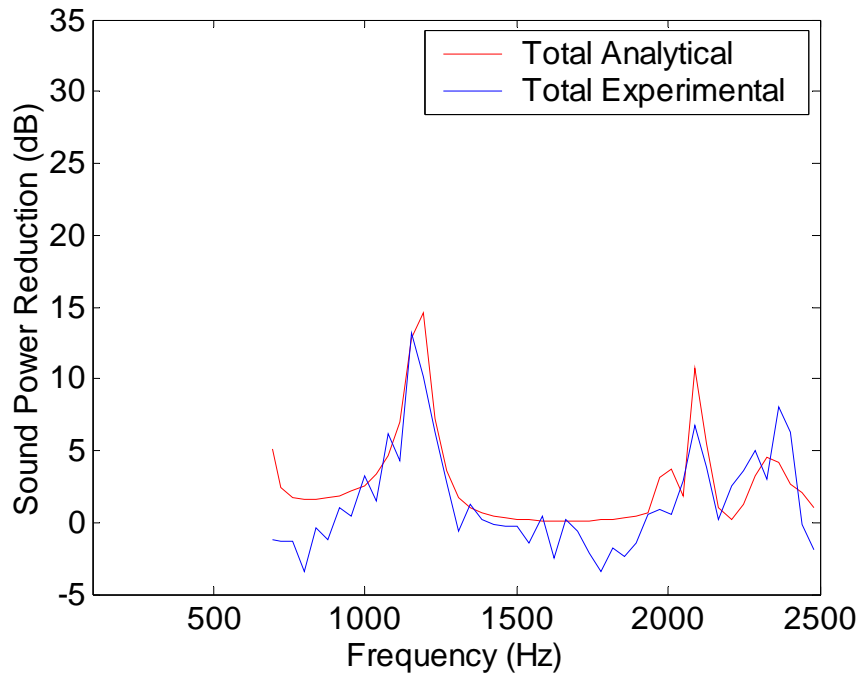


Figure 4-54: Analytical versus experimental total  $W_{Red}^{++}$  of the  $m$ -order 1 modes with 16 HQ tubes in position 4.

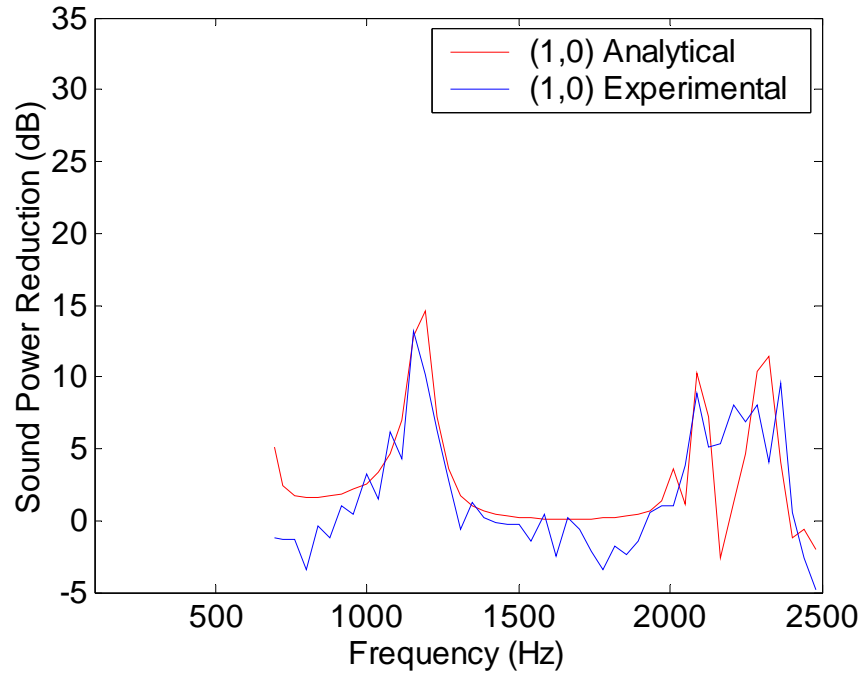


Figure 4-55: Analytical versus experimental  $W_{Red}^{++}$  of the (1,0) mode with 16 HQ tubes in position 4.

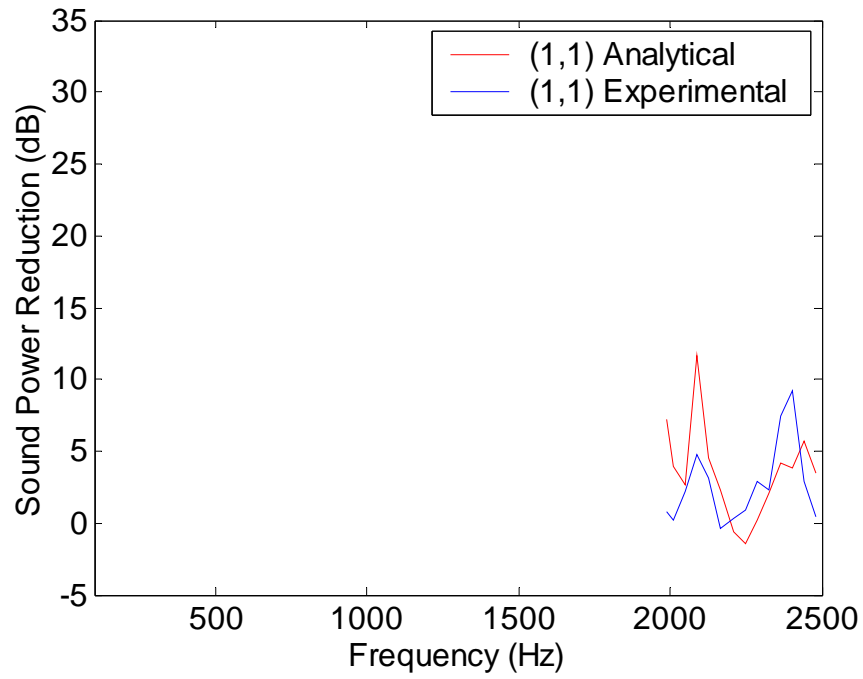


Figure 4-56: Analytical versus experimental  $W_{Red}^{++}$  of the (1,1) mode with 16 HQ tubes in position 4.

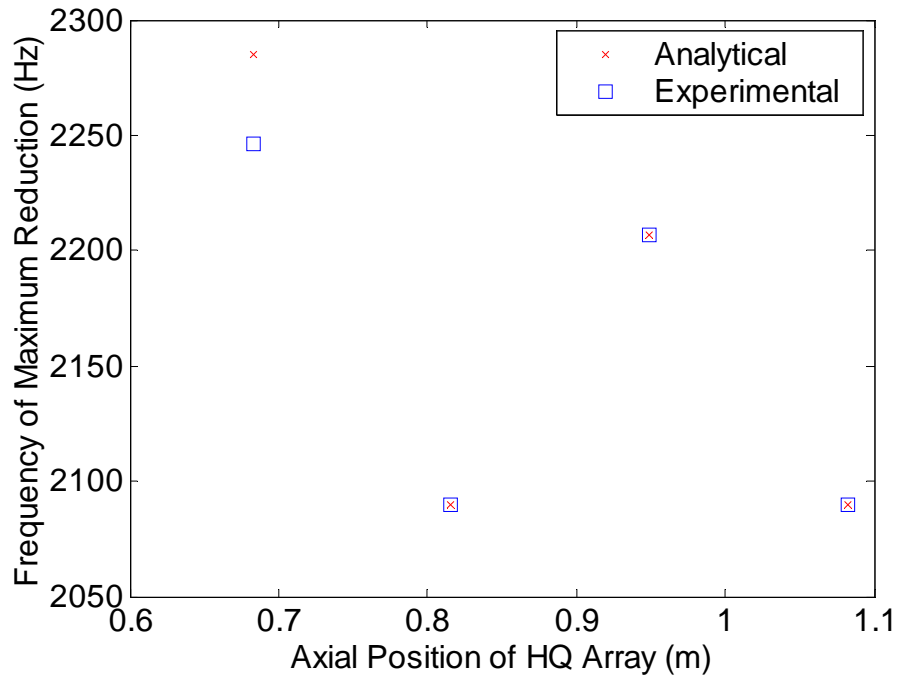


Figure 4-57: Frequency of maximum sound power reduction of the total power of the  $m$ -order 1 modes as a function of axial position of the HQ tubes.

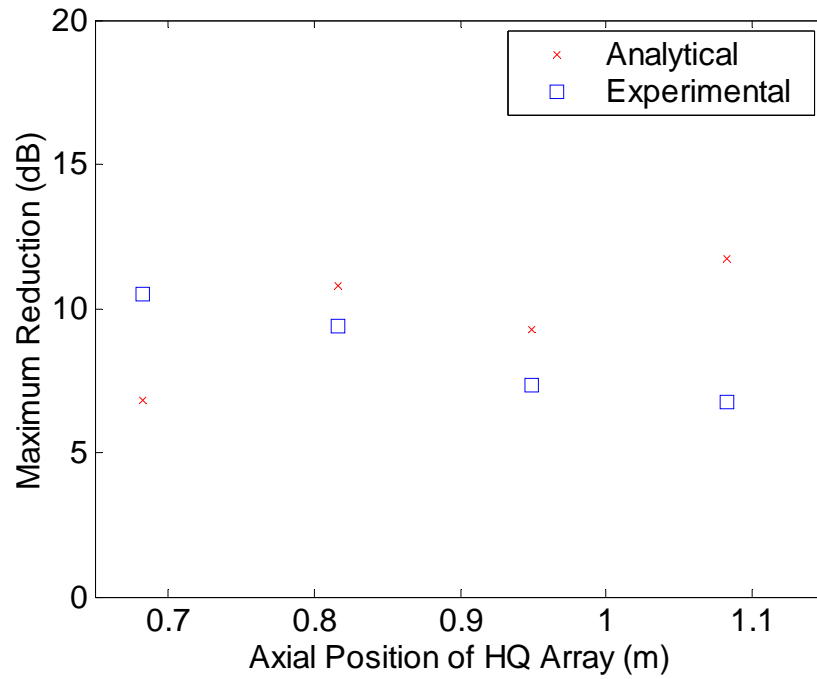


Figure 4-58: Maximum sound power reduction of the total power of the  $m$ -order 1 modes as a function of axial position of the HQ tubes.

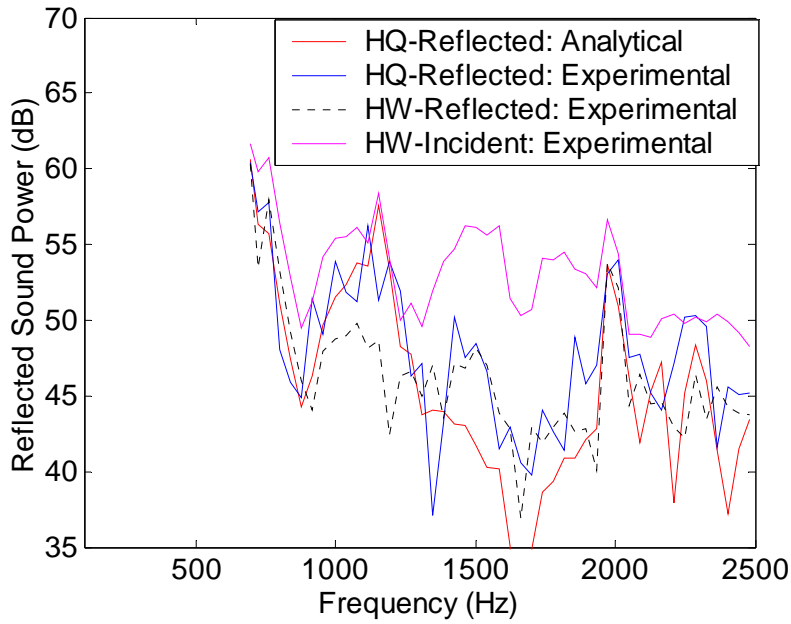


Figure 4-59: The  $m$ -order 1 modes: analytical versus experimental total  $W_R^{+-}$  with 16 HQ tubes in position 6 compared to the experimental hard wall  $W_R^{+-}$  and  $W_I^{++}$ .

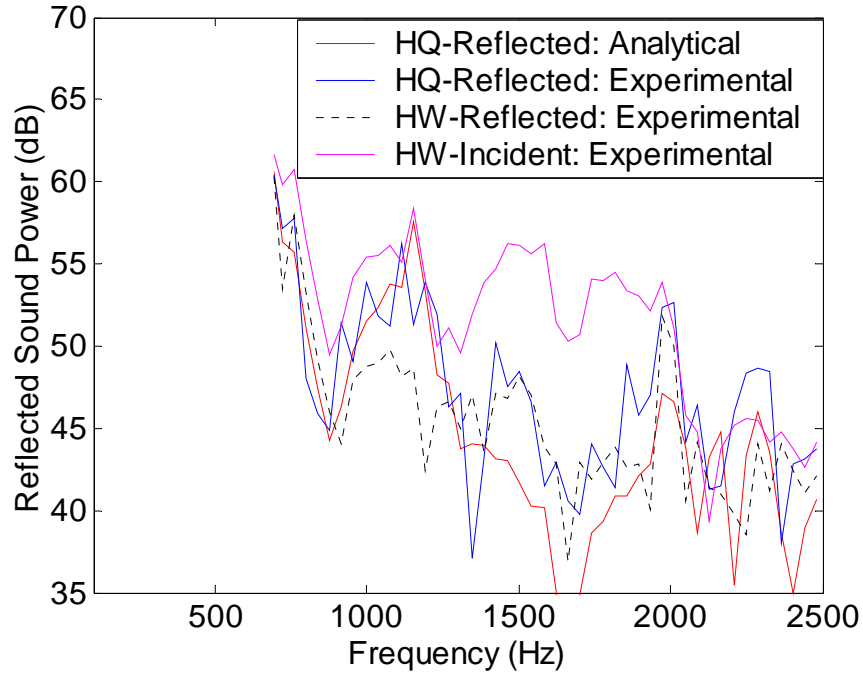


Figure 4-60: The (1,0) mode: analytical versus experimental  $W_R^{+-}$  with 16 HQ tubes in position 6 compared to the experimental hard wall  $W_R^{+-}$  and  $W_I^{++}$ .

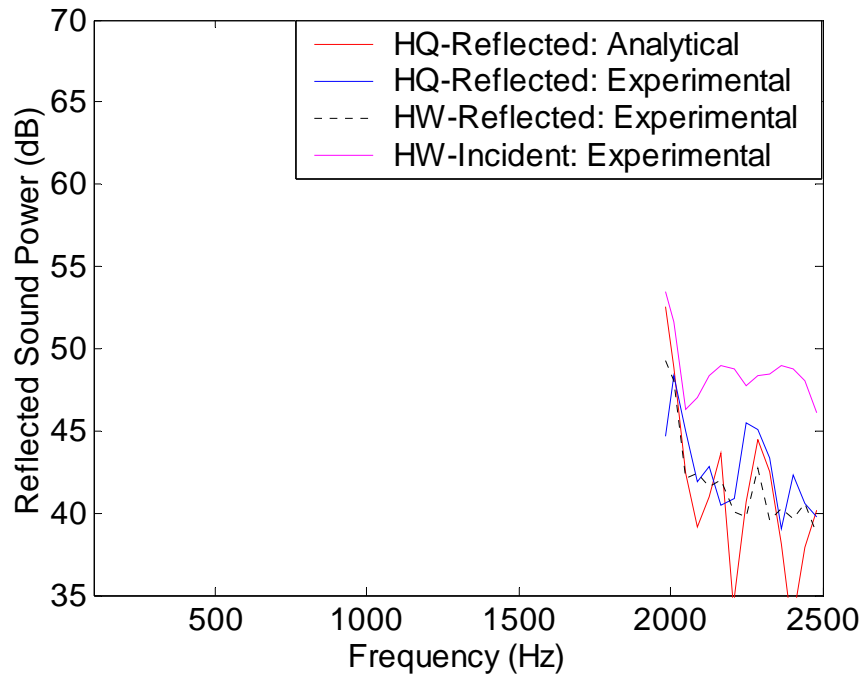


Figure 4-61: The (1,1) mode: analytical versus experimental  $W_R^{+-}$  with 16 HQ tubes in position 6 compared to the experimental hard wall  $W_R^{+-}$  and  $W_I^{++}$ .

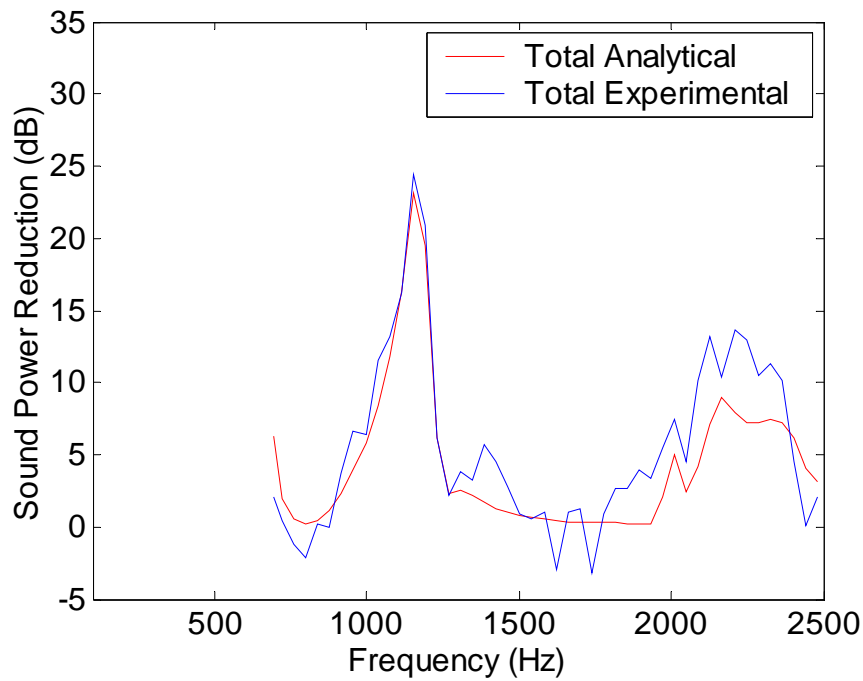


Figure 4-62: Analytical versus experimental total  $W_{Red}^{++}$  of the  $m$ -order 1 modes with 16 HQ tubes in position 5.

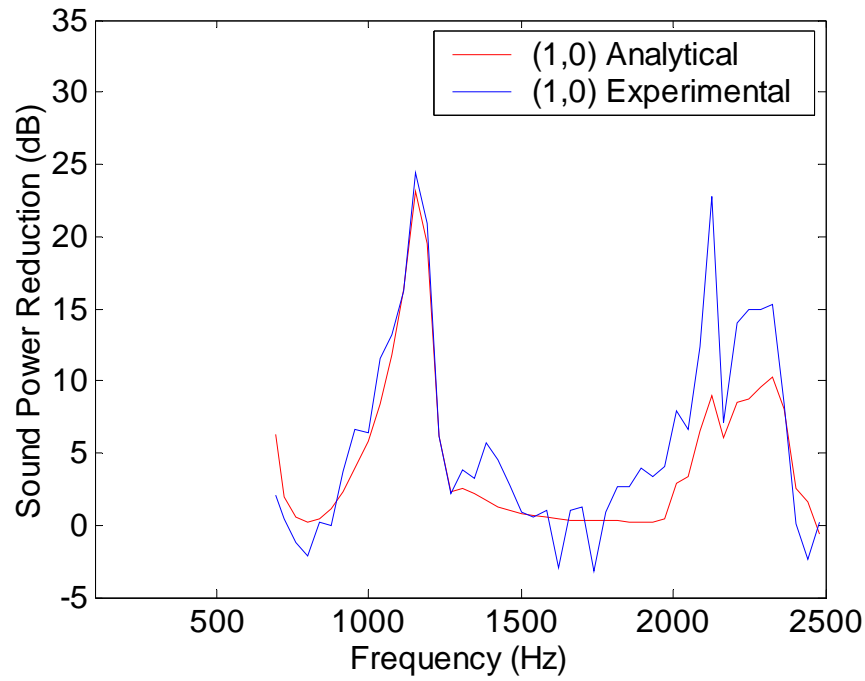


Figure 4-63: Analytical versus experimental  $W_{Red}^{++}$  of the (1,0) mode with 16 HQ tubes in position 5.

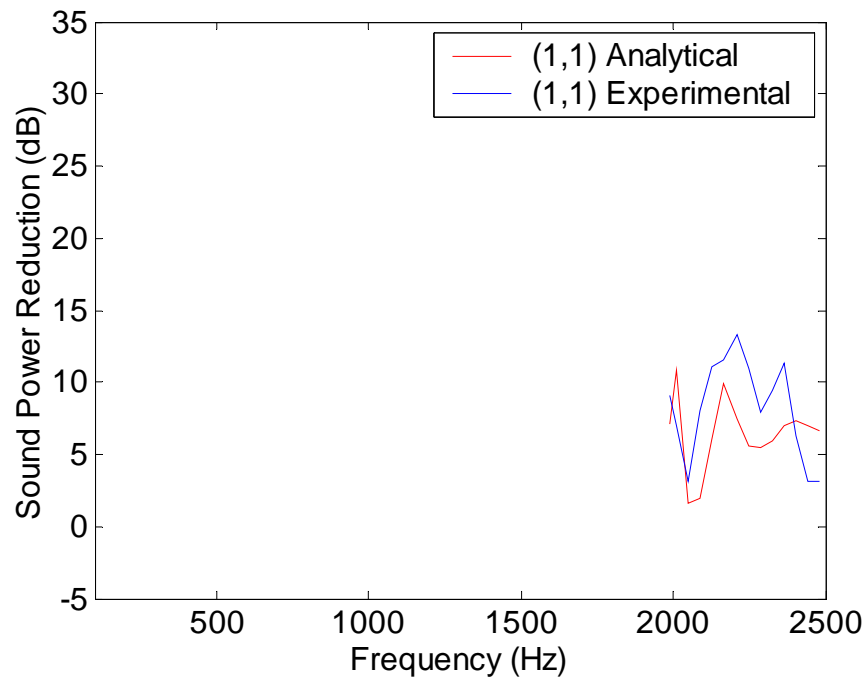


Figure 4-64: Analytical versus experimental  $W_{Red}^{++}$  of the (1,1) mode with 16 HQ tubes in position 5.

### 4.4.5 Test 5: Circumferential Scattering

#### Objectives and Description

This final experiment is designed to look at a simple case with circumferential scattering. The lone incident disturbance mode is the positive spinning and traveling  $(4,0)$  mode with a cut-off frequency of 1968 Hz. A single array of 8 HQ tubes was designed to create a case where circumferential scattering was present. At the HQ tube array interface the  $(4,0)$  mode circumferentially scatters energy into the  $(-4,0)$  mode. This scattering occurs because of the spatially aliasing of the HQ tubes. In addition, some of the energy of the  $(4,0)$  and  $(-4,0)$  modes are transmitted upstream while some is reflected downstream. The experimental setup is shown in Figure 4-65.

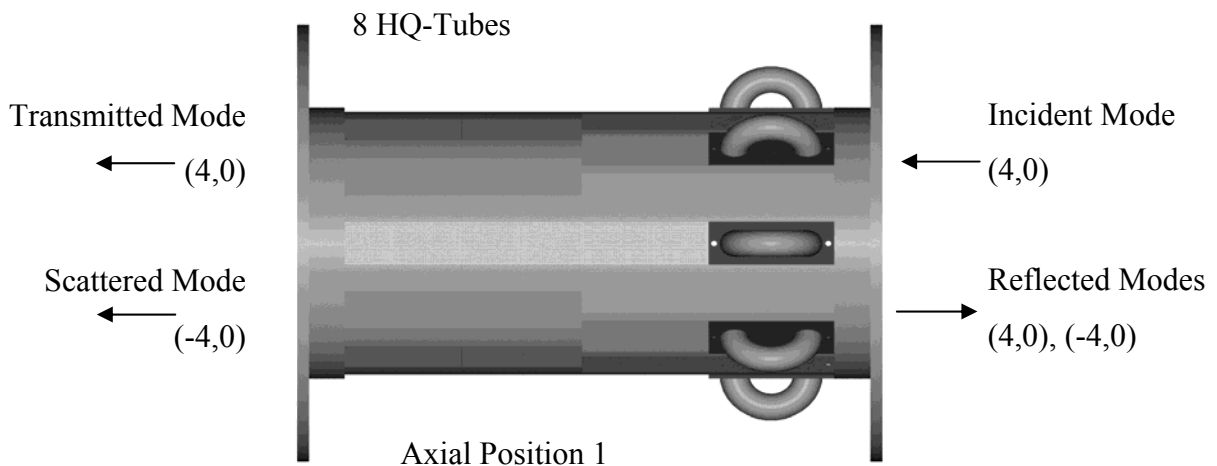


Figure 4-65: Test 5 experimental setup with HQ tube system

#### Test 5 Results: Circumferential Scattering

The incident positive spinning and traveling  $(4,0)$  mode is shown in Figure 4-66. The level of the incident  $(4,0)$  mode is shown to be significantly higher than the  $(-4,0)$  mode, which should not be present in the hard wall case. As the incident  $(4,0)$  mode encounters the HQ tubes it circumferentially scatters energy into the  $(-4,0)$  mode. The total transmitted sound power of the  $m$ -order 4 modes is shown in Figure 4-67. The transmitted sound power of the  $(4,0)$  and  $(-4,0)$  modes follow in Figure 4-68 and Figure

## Chapter 4. Experimental Results

4-69, respectively. The total  $m$ -order 4, (4,0), and (-4,0) modes are predicted very accurately in shape and level. The total sound power reduction of the  $m$ -order 4 modes shows a slight reduction at the cut-off frequency of the (4,0) mode, as show in Figure 4-70. However, in Figure 4-71 the sound power reduction of the (4,0) mode shows significant reduction, especially around the cut-off frequency. This significant reduction can be attributed to the circumferential scattering of the (4,0) mode into the (-4,0) mode.

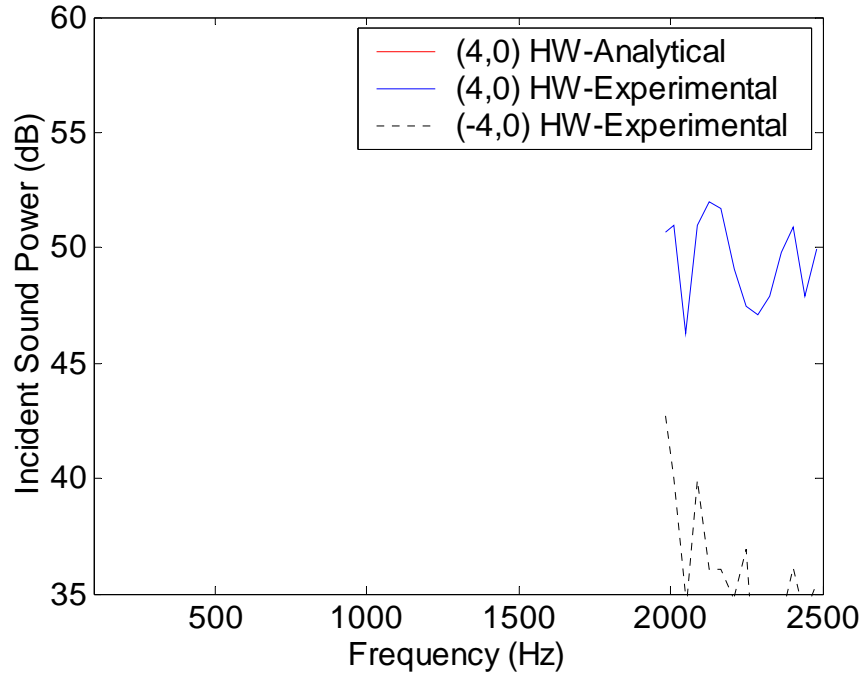


Figure 4-66 Experimental  $W_l^{++}$  of the (4,0) mode compared to the experimental  $W_l^{-+}$ .

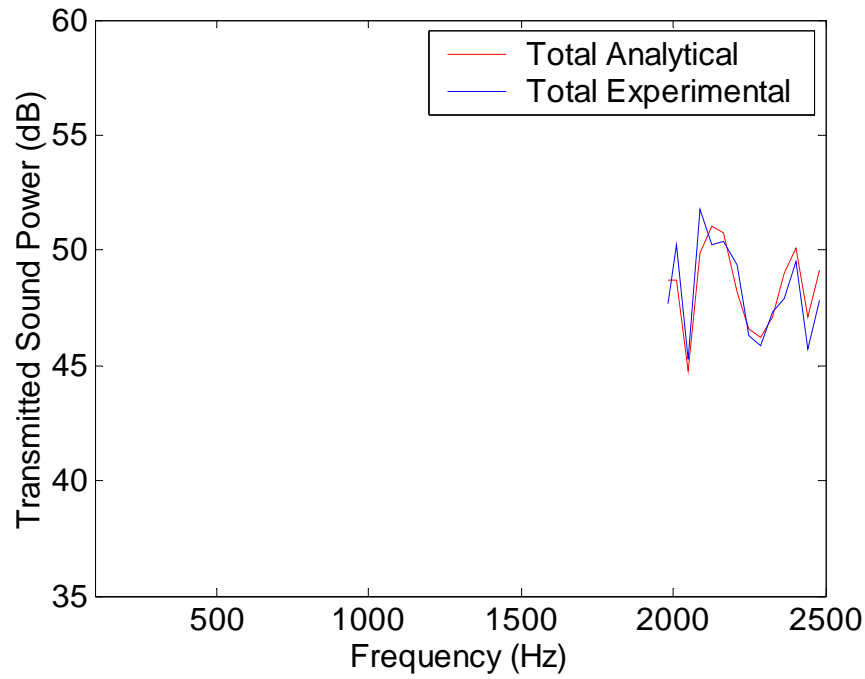


Figure 4-67: Analytical versus experimental total  $W_T$  of the  $m$ -order 4 modes with 8 HQ tubes in position 1.

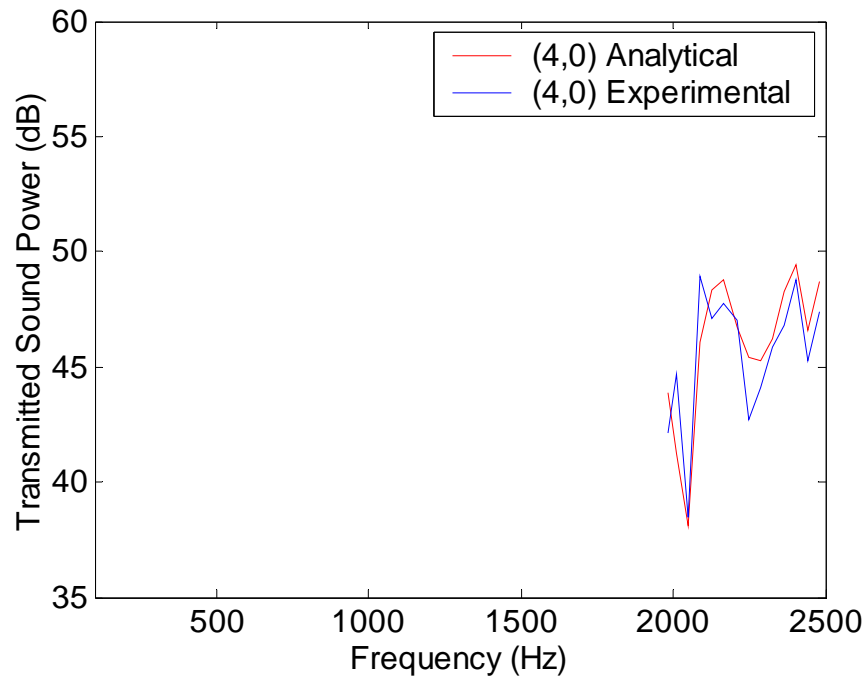


Figure 4-68: Analytical versus experimental  $W_T^{++}$  of the (4,0) mode with 8 HQ tubes in position 1.

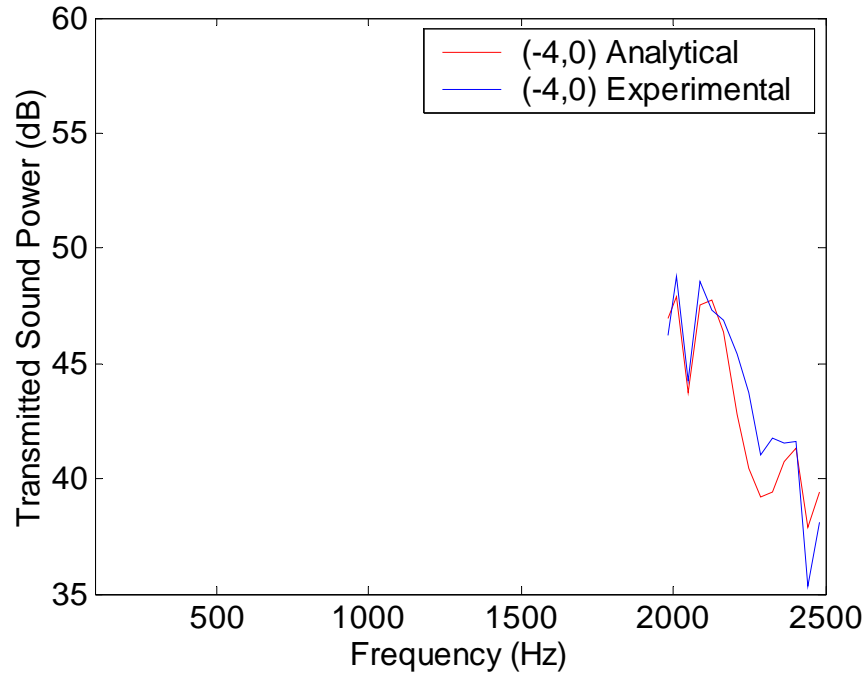


Figure 4-69: Analytical versus experimental  $W_T^{-+}$  of the (-4,0) mode with 8 HQ tubes in position 1.

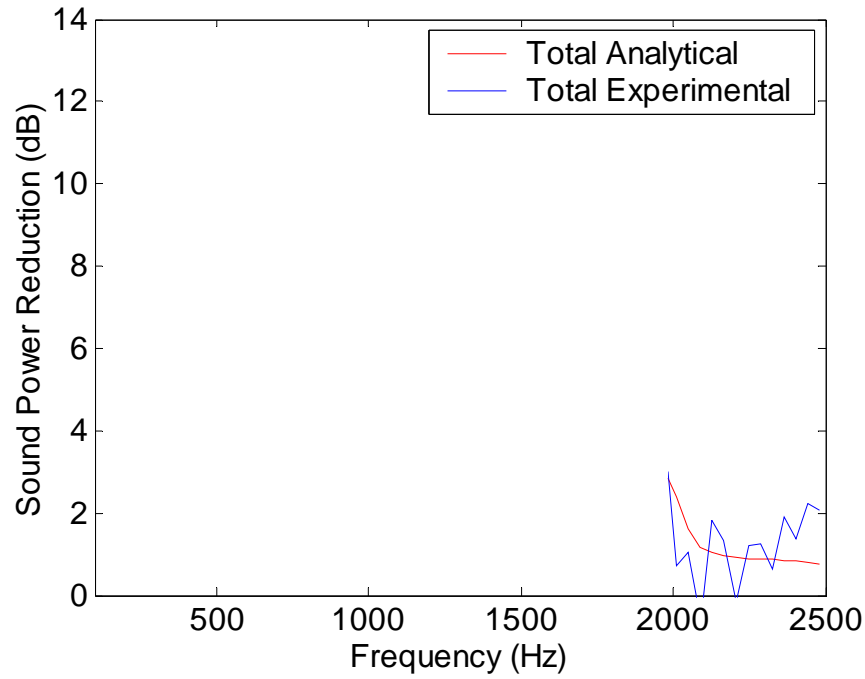


Figure 4-70: Analytical versus experimental total  $W_{Red}$  of the  $m$ -order 4 modes with 8 HQ tubes in position 1.

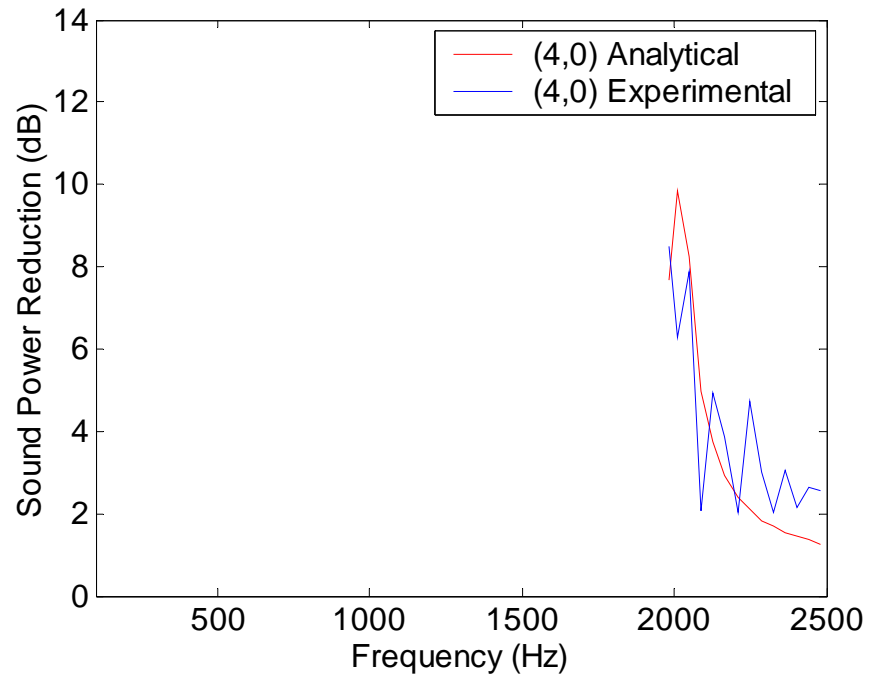


Figure 4-71: Analytical versus experimental  $W_{Red}^{++}$  of the (4,0) mode with 8 HQ tubes in position 1.

## **Chapter 5. Conclusions and Recommendations**

In this final chapter, conclusions of the study and recommendations for future work will be presented. The results of the fundamental study of the Herschel-Quincke tube concept are reviewed in the conclusions. The recommendations outline theoretical and experimental improvements that could be made on this study. Additional experiments and alternative methods that could be used for future experiments are also presented.

### **5.1 Theoretical and Experimental Conclusions**

A fundamental study of the Herschel-Quincke tube concept for the reduction of noise in circular ducts is investigated in this thesis. The primary goals of this research are to evaluate the accuracy of the previously developed theoretical model and provide insight into the noise control mechanisms of the HQ tubes. To obtain these objectives experiments were performed for different disturbance mode structures, number of HQ tubes and arrays, and axial positions of the arrays in a controlled laboratory environment. The modes in the duct were generated with an array of acoustic drivers and measured with logarithmically spaced circumferential and helical microphone arrays located on the duct wall. The modal amplitudes of the incident, transmitted, and reflected modes in the duct were determined from the microphone measurements. This allowed for the comparison of analytical and experimental modal amplitudes, modal powers, total power, and reductions.

For a single incident mode, there is very good agreement between level, shape, and system resonance frequencies between the analytical and experimental results. With multiple incident modes, the analytical and experimental results also show good agreement. The frequencies of maximum attenuations are accurately predicted with some discrepancies in the level of attenuation. The model also predicts the effects of the number of HQ tubes and axial position very well. Increasing the number of HQ tubes increased the resonant frequencies of the HQ tube system and the level of maximum attenuation. With multiple incident modes, changing the axial position of the HQ tube array produced a sinusoidal variation in the frequency and level of maximum attenuation. The model predicts this variation quite accurately. Increasing the number of HQ tube arrays increases the level of attenuation, as expected. However, the model under-predicts the attenuation at the 2<sup>nd</sup> tube resonance by approximately 4 dB.

At the cut-off frequency of the modes, the results show poor agreement with the analytical predictions generally showing higher levels of attenuation than the experimental results. For reflected modes, the analytical predictions and experimental results generally agree in shape, with discrepancies on the level of reflected sound power. The discrepancies at the cut-off frequency and levels of reflected modes could be a result of the theoretical model not taking into account the reflection at the open end of the duct.

The results of this study provided insight into the three noise control mechanisms associated with this approach. Evidence of reflection, circumferential scattering, and radial scattering are shown. Overall, the results of this study validate the general modeling approach for the HQ tube concept.

## 5.2 Recommendations

There are many theoretical and experimental recommendations for future work. The experimental results can be used to investigate improvements in the VPI theoretical model. The theoretical model takes into account reflection of the HQ tube system. However, the reflection due to the open end of the duct is not modeled. Modeling this reflection is especially important at the cut-off frequencies where significant reflections

## Chapter 5. Conclusions and Recommendations

occur. It is also very important for the analytical and experimental comparisons of the reflected modes in the duct. This could help explain the large discrepancies in sound power levels at the cut-off frequencies of the modes in the duct.

Improvements can be made in the orthogonality condition of the modal decomposition technique. Increasing the number of microphones in the array and/or optimizing the position of the microphones would increase the difference between the magnitude of mode of interest and the other modes in the duct.

Improvements in the formulation of the disturbance modes generated from the acoustic drivers are also possible. Results show that the acoustic drivers generate the disturbance modes of interest along with significant modal content in the  $m$ -order 0 modes. This significant modal content in the  $m$ -order 0 modes results in contamination of the sound pressure measurements.

The experimental setup allowed measurement of the transmitted and reflected sound power of the modes in the duct. However, the setup did not allow for simultaneous recording of these measurements. Simultaneous recording would allow an energy balance to be performed on the system. An energy balance would provide insight into the losses caused from the perforated screen. It would also allow investigation of the effects of the perforated screen parameters, such as orifice radius and percentage of open area.

A more in-depth experimental investigation of circumferential and radial scattering of acoustic energy between modes is needed. Varying the number of acoustic drivers and HQ tubes, as well as examining the system at higher frequencies would cause more occurrences of circumferential and radial scattering.

Two possible extensions of the fundamental experiments performed in this work could be investigated. Using a low speed fan, the effects of flow on the HQ tube system could be examined. In addition, the use of acoustic liners with the HQ tube system could be investigated with the acoustic drivers or low speed fan.

Further consideration is needed to examine the use of square HQ tubes as a more simplistic and cost effective alternative to round HQ tubes. Round tubes are found in very limited pre-fabricated configurations and manufacturing to given specifications requires substantial financial investment. Using square tubes as an alternative may provide the insight needed for further HQ tube experiments, while allowing an infinite

number of possible configurations at a substantial cost savings. Figure 5-1 shows a preliminary study that compares the magnitude and phase of the frequency response function of round and square tubes with the equal cross sectional area, length, and center-to-center distance.

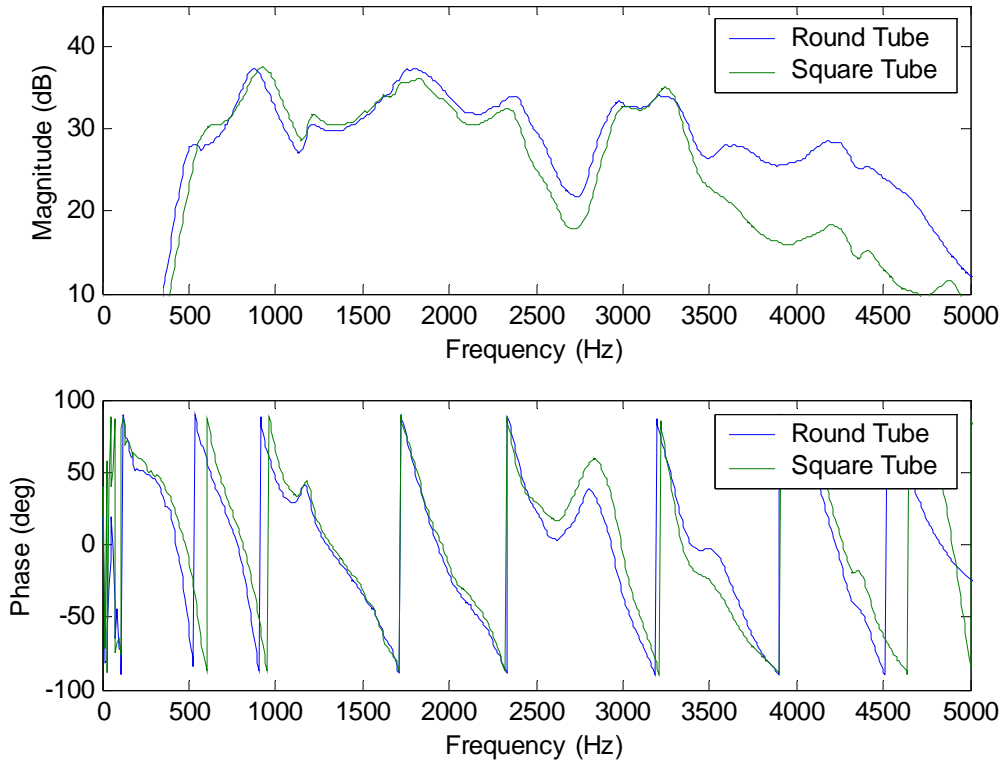


Figure 5-1: Comparison between the magnitude and phase of the frequency response function of round and square tubes.

The comparison of the frequency response functions of the round and square tubes shows excellent agreement in magnitude and phase up until approximately 3400 Hz. Differences at high frequencies could be a result of the reflections due to the corners in the square tube. The use of square tubes as a more versatile and cost effective alternative to round tubes appears to have real promise.

## **Appendix A. Additional Work**

### **A.1 Repeatability Analysis**

To determine if the results from the experiments could be repeated a case was chosen at random. All incident  $m$ -order modes were repeated for the HQ-tube case with 16 HQ-tubes in position 2. The sound power results for each  $m$ -order are presented in Figure A-1 through Figure A-9 showing trail 1 in red and trail 2 in blue. The results of the repeatability study show some differences in shape and level of the  $m$ -order 0 modes as seen in Figure A-1 through Figure A-3. However, Figure A-4 through Figure A-9 shows extremely good agreement in both shape and level of all other  $m$ -orders.

Appendix A. Additional Work

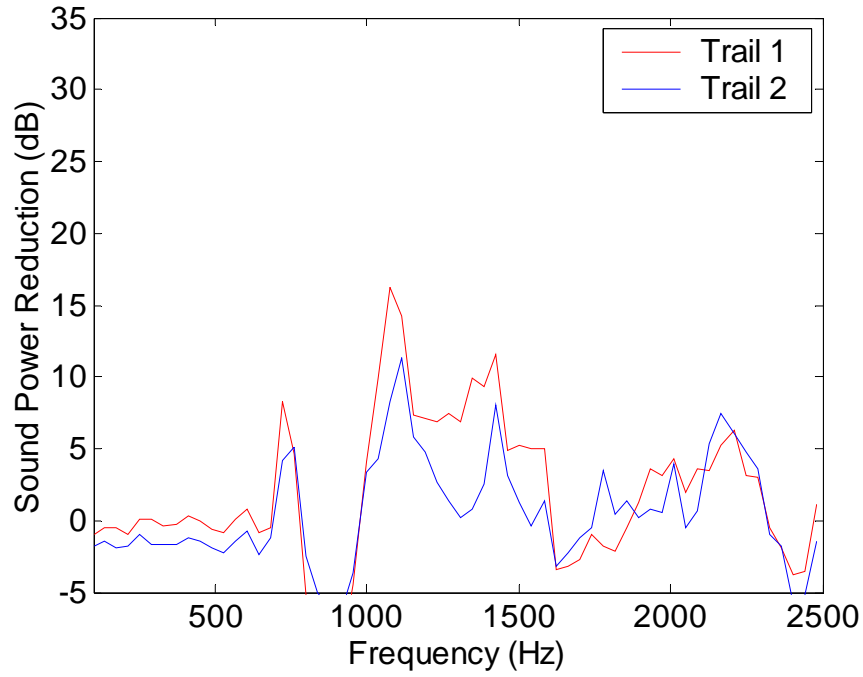


Figure A-1: Experimental comparisons of the total  $W_{Red}^{++}$  of the  $m$ -order 0 modes.

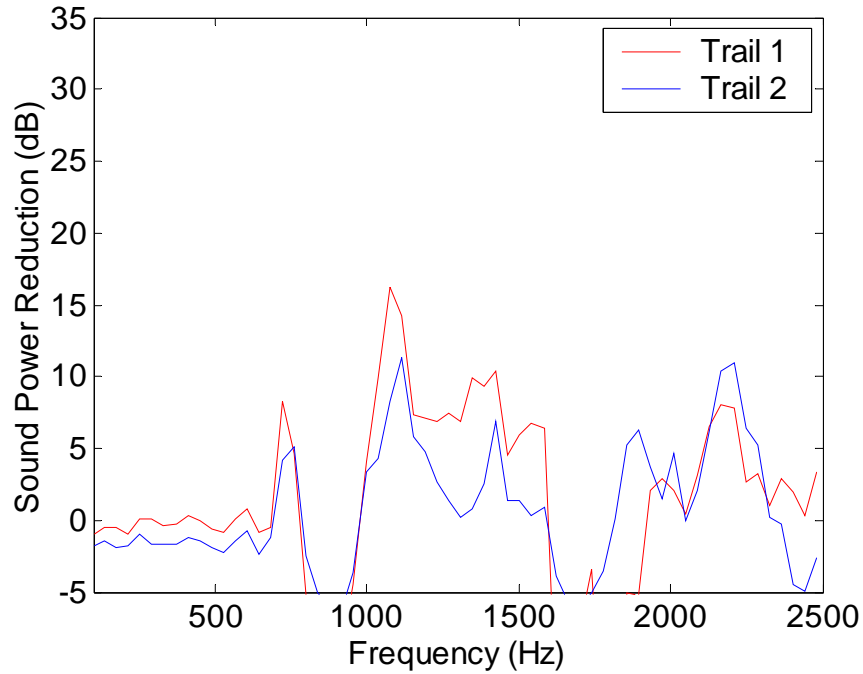


Figure A-2: Experimental comparisons of the total  $W_{Red}^{++}$  of the (0,0) mode.

Appendix A. Additional Work

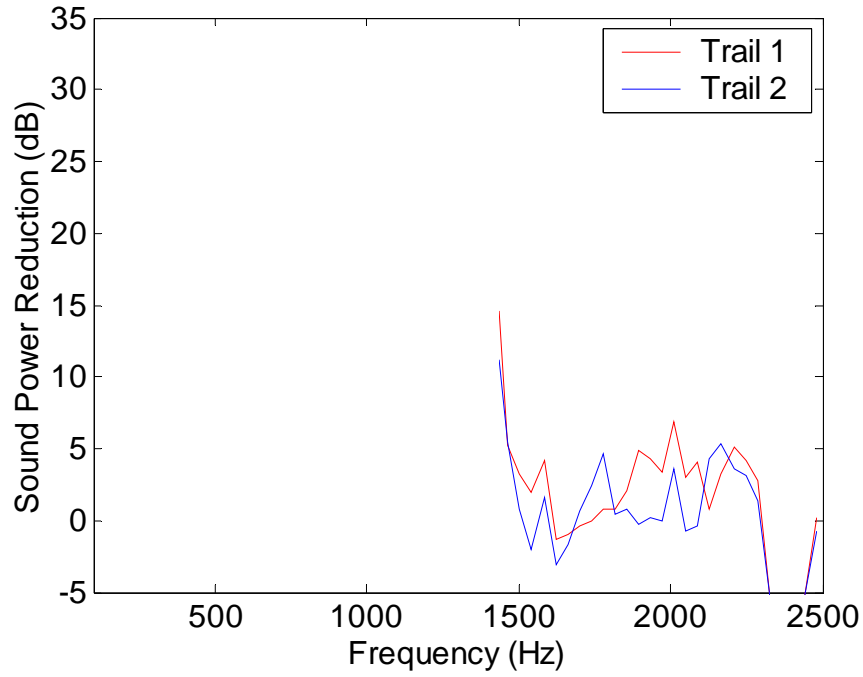


Figure A-3: Experimental comparisons of the total  $W_{Red}^{++}$  of the (0,1) mode.

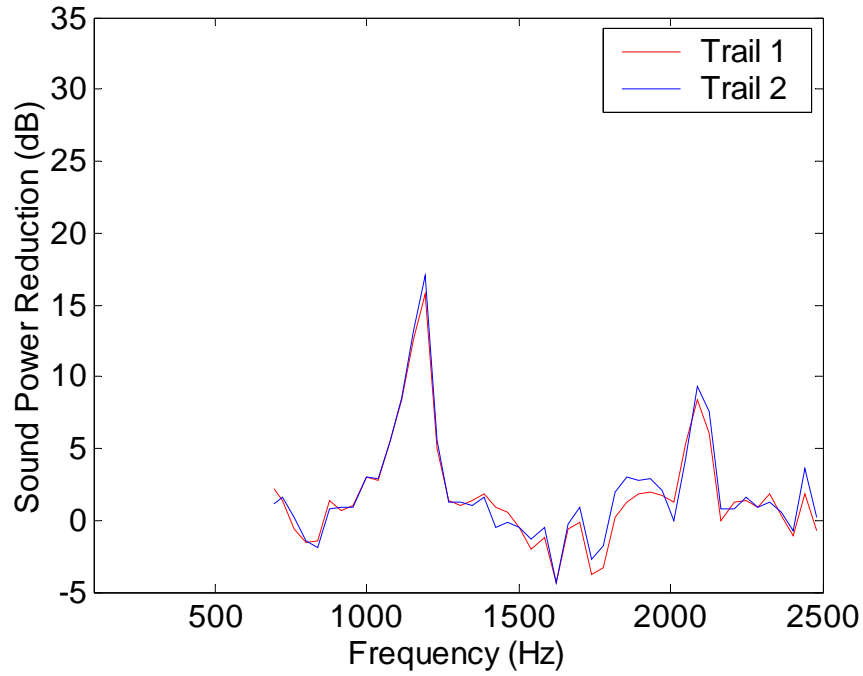


Figure A-4: Experimental comparisons of the total  $W_{Red}^{++}$  of the  $m$ -order 1 modes.

Appendix A. Additional Work

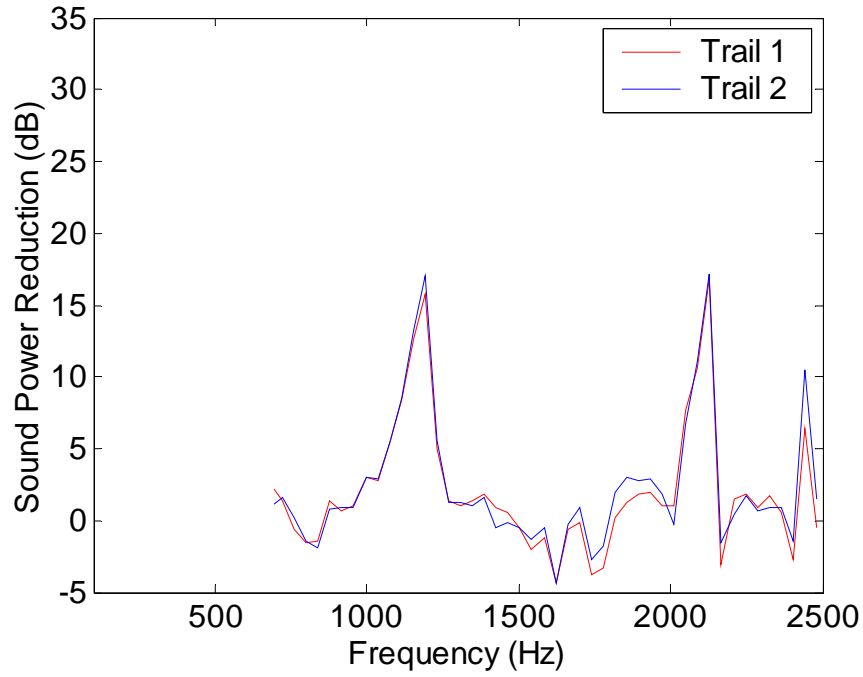


Figure A-5: Experimental comparisons of the total  $W_{Red}^{++}$  of the (1,0) mode.

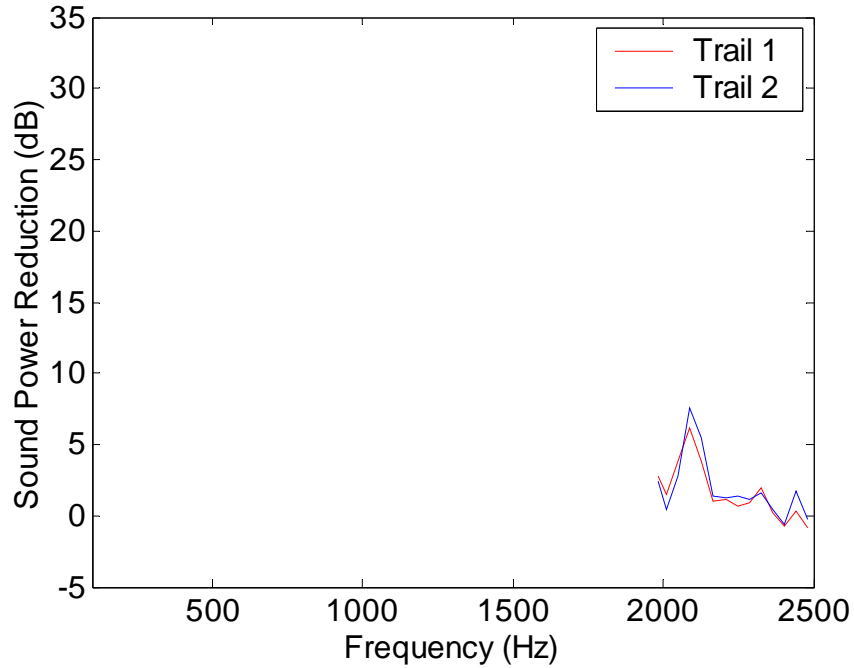


Figure A-6: Experimental comparisons of the total  $W_{Red}^{++}$  of the (1,1) mode.

Appendix A. Additional Work

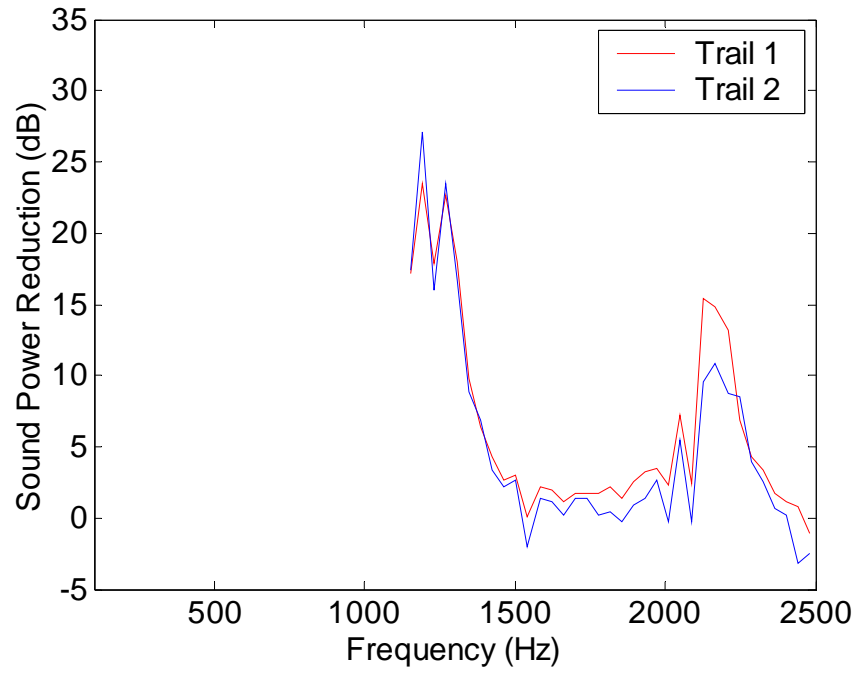


Figure A-7: Experimental comparisons of the total  $W_{Red}^{++}$  of the (2,0) mode.

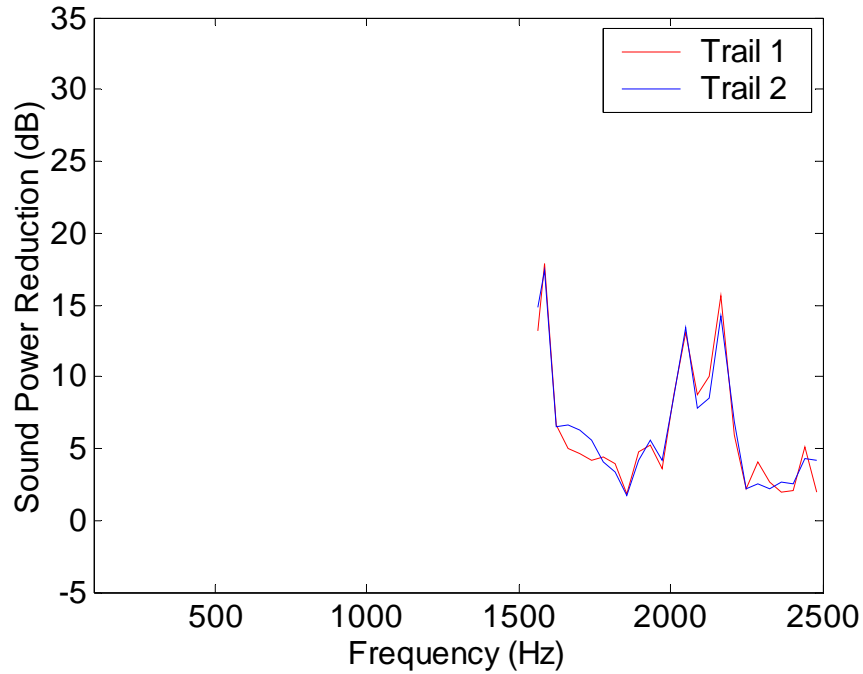


Figure A-8: Experimental comparisons of the total  $W_{Red}^{++}$  of the (3,0) mode.

Appendix A. Additional Work

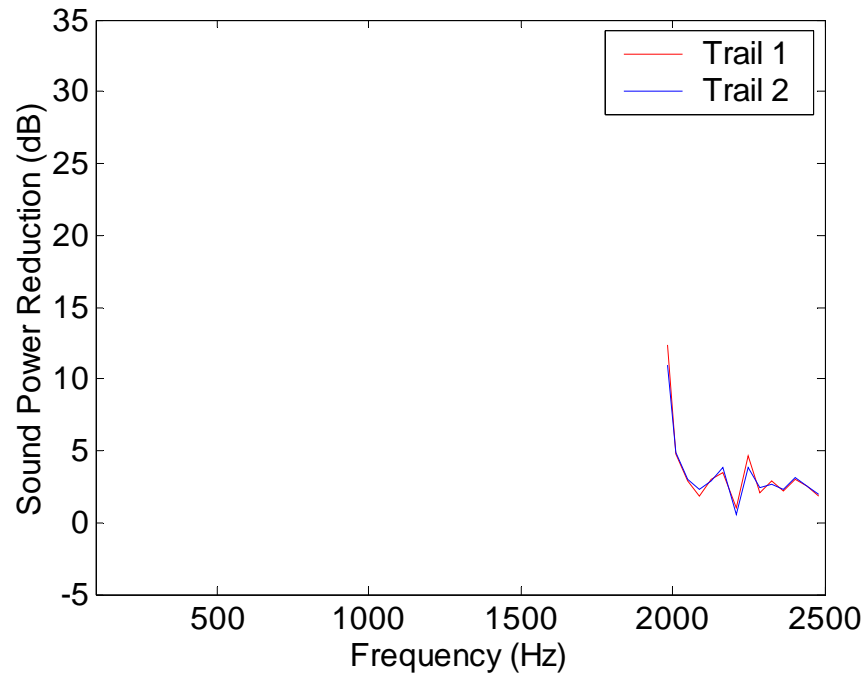


Figure A-9: Experimental comparisons of the total  $W_{Red}^{++}$  of the (4,0).

## References

---

- 1 NASA Glen Research Center, "Making Future Commercial Aircraft Quieter", 1999, <http://www.grc.nasa.gov/WWW/PAO/PAIS/fs03grc.htm> (2001).
- 2 R. A. Mangiarotty, "The Reduction of Aircraft Engine Fan-Compressor Noise Using Acoustic Linings," Journal of Sound and Vibration 18 (4) (1971): 565-576.
- 3 M. Rim and Y. J. Kim, "Narrowband Noise Attenuation Characteristics of In-Duct Acoustic Screens," Journal of Science and Vibration 234 (5) (2000): 737-759.
- 4 R. H. Thomas, R. A. Burdisso, C. R. Fuller, and W. F. O'Brien, "Active Control of Fan Noise From a Turbofan Engine," AIAA 93-0597 (1993).
- 5 J. P. Smith and R. A. Burdisso, "Active Control of Inlet Noise From a Turbofan Engine Using Inlet Wavenumber Sensors," CEAS/AIAA 99-1808 (1999).
- 6 R. A. Burdisso, C. R. Fuller, and J. P. Smith, "Experiments of the Active Control of a Turbofan Inlet Noise using Compact, Lightweight Inlet Control and Error Transducers," CEAS/AiAA 95-028, (1995): 177-185.
- 7 J. F. W. Herschel, "On the Absorption of Light by Colored Media, viewed in connection with the Undulatory Theory," Philosophical Magazine and Journal of Science, 3 (1833): 401-412.
- 8 G. Quincke, "Ueber interferenzapparate für schallwellen," Ann. Phys. Chem. 128 (1866): 177-192.
- 9 G. W. Stewart, "The Theory of the Herschel-Quincke Tube," Physical Review 31.4 (1928): 696-698.
- 10 Selamet, P. M. Radavich, and N. S. Dickey, "Mult-Dimensional Effects On Silencer Performance," Noise Control 94 (1994): 261-266.
- 11 A. Selamet, N. S. Dickey, and J. M. Novak, "The Herschel-Quincke tube: a theoretical, computational, and experimental investigation," J. Acoust. Soc. Am. 96 (5) (1994): 3177-3185.
- 12 A. Selamet and P. M. Radavich, "Effect of Expansion Chamber on the Resonance Frequency of Side Branches and Herschel-Quincke Tubes," ASME NCA 22 (1996): 127-132.
- 13 A. Selamet and V. Easwaran, "Modified Herschel-Quincke tube: Attenuation and resonance for n-duct configurations," Acoust. Soc. Am. 102.1 (1997): 164-169.

- 
- 14 C. R. Fuller and D. A. Bies, "The effects of flow on the performance of a reactive acoustic attenuator," J. Sound Vib., 62 (1979): 73-92.
- 15 A. J. Torregrosa, A. Broatch, and R. Payri, "A study of the influence of mean flow on the acoustic performance of Herschel-Quincke tubes," J. Acoust. Soc. Am. 107 (4) (2000): 1874-1879.
- 16 Z. Zhichi, L. Song, T. Rui, G. Rui, D. Genhua, and L. Peizi, "Application of Quincke tubes to flow ducts as a sound attenuation device," Noise Control Eng. J., 46 (6) (1998): 245-255.
- 17 L. A. Brady, R. A. Burdisso, and J. P. Smith, "Investigation of the Herschel-Quincke Concept for the Suppression of Higher-order Modes in a Duct," Proceedings of Internoise, 99 (1999): 545-550.
- 18 R. F. Hallez, J. P. Smith, and R. A. Burdisso, "Control of Higher-Order Modes in Ducts using Arrays of Herschel-Quincke Waveguides," ASME Control of Vibration and Noise (2000): 1-8.
- 19 R. D. Stunk, "Silencer for Hydraulic Piston Pump Pressure Pulsations," SAE Technical Paper Series, 911759, International Off-Highway & Powerplant Congress & Exposition (1991).
- 20 C. C. Chen and M. C. Hastings, "Half-wavelength tuning cables for passive noise control in automotive power steering systems," Act. Control Vib. Noise, ASME Proc. DE-75 (1994): 355-361.
- 21 R. A. Burdisso and J. P. Smith, "Control of Inlet Noise from Turbofan Engines Using Herschel-Quincke Waveguides," AIAA. 2000-1994.
- 22 R F. Hallez, "Investigation of the Herschel-Quincke Tube Concept as a Noise Control Device for Turbofan Engines," Masters of Science Thesis, Virginia Tech, 2001.